UNIVERSITY OF EXETER

# NON-INVASIVE NEAR-FIELD MICROWAVE DETECTION OF BREAST CANCER

*Submitted by*

*Wael Mouin Saleh*

*to the University of Exeter as a thesis for the degree of Doctor of Philosophy (Ph.D.) in Engineering, March 2007.*



I certify that all material in this thesis which is not my own work has been identified and that no material has previously been submitted and approved for the award of a degree by this or any other University.

.....

## ABSTRACT

The spread of breast cancer worldwide and the need for new technologies to improve breast cancer detection present a challenge to the standard medical screening methods. Tumour detection, in the early stages, is crucial if patients are to be treated effectively and with minimally invasive procedures. Thus, any technique that can improve on, or add to, existing breast tumour detection methods is welcome. In this thesis just such a technique based on near-field microwave imaging is investigated, both theoretically and experimentally. The electromagnetic waves interaction with dielectric structure is fundamental for any microwave application. Thus it is essential to understand the interaction of the microwaves radiated from the sensor (open-ended rectangular waveguide) with the breast structure under investigation.

A detailed mathematical model describing the interaction of microwaves emitted from an open rectangular wave-guide with an N-layer dielectric structure is developed, using the Fourier Transform Matching method. The model is capable of calculating the electric field properties anywhere within the N-layer structure, as well as the complex reflection coefficient existing at the waveguide aperture.

Computer simulations, based on the mathematical formulations derived using the Fourier Transform Matching method, of the near-field radiation patterns in a 3-layer approximation to the general N-layer model are presented. Such simulations are most useful in assessing the suitability of near-field microwave non-invasive testing and evaluation (NIT&E) technique for breast tumour detection. In addition, simulated 1-D and 2-D reflection phase and magnitude images are calculated and presented for the 3-layer structure with an inclusion to represent the presence of a tumour. Parameters controlling the detection sensitivity, specifically the frequency of operation, waveguide filling, and standoff distance dielectric filling, are investigated to obtain the optimal

parameters for the inspection system. The theoretical simulations show that a high sensitivity in both reflection coefficient magnitude and phase should be obtainable.

Experimental measurements of the reflection coefficient magnitude and phase when imaging a breast phantom that imitates real breast dielectric properties contrast are also presented. The phantom comprises a plexiglass container filled with soybean oil to represent normal breast tissue, with a small balloon filled with diacetin solution to represent the tumour. Both uncalibrated and calibrated measurements of reflection coefficient magnitude and phase were performed. The microwave source comprised an open-ended rectangular waveguide operating in the frequency range of approximately 8.2 to 12.4 GHz. Calibrated measurements were performed using a slotted waveguide system. An in-depth analysis between calibrated measurements and simulation results for a simple dielectric structure is illustrated to verify the simulation results. Then, calibrated measurements for breast phantom are obtained. Finally, a theoretical-versus-experimental qualitative assessment for the breast phantom verifies the mathematical model developed in the thesis. Thus, a near-field microwave non-invasive detection prototype is designed to experimentally detect tumour presence via measuring the sensor's aperture reflection coefficient.

## ACKNOWLEDGMENTS

First and foremost I would like to thank Allah (God) for all what I am and all what I have. Then, I would like to offer my sincere appreciation to those who supported me during this research endeavor. I would like to thank my parents for their understanding, patience and continuing support in every aspect of my life. Their good deeds started more than 28 years ago when I was an embryo (0- 8$^{th}$ week of gestational age before birth) then a fetus (after 8$^{th}$ week - just before birth) then a newborn (0-30 days) then a baby (1 month-1 year) then a toddler (1-4 years) then a middle childhood (4-8 years) then a late childhood (9-13 years) then a teenage (13-19 years) then a young adult (19-25 years) then an early adulthood (20-39 years). At every stage, they had their own way in expressing their mercy, kindness and sympathy. I cannot reward them with these few words but I wrote these words to partially honor them in such occasion where their role is not visible but valuable. My parents: “I will never ever hesitate to impress you and serve you with all the skills that Allah granted me till I die and leave this life!”.

Also, I am very grateful for the patient guidance, valuable advices and the endless support and encouragement given by my supervisor Professor David Wright, Director of Research, and my external supervisor Professor Nasser Qaddoumi, Director of the Microwave Imaging and Nondestructive Evaluation Laboratory (*minel*) at the American University of Sharjah (AUS), UAE. Thanks a lot for every minute they spent, for every paper they signed and read, for every meeting they attended, for every decision they made, for every effort they did and for all the constructive advices they gave.

I would also like to express my gratitude to His Highness Sheikh Dr. Sultan Bin Mohammed Al Qassimi, Supreme Council Member, Ruler of Sharjah and President of American University of Sharjah, and Dr. Hamid Dhiya Jafar, the Chairman and CEO of the Crescent Petroleum Group of Companies, the Executive Chairman of Dana Gas PJSC, the Chairman of Gulftainer Ltd. and member of the Board of Trustees and Chairman of the Finance Committee of the American University of Sharjah (AUS), for their sponsoring and funding this research.

I would like to thank in particular Engineer Mohammed Abou-Khousa for helping me in developing the codes for the mathematical derivations of chapter 2 and everyone at *minel* for their help during this work. Also, I would like to express my gratitude to Dr. Moza Al-Shehhi, Vice Chancellor for Student Affairs at the American University of Sharjah, for her support, guidance and encouragement.

Finally, thanks to my two sons, Abd AlRahman (3 ½ years) and Abd AlRahim (1 ¾ years) for allowing me to conduct my research and not giving them enough time for their childhood.

# TABLE OF CONTENTS

## LIST OF FIGURES

## LIST OF TABLES

# *CHAPTER 1*

# *Introduction*

## *1.1 Background*

Non-destructive and non-invasive testing methods exploiting microwave sensors and probes for the intention of material examination are quite well established and have been applied to several media [Alt.63] [Arc.88] [Bah.82] [Bel.90] [Dec.74] [Lun.72] [Qad.95] [Qad.96a] [Qad.96b] [Sal.03b] [Sal.04a] [Sal.04b] [Sal.04c] [Sal.05a] [Sal.05b] [Sal.06] [Sal.07] [Ven.86] [Zou.90]. The increased use of composite materials for industrial, medical, and military applications presents quite a challenge to many non-destructive and non-invasive testing methods. Difficulties arise from the inherent anisotropy and physical property heterogeneities of these materials, as well as the relative high absorption and scattering of the radiated signals. The success achieved and the promising results obtained when utilizing near-field microwave non-destructive testing techniques in wide range of industrial applications such as corrosion detection, laminated composite inspection, surface crack detection and material characterization led researchers to adopt near-field microwave imaging for medical applications such as breast cancer detection [Hub.97] [Qad.95] [Qad.96a] [Qad.96b] [Ven.86] [Yeh.94] [Zou.90].

The spread of breast cancer worldwide and the critical need for new technologies to improve detection, diagnosis and treatment of breast cancer presents a challenge to most of the existing non-destructive and non-invasive testing methods.

Near-field microwave non-invasive testing and evaluation (NIT&E) techniques can be a successful candidate for the detection of breast cancer because of their potential in dealing with materials with low conductivity (i.e. lossy dielectrics like the breast tissue). Microwave NIT&E techniques are accomplished by transmitting an electromagnetic wave at a relatively high frequency towards a structure. The magnitude and/or phase information of the transmitted and/or reflected wave properties are measured to obtain information about the composition and the integrity of the structure. Such information can be a two dimensional image of the structure under inspection, line scans or a single point measurement. This can be done in a contact or non-contact fashion and either in the near-field or the far-field region. Further details and comparison between near-field and far-field regions are illustrated in section 4.2 of this thesis.

## *1.2 Motivation*

Microwave imaging and non-invasive testing of biological structures has been of interest for many years. Recently, microwave imaging and non-invasive testing has been applied to the detection of breast cancer [Fea.02] [Fea.00] [Hag.98] [Hag.99] [Li.01] [Sal.03b] [Sal.04a] [Sal.04b] [Sal.04c] [Sal.05a] [Sal.05b] [Sal.06] [Sal.07]. The physical basis and clue for tumour detection with microwave imaging and non-invasive testing techniques is the high contrast in dielectric properties between normal and malignant breast tissues. In the breast tissue, tumours may be divided into two groups (depending on the size with respect to the 'footprint' or sensing area of the microwave sensor), namely large and small tumours. A large tumour is a tumour whose area is several times larger than the footprint, and it can be considered as an extra layer in the breast. This layer can be detected and characterized using the measured reflection coefficient. If the tumour is small (i.e. its extent is smaller than the footprint),

it will have a different interaction with the fields, due to the boundaries and edges, and this interaction will influence the refection coefficient and consequently the signal measured by the microwave sensor. Detection of tumours in their early stages is a very important matter in order for the patient to be treated without any surgical operation or medical action that would negatively affect the patient's life. That is why it is of great importance to understand the interaction of the measurement probe with the breast under inspection.

## *1.3 The Biology of the Breast*

The intention behind this section is to describe the biological structure of the female breast, i.e. its anatomy. Understanding the physical and biological structure of the breast will aid in obtaining an optimal inspection system for breast cancer detection in its early stages since "early detection is your best protection" is the philosophy that guides almost all breast cancer screening programs and methods.

Figure 1-1 shows the anatomy of a female breast. The breast consists of glandular, fatty, and fibrous tissues located over the pectoral muscles of the chest wall. A layer of fatty tissue, which gives the breast a smooth texture, encloses the breast glands and extends throughout the breast. The glandular tissues of the breast accommodate the lobules (milk producing glands at the ends of the lobes) and the ducts (milk ways). The nipple is surrounded by the areola, a darker area. Glands in the areola produce fluid to lubricate the nipple during breastfeeding. The remainder of each breast is made up of surrounding fatty and connective tissue [Lov.95] [Web.1]. During lactation, milk moves through the ducts to the nipple to feed the newborn baby. Thus, the breast is mainly composed of:

1. Milk glands (lobules) that produce milk.

2. Ducts that transport milk from the milk glands (lobules) to the nipple.
3. Nipple.
4. Areola (dark pigmented region surrounding the nipple).
5. Tissues that surround the lobules and ducts.
6. Fat tissues.

The major parts of the female breast that are of great importance, for near-field microwave NIT&E techniques to be implemented effectively, are the skin, the breast tissue (mixture of fat, glands and blood) with the muscle and the tumour. This model will be adopted for theoretical investigation, simulation analysis and preclinical examination.

Further research on breast physiology and pathology may be needed in future, after showing the potential of near-field microwave NIT&E techniques in breast cancer detection, in order to address issues such as the precise functionality of the breast parts, at what stages there is a higher risk of breast cancer, what are the different lesions that are non-cancerous, the size of the breast as compared to age, the volume fraction of each part of the breast compared to the whole breast etc.. A quick overview of these issues is illustrated in the next section.

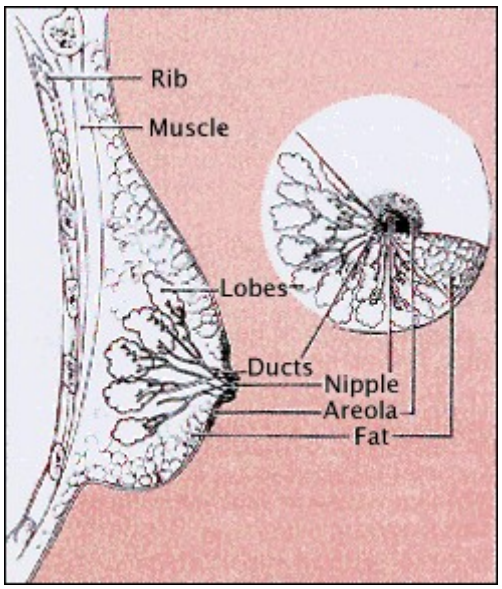


Figure 1-1: Female breast anatomy [Web.1].

## *1.4 Physiology and Pathology of the Breast*

Further discussion on breast physiology and pathology with the various benign and malignant lesions of the breast is presented in this section. These are important issues that have to be addressed because there will be physical and biological changes in the breast throughout a woman's life that will have an impact on the electrical (microwave) properties of the breast. Progesterone and oestrogen hormones play a key role in the growth and development of the female breast tissue, beginning at puberty. At this time, fat and fibrous tissue becomes stretchier and the breast ducts begin to grow. This growth carries on until menstruation begins, normally one or two years after breast development has started [Web.1].

A woman's breasts are infrequently symmetrical. Mostly, one breast is to some extent larger or smaller, higher or lower, or looks in some way slightly different to the other. The physical size and characteristics of the nipple also differ from one woman to another. As a woman gets older, the structure and the appearance of the breast keep on changing. In young women, the breast skin stretches and gets bigger as the breast grows resulting in a rounded appearance. Young women tend to have denser breasts than older women because of the more glandular tissue they have [Tav.99] [Web.1]. Throughout each menstruation, the breast tissue has a tendency to swell as a consequence of changes in the oestrogen and progesterone hormone levels. The milk glands and ducts expand and the breasts maintain more water. During the menstrual cycle, breasts may temporarily feel distended, painful or aching. The effect of this on near-field microwave imaging is that the dielectric properties of the tissue are likely to change over the course of the menstrual cycle because of the water retention. Thus, the patient is advised either to be scanned at the same point in her menstrual cycle or to be scanned when she does

not have menstruation to have a unique and consistent uniform background (healthy breast) during the imaging mechanism for routine screening.

There are many lesions and conditions that are non-cancerous but still affect the health of the breast and could be mistaken for cancer. They are as follows [Tav.99] [Kot.03] [Gur.06]:

1. *Fibroadenoma*: is a fibrous lump of tissue that exists normally in young women whose ages range between 20 and 30 years. They are due to an increased sensitivity to the oestrogen hormone. They move easily under the skin and are fairly obvious. They are harmless in themselves but painful at the same time. Most of the time fibroadenomas will not change in size over time and hence are just left alone. But in some cases mainly during pregnancy or breast-feeding they can become larger. If this is the case or they are really painful then surgery may be needed to remove them.
2. *Cyst*: is an irregular membranous sac including a fluid or semisolid substance that builds up within the breast tissue. Again, they are blatant and are not harmful. They most frequently occur in the upper half of the breast.
3. *Mastalgia*: is the breast pain and is usually categorized as either cyclical (linked with menstrual periods) or noncyclic. Noncyclic pain may come from the breast or may come from close muscles or joints and may be felt in the breast. Pain can vary from minimal discomfort to serious intolerable pain in some cases. Many women having mastalgia be anxious of having cancer rather than the pain itself.
4. *Calcification*: is a small deposit of calcium salts. It can take place with other benign breast conditions such as fibroadenomas and cysts or as a reaction to irritation and foreign bodies. Big calcifications, called macrocalcifications, are generally not related to cancer. Groups of small calcifications grouped together, called clusters of microcalcifications, are associated with extra breast cell activity. Calcification is ordinary and in most cases is harmless. However, it can be a sign of breast cancer.

5. *Mammary Duct Ectasia*: is one of the most common causes of abnormal nipple discharge. One or more of the ducts underneath the nipple becomes reddened and congested with a thick, sticky, green or black substance. Most often, mammary duct ectasia affects women in their forties and fifties. It can be recognized by an obvious lump behind the nipple or by the appearance of scar tissue behind the nipple, which can then cause the nipple to invert.
6. *Periductal Mastitis*: this is a condition where non-dilated breast ducts around the nipple become infected. It most commonly affects young women. The breast may be tender, the nipple becomes inflamed or infected and it has similar symptoms to duct ectasia.
7. *Fat Necrosis*: is another benign breast condition in which the neutral fats in the cells of adipose tissue break down into fatty acids and glycerol. It causes the formation of a firm, round lump and mainly occurs in an area of fatty breast tissue that has been injured. The lump is mostly painless, and the skin around it may look red or black-and-blue.
8. *Hyperplasia*: is caused by an abnormal growth in the size and number of normal cells within a part of the breast. It can occur in the ducts, hence called ductal hyperplasia, or in the lobes, so called lobular hyperplasia. Sometimes the cells extend in an irregular pattern and these are known as atypical ductal hyperplasia and atypical lobular hyperplasia. If these cell changes in the lobes are very irregular, the condition is known as lobular carcinoma in situ (LCIS) and if they occur in the ducts, then the benign condition is known as ductal carcinoma in situ (DCIS). This is not a real cancer (carcinoma) but a middle stage where the abnormal cells fill up the lobes or the ducts.
9. *Intraductal Papilloma*: is a benign lump within a duct that takes shape behind the areola. It will result into a small lump beneath the areola or discharge of clear, sticky or bloody fluid from the nipple. It can happen in both breasts simultaneously.

10. *Phyllodes Tumour*: is an uncommon type of breast lesion that can grow to be very large. It can affect a woman at any time in her life, but usually occur in women between forty and fifty years old who have not yet been through the menopause. It is categorized into three groups: benign (most frequent), borderline malignant and malignant.
11. *Sclerosing Adenosis*: is a benign condition where extra tissue grows within the breast lobules. This can cause persistent pain or result in a small solid lump in the breast.

The above described lesions are in general non-cancerous. Whereas when malignant lesions are described, cancer is sought. Cancer is an uncontrollable cell division that occurs because of mutation in the DNA of the cells. The cells divide so rapidly that they eventually kill and replace the surrounding normal tissue. There are several different types of tumours that can affect the breast. Around 70% - 80% of breast cancers are ductal carcinomas connected to the milk ducts, 10% - 15% are lobular carcinomas connected to the lobes, and the rest are relatively uncommon types of cancer such as of the connective tissue. While the cancer stays in the duct or lobule it is known as localised cancer, which is easier to treat and easier to detect. But it can expand beyond the duct or lobule into the surrounding tissue. As tumours expand, some develop the capability to produce their own capillary system of blood vessels and the water content inside the tumours becomes high compared to the healthy breast tissue. This development is defined as vascularisation and is linked to the fast tumour growth and the ability for a tumour to metastasize (spread through the breast and even the body), when tumour cells travel to other parts of the body. Due to the high-water content of tumours, the dielectric properties become much higher than the healthy breast tissue and thus there exists a distinct dielectric contrast between the malignant tumour and the breast tissue [Mur.94] [Hag.98] [Hag.99] [Tav.99], and it is this contrast that is exploited in near-field microwave imaging and detection.

## *1.5 Risk Factors and Symptoms of Breast Cancer*

Breast cancer remains a leading cause of cancer deaths among women in many parts of the world. Cancer is an uncontrollable cell division that occurs because of mutation in the DNA (DeoxyriboNucleic Acid) of the cells. The cells divide so rapidly that they eventually kill and replace the surrounding normal tissue. Breast cancer originates in the breast tissue and can spread around the body (a malignant cancer). Breast cancer can produce red inflammations of the breast, a discharge of blood from the nipples, the nipple turning inward, and cause pain. Despite this, there is a risk that the cancer will spread in the lymph nodes even before the symptoms become visible. A medical expert has to examine the symptoms and carry out physical examination to judge the presence and spread of breast cancer. There are several risk factors that cause breast cancer. The following list includes the majority of the known risk factors and/or causes of breast cancer [Par.96] [Hen.93] [Bri.96] [Mir.71] [Web.1]:

- *Age*: As a woman's age increases, the possibility of having breast cancer increases as well. It has been reported that the highest number of women having breast cancer is diagnosed in the 50-64 age group as shown in Figure 1-2 [Off.05] [Web.2]. Also, it has been stated that in the UK, the age-standardised incidence of breast cancer per 100,000 women increased from 75 in 1979 to 116 in 2002 as shown in Figure 1-3. Over the twenty year period from 1983 to 2002, the incidence rate increased by 45%.
- *Family history*: In general, women who have close relative (a mother or a sister) who has or had breast cancer, have a greater risk of developing breast cancer.
- *Induced abortion (in young women)*: There are several extensive investigations indicating that women who had an induced abortion at a young age have an increased risk of breast cancer.

- *Parity (how many children a woman has)*: Numerous studies have noted that the risk of breast cancer declines as a woman has more children. In general, women who have more children have a lower risk of breast and ovarian cancer. Women who have five or more children have about a 50% decreased risk of breast cancer. On the contrary, women who do not have children at all have about double the risk of attaining breast cancer.
- *Age at first birth*: Researchers have observed that the risk in mothers who give birth at a young age (under the age of 20) is about one half to one third of that of women who deliver their firstborn child after the age of 35. The main reason for this is thought to be that when a younger woman has a child, the cells in the small ducts of her breast mature and are less sensitive to cancer producing agents.
- *Previous personal history of breast cancer*: Women who had already one breast cancer before have a possibility of 25% to have a second breast cancer.
- *Long-term breastfeeding*: It has been stated by researchers that women who breast fed for more than 4 months in their lifetime, had at least a 22% decreased risk of breast cancer. In another study, it is noted that women who breast fed for more than 13 months had a 55% decreased risk. In general, breastfeeding (lactation) appears to reduce the risk of breast cancer in women.
- *Alcohol*: Alcohol is hypothesized to cause breast cancer by raising a woman's oestrogen levels.
- *Obesity*: Women who are overweight have an increased risk of developing breast cancer, due to the fact that fat tissues augment the level of oestrogen in the blood.

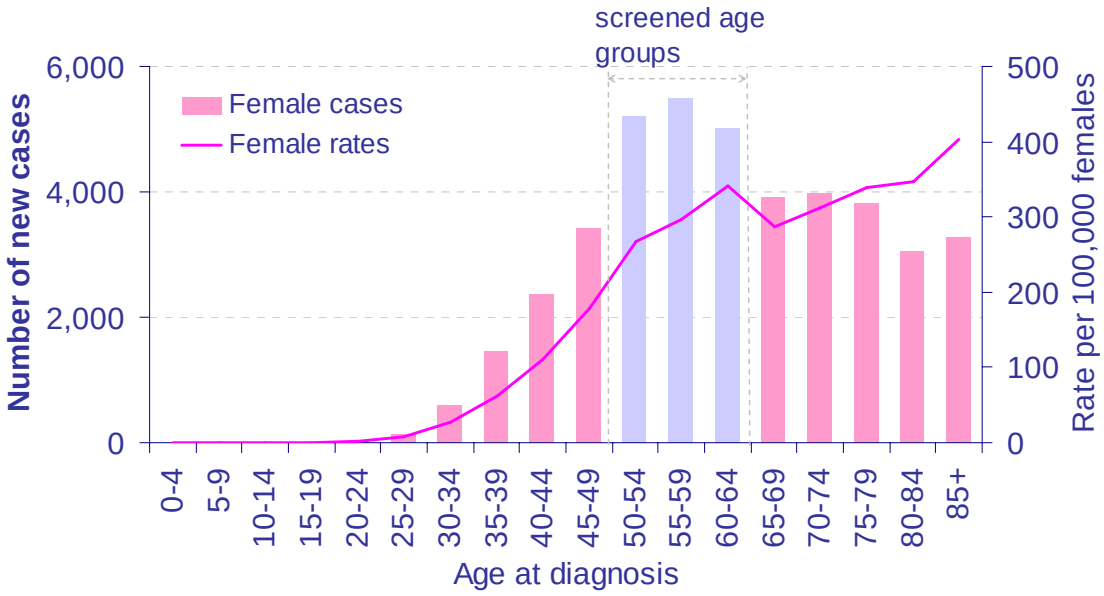


Figure 1-2: Number of new cases and age-specific incidence rates for female breast cancer, UK, 2002 [Web.2].

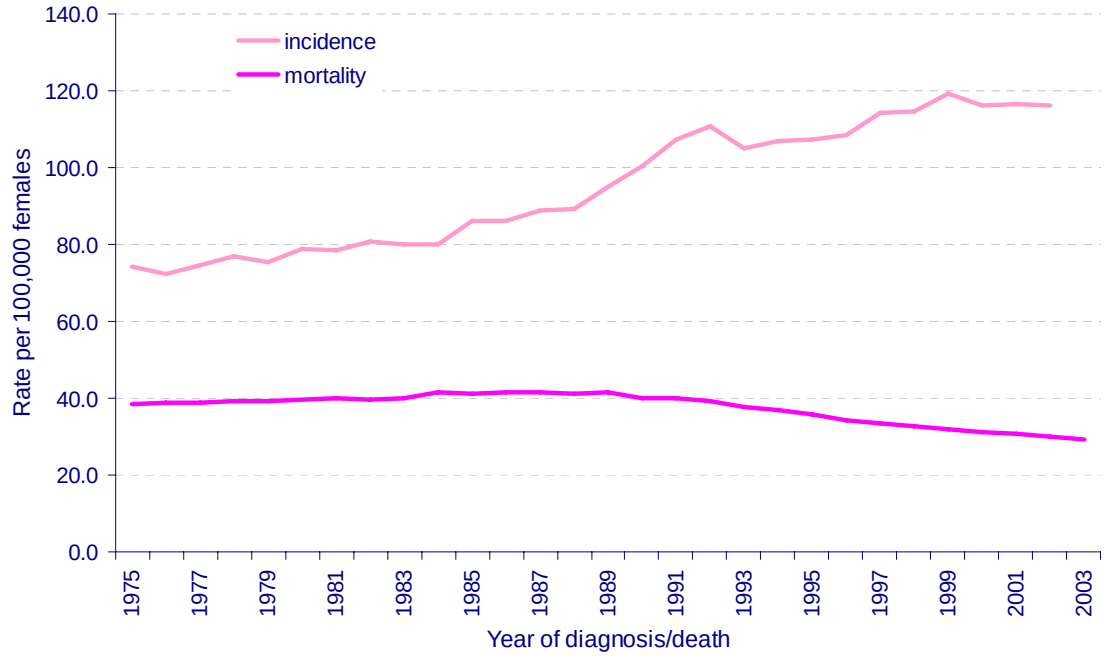


Figure 1-3: Female breast cancer incidence and mortality trends in UK [Web.2].

## *1.6 Existing Breast Screening Techniques*

Extensive research and investigations for breast cancer detection have been conducted by many research groups worldwide. Also, many techniques and screening programs have been adopted by these groups. The conventional, sequential stages in breast cancer screening are screening mammography, ultrasound, and finally biopsy. Screening mammography is conventionally an x-ray breast examination that is conducted on women that don't have any symptoms of breast cancer (asymptomatic). If a screening mammography shows any abnormality, additional breast imaging i.e. ultrasound (sonography) will usually be carried out. If a patient's ultrasound and x-ray results are both negative (no proof of cancer is seen), but the medical doctor is still concerned about the lump or mass, the woman may be referred to biopsy to determine whether she has breast cancer or not. Breast biopsy is the removal a sample of breast tissue to determine whether it is cancerous or benign (non-cancerous) and it is conducted by a surgeon. Pathological (microscopic) analysis conducted by a pathologist followed biopsy to determine if cancer is present or not. A brief description of the existing breast cancer diagnostic techniques with their advantages and limitations will be presented in this section.

X-ray mammography is considered to be the most conventional method utilized by doctors for breast cancer examination [Bre.82] [Wat.92] [Paq.00] [Web.03] [Fin.05]. This technique involves compressing the breast between two plates. Radiations, namely X-rays, are then passed through the breast and recorded onto film. An X-ray mammography imaging system is shown in Figure 1-4. Some latest improvements have been attained to enhance X-ray mammography. These are digital mammography and computer aided detection (CAD). But these enhancements are not broadly used because of their high cost compared to their partial progress to cancer detection rates. Also, X-ray mammography uses ionising radiation which is hazardous and compresses the breast

which may be painful to the patient. Conversely, X-ray mammography offers many advantages such as high detection sensitivity compared to other techniques, and the imaging execution time is fast as well.


Figure 1-4: X-ray mammography imaging unit [Web.3].

Ultrasound testing is the use of ultrasonic waves for diagnostic purposes, particularly to image an internal body structure such as the breast. No harmful radiation is involved in ultrasound imaging. The frequency range used in medical ultrasound imaging is from 1 MHz to 15 MHz. Ultrasound is used to determine whether a suspicious area lesion detected on a mammogram is a liquid cyst (always non-cancerous) or an increased mass of solid tissue which may require a biopsy to determine if it is malignant (cancerous) [Kre.98] [Bus.99] [Web.03]. Moreover, ultrasound offers significant freedom in imaging the breast from almost any orientation. The ultrasound signal may be generated and detected by a hand-held transducer as shown in Figure 1-5.

Figure 1-5: Ultrasound hand-held transducer.

Magnetic Resonance Imaging (MRI) is a non-invasive screening tool that employs powerful magnets and radio waves to construct images of the body. MRI is a non-invasive imaging technique that is able to differentiate between soft tissue. The scanner must be placed in a special shielded room to avoid outside interference because MRI operates at a high frequency close to FM radio frequencies. The patient has to lie down on a narrow table which slides into a large tube-like channel within the scanner as shown in Figure 1-6. Additionally, small devices may be placed around the breast to be examined. These are special body coils which transmit and receive radio wave pulses, and are intended to enhance the quality of the images. Several sets of images are usually required. A complete scan may take up to one hour. There is no pain and the magnetic fields and radio waves are not felt. The main probable discomfort is the claustrophobic feeling that some patients suffer from being inside the scanner. The machine produces loud thumping and humming noises during normal operation. Ear caps are given to the patient to reduce the noise [Sta.92] [Has.97] [Bro.99] [Web.1].

Figure 1-6: MRI unit [Web.3].

Another screening tool for breast cancer detection is nuclear medicine imaging (scintimammography). Small amounts of radioactive materials, called radiopharmaceuticals, are used by nuclear medicine imaging. A nuclear medicine breast imaging examination takes roughly 45 minutes to one hour. To conduct the exam, a radioactive tracer, explicitly Tc-99m sestamibi, is injected in the patient's arm. Then the patient is instructed to lie face down on a special table while the breast hangs down through a hole in the table as shown in Figure 1-7. Roughly five minutes afterwards, many images of the breast with various orientations are taken with a special gamma camera [Met.98] [Thr.01] [Web.1].

The above mentioned screening tools exist and are commercially available, but there are other diagnostic and imaging techniques that are under investigation. One of these imaging techniques is optical tomography. Optical tomography, known as Near-Infrared (NIR) imaging, offers a difference between tissues based on their optical properties obtained from transmitted light measurements. The measurable parameters that are of interest in optical tomography are the absorption and the scatter properties of the breast that is under inspection. The absorption and the scatter properties are represented with their coefficients, $\mu_a$ and $\mu_s$ respectively. Optical techniques offer the

following features: (a) the utilization of nonionizing radiation, (b) the potential of measuring physiological parameters, (c) the high sensitivity to the molecular conformation of biological tissues, and (d) low cost. But still further research and investigations are required to enable optical tomography to be a conventional screening tool for breast cancer detection [Wan.98] [Col.99] [Jia.01] [Deh.03] [Deh.04] [Deh.05] [Gib.05] [Heb.05] [Yat.05a] [Yat.05b] [Yat.05c] [Sub.06] [Wan.06].

Other screening techniques involve electrical impedance tomography (EIT) (based on the tissues different conductivities), and thermography. Other diagnostic methods include biopsy (removal and examination of a sample of tissue from the breast for diagnostic purposes), self-examination and ductal lavage (tissue analysis that have been washed out from the breast ducts using a breast pump). Further details of these diagnostic and imaging techniques are described in [Moo.01] [Gro.80] [Nyi.86] [Rad.99] [Web.1].

Figure 1-7: Nuclear medicine imaging unit [Web.4].

In summary, the aforementioned existing screening tools with their advantages and disadvantages are as follows [Bre.82] [Sta.92] [Wat.92] [Has.97] [Kre.98] [Met.98] [Bro.99] [Bus.99] [Paq.00] [Thr.01] [Web.03] [Fin.05] [Web.1]:

1. **X-ray Mammography:**
    a. *Advantages:*
        i. High-quality resolution, microcalcifications can be detected easily.
        ii. Good sensitivity.
        iii. Execution imaging time is short.
    b. *Disadvantages:*
        i. Hazardous because ionising radiation is employed.
        ii. Breast compression which is painful for the patient.
        iii. Low detection sensitivity for patient with dense breast tissue (young women).
        iv. Mammogram interpretation is hard because of the dissimilarities in the physical appearance of the breast for each patient.
        v. Breast implantation (such as silicone implants) might corrupt the mammography accuracy.
2. **Ultrasound:**
    a. *Advantages:*
        i. Image contrast and resolution is high which yields a high distinction between normal tissue and suspicious areas.
        ii. Detection and examination for young women with dense breasts and women with breast implants are applicable.
        iii. Safe screening tool because there is no harmful radiation.
    b. *Disadvantages:*
        i. Microcalcifications can't be easily detected.
        ii. System performance is dependent on the technician's skills and the operator expertise.

iii. Some solid masses cannot be distinguished.

iv. Deep lying lesions can barely be detected.

**3. Magnetic Resonance Imaging (MRI):**

*a. Advantages:*

i. Patients with dense breasts can be examined effectively using MRI.

ii. Non-ionising imaging technique.

iii. Images can be captured from various angles.

iv. Detection sensitivity to small abnormalities is high.

v. Multi-focal cancers can be detected.

vi. Helpful in determining if the cancer reaches the chest wall.

vii. Return of cancer can be inspected in patients who have experienced lumpectomy (surgical removal of a tumour from the breast with the exclusion of a minimal amount of surrounding tissue).

viii. Breast implants and ruptures can be detected.

*b. Disadvantages:*

i. Extremely expensive.

ii. Immobile and fixed.

iii. Injection of a contrast agent for operative testing is needed.

iv. Calcifications cannot be detected.

v. Feelings of claustrophobia (an abnormal fear of being in narrow or enclosed spaces) can be produced.

vi. Imaging and scanning execution time is lengthy comparing to ultrasound and X-ray mammography.

**4. Nuclear Medicine Imaging (Scintimammography):**

*a. Advantages:*

i. Patients with dense breasts can be examined effectively as MRI.
ii. Large lesions that cannot be inspected by other testing methods can be detected.
iii. Multi-focal cancers can be detected.
iv. Although nuclear medicine is invasive, tissue testing can be performed without mastectomy (surgical removal of all or part of the breast) as opposed to biopsy where removal and examination of a sample of tissue from the breast for diagnostic purposes is performed.
v. Metastases (cancer that starts from cancer cells that come from a different location in the body) in the auxiliary lymph nodes can be tested.

*b. Disadvantages:*

i. Ionising radiation.
ii. Invasive.
iii. Testing and scanning procedure is time-consuming.
iv. Accuracy is not high when detecting small defects.

## *1.7 Previous Research Findings*

With the improvement in imaging techniques, microwave equipment, image reconstruction algorithms, computational methods, and increased computing power, recent advances in microwave imaging have been significant. Many investigations of the use of microwave imaging have been conducted to detect the presence of breast tumours. These investigations explore breast imaging with passive, hybrid and active methods [Fea.02].

In the passive method, microwave radiometry is exploited to measure temperature differences in the breast leading to the detection of tumours based on their increased temperature compared to normal tissue [Car.00]. A research team in France developed a Dicke radiometer that utilizes six radiometers that operate in parallel to reduce the acquisition time [Mou.00].

In hybrid techniques, such as microwave-induced acoustic imaging, use is made of microwave energy to heat up the tumours. Due to the high conductivity of the malignant tissue, more microwave energy is accumulated in the tumours. Consequently, the tumour tissue will be heated and thus expand and produce pressure waves. Ultrasound transducers are then used to detect these pressure waves. Further details of this technique are given in [Kru.99a] [Kru.99b] [Wan.99].

Active microwave techniques illuminate the breast with microwaves and then the transmitted or reflected microwave signals are measured. The transmission or reflection measurements are then used to reconstruct the material properties of the breast. Such reconstruction may use a computed tomography (CT) approach, as developed by Miyakawa *et al.* [Miy.93]. This system isolates the signal travelling directly from the transmitting to the receiving antennas, using the frequency component of the signal corresponding to the distance between the antennas. Another approach to reconstructing the breast profile solves the inverse scattering problem exploiting iterative methods. This involves computing the received energy with a numerical method and estimating the material properties (the forward problem). Consequently, optimisation techniques are applied to vary material properties for a better match between the measured and computed data. In 1999, Paulsen *et al.* developed such a system that operates between 500-900 MHz, and consists of an array of monopole antennas [Mea.99] [Pau.99]. Yet another reconstruction approach is the use of hybrid finite-element boundary-element method to solve the forward problem, and then Newton-Raphson iterative method is applied to solve the inverse-scattering problem.

Moreover, Franchois *et al.* have developed a 2.45 GHz microwave camera, which consists of transmitting and receiving horns, with an array of 32x32 small dipoles located in the receiving horn [Fra.98]. The method of moments (MoM) combined with the distorted Born iterative approach was used in image reconstruction.

Another system developed in 1998 by Souvorov *et al.* consisted of an object placed in a water bath and surrounded by 32 transceivers operating at 2.45 GHz [Sou.98]. Measurements are made at the 16 antennas located across from the excited antenna. To reconstruct images, a fast iterative method was used for the direct solution, and the Newton iterative method is applied to the inverse solution. In 1998, Chew developed a time-domain approach that includes the finite-difference-time-domain (FDTD) method in the distorted-Born iterative method to reconstruct images [Che.98b]. This was combined with time-domain impulse radar to produce a system for non-destructive testing [Che.98a]. Yet another approach was introduced by Hagness *et al.* where a pulsed microwave confocal system was introduced to detect tumours [Hag.98] [Hag.99]. Both two- and three-dimensional (2-D and 3-D) simulations were conducted with the finite-difference-time-domain (FDTD) method. In both cases antennas were placed on a flattened breast model.

The approach adopted in this thesis to detect breast cancer differs from previous and abovementioned microwave imaging techniques in many aspects. It involves studying the theoretical foundation of the interaction of the microwave signals radiated from an open-ended rectangular waveguide probe with the breast under inspection in the near-field region. Other factors such as the polarization properties of microwave signals, the physical structure of the microwave sensor and the loading of the microwave sensor are studied as well. Also, it adopts an alternative electromagnetic numerical technique, namely Fourier Transform Matching (FTM) technique. This technique allows calculation of the magnitude and phase of the reflection coefficient at the waveguide aperture explicitly. Moreover experimental investigations are also

performed measuring the magnitude and phase of the reflection coefficient at the waveguide aperture using the slotted waveguide reflection measurement setup, as shown in chapter 5 of this thesis.

It has been recognized that an open-ended rectangular waveguide probe operating at a certain frequency, polarization and excitation mode can be effectively used for defect (void) detection and imaging in composite structures, for corrosion detection as well as crack detection within metallic structures [Bak.92] [Bak.93] [Bak.95] [Hub.97] [Qad.97] [Qad.98b] [Qad.00] [Sal.01] [Yeh.94]. In addition, it has been established that an open-ended rectangular waveguide probe can be successfully used for inclusion (tumour) detection and classification as well in this thesis [Sal.03b] [Sal.04] [Sal.05] [Sal.06] [Sal.07]. A homogeneous dielectric structure without an inclusion (tumour) provides a certain reflection coefficient at the aperture of the waveguide. The presence of a tumour (i.e. heterogeneity) will cause the reflection coefficient to be altered. Thus, the study of the reflection properties, as the structure is being scanned by an open-ended waveguide sensor, renders information about the existence of a tumour (detection).

The ability of microwaves to penetrate inside dielectric materials and interact with their inner structure makes them an excellent candidate for non-invasive and non-ionising inspection of dielectric media and tumours. Near-field microwave NIT&E techniques offer novel solutions when inspecting breast tissue for the purpose of detecting tumours. Microwave techniques do not require a couplant, and can effectively and smoothly scan the breast in contact and/or non-contact fashions (i.e. at some standoff distance). Furthermore, as shown in this thesis, optimising the frequency of operation, the standoff distance and/or the waveguide filling have been shown to significantly improve measurement sensitivity when detecting tumours in breast tissue [Sal.03b] [Sal.04a] [Sal.04b] [Sal.04c] [Sal.05a] [Sal.05b] [Sal.06] [Sal.07].

To date, a general model that considers the near-field radiation and reflection properties of the rectangular waveguide sensor radiating into N-layer dielectric material has not been investigated in-depth. Furthermore, a detailed analysis that describes the interaction model between microwaves and the breast material under inspection has not been investigated and a detailed theoretical formulation of the imaging mechanism between the microwave sensor and the material under inspection has not been presented. However, the use of an open-ended rectangular waveguide as a sensor for measuring material properties at microwave frequencies has received significant interest. The analysis of near-field radiation properties of an open-ended rectangular waveguide radiating into an infinite half-space of a dielectric was studied by other researchers [Bov.89] [Nik.89] [Zou.90] [Bak.95] [Qad.98a]. The majority of the endeavours carried out in this field have discussed various methods for designing waveguides and not the interaction of the electromagnetic waves with N-layer dielectric structure [Ste.77] [Mar.70] [Her.83] [Kor.82] [Kir.94]. In this thesis, the interaction between microwaves radiated from an open-ended rectangular waveguide sensor and the breast will be investigated, simulated and analyzed (forward problem). Then, the potential of exploiting open-ended rectangular waveguide probe for breast cancer imaging will be demonstrated. The high quality images obtained demonstrate that tumour detection may be achieved without the need for complicated signal-processing techniques or solving the inverse problem.

## *1.8 Potential Impact and Benefits*

Microwave NIT&E techniques present attractive advantages over other techniques for inspecting tumours in breast. Microwave breast imaging is appealing because both ionising radiation and breast compressions are avoided. Also, microwave imaging is non-invasive and a harmless screening tool. Microwave imaging is based on transmitting a microwave signal into a dielectric structure (breast) and using the magnitude and/or phase information of the transmitted and/or the reflected signal to obtain a line scan, a two or three dimensional image of the breast. This can be done in contact, non-contact and either in the near- or the far-field regions. Near-field microwave imaging uses simple probes such as open-ended rectangular waveguide probes and coaxial lines, whereas far-field imaging needs an antenna for focusing the microwave energy. In the near-field region, images can be obtained using either phase or magnitude information. Far-field techniques generally use magnitude information. Near-field microwave imaging is more adaptable since complex (phase and/or magnitude) images are easily produced and often contain more or complimentary information than amplitude imaging [Gop.94]. The output signals of these microwave sensors are easy to interpret and minimal operator skills are required. Furthermore, unlike some alternative technologies, microwave imaging techniques require no coupling agent, do not need surgical operation, do not suffer from high signal attenuation, are relatively inexpensive and they are not time-consuming.

Microwave non-invasive testing and evaluation techniques may be exploited for regular examination of different tumours and may be adapted to on-line concurrent detection environments. These characteristics enhance the detection capability of breast cancer in its early stages and increase the validity of self-examination. Generally, a near-field microwave detection/inspection technique requires simple hardware and minimum operator expertise. The measurement system can be battery operated,

handheld and the measurements can be conducted on-line and in real time [Bak.92] [Sal.03b] [Sal.04a] [Sal.04b] [Sal.05a] [Sal.05b] [Sal.06] [Sal.07].

Furthermore, microwave imaging in general and near-field microwave non-invasive testing and evaluation techniques in particular are safer and less likely to induce patient anxiety compared to some alternatives. The coupled power has been comprehensively examined and analyzed for applications such as mobile phones and hyperthermia. Safety standards (such as IEEE Standard C95.1-1999: IEEE Standard Safety Levels with Respect to Human Exposure to Radio Frequency Electromagnetic Fields, 3 KHz to 300 GHz) have been described based on maximum allowable exposure using quantities like the specific absorption rate (SAR) and the effect of electric and magnetic fields in the body [Gan.01] [Poz.05]. SAR is a measure of the rate at which RF energy is absorbed by a certain volume of a biological tissue when using microwave equipment. It is defined as:

$$SAR = \frac{dW}{\rho dV} = \frac{\sigma E^2}{\rho} \tag{1.1}$$

where $dW$ is incremental energy, $dV$ is volume element and $\rho$ is the density of the material (kg/m$^3$) in volume $dV$, $\sigma$ is the tissue conductivity (S/m), $E$ is the rms electric field strength induced in the tissue (V/m). SAR has units of W/kg. IEEE Standard C95.1-1999 specifies that acceptable apparatus operating between 100 KHz and 6 GHz should have maximum SAR over the body less than 1.6 W/kg when averaged over 1g of tissue. Results obtained by Gandhi *et al.* show that radiated power of 121 mW is required to obtain 1.6 W/kg SAR at 1900 MHz [Gan.01]. The proposed microwave inspection system in this research will operate in the few milliwatts range, and thus microwave testing and imaging is not expected to cause any health risk or threat to the patient.

Finally, from a financial point of view, microwave inspection systems are inexpensive and economical when compared to other screening and testing tools and

methods such as MRI and nuclear medicine imaging. The reason behind this is that microwave components cost a small fraction of the equipment needed for MRI or nuclear medicine.

## *1.9 Basic Electromagnetic Wave Concepts*

### *1.9.1 Plane Waves and Characteristic Impedance*

The propagation of electromagnetic waves in linear media is governed by Maxwell's equations [Sad.95]. These equations are the differential equations for the vector components of the electric and magnetic fields, and the equations take different forms depending on which orthogonal coordinate system (Cartesian, spherical, etc.) is used in expressing the vector fields. It is convenient to restrict ourselves to fields that vary with time according to the complex exponential function (harmonic) $e^{j\omega t}$ where $j = \sqrt{-1}$, $\omega$ is the angular frequency, and $t$ is the time. There is little loss of generality in using such a time function since any physically realizable time variation can be decomposed into a spectrum of such functions by means of the Fourier integral [Bra.65]. Also, in practice, microwave sources typically generate sinusoidal signals.

Plane waves are defined to have no spatial variation in the plane transverse to the direction of propagation. Also, they are time-harmonic (or sinusoidal) because time dependence $e^{j\omega t}$ is assumed, i.e. time variation is ignored [Sad.95]. Taking the z-direction as the direction of propagation, the differential equation (wave equation) for the transverse electric-field vector, $\overline{E_t}$ in the x-y plane is

$$\frac{d^2\overline{E_t}}{dz^2} + k^2\overline{E_t} = 0 \qquad (1.2)$$

where $k^2 = \omega^2 \mu_c \varepsilon_c$, and $\mu_c$ and $\varepsilon_c$ are the complex permeability and complex permittivity of the medium [Poz.05]. The solution of this equation has the form $A^{\pm} e^{\mp jkz}$ where $A^{\pm}$ are complex coefficients that are determined by boundary conditions. Since a time function $e^{j\omega t}$ was assumed, $A^{+} e^{-jkz}$ represents propagation along the positive z-axis and the other solution represents propagation in the opposite direction (e.g., a wave reflected from a material boundary). The propagation constant or wave number, *k*, is given by

$$k = \omega\sqrt{\mu\varepsilon} = \frac{\omega}{v_c} = \frac{2\pi f}{v_c} = \frac{2\pi}{\lambda} \tag{1.3}$$

where $v_c$ is the phase velocity of electromagnetic waves in a medium with parameters $\mu$ and $\varepsilon$, and $\lambda$ is the wavelength corresponding to frequency *f* in the same medium. The magnetic fields associated with these forward- and backward-propagating waves are perpendicular to the corresponding electric fields and are given by

$$\begin{aligned} H_x &= \mp \frac{E_y}{\eta} \\ H_y &= \pm \frac{E_x}{\eta} \end{aligned} \tag{1.4}$$

The factor

$$\eta = \sqrt{\frac{\mu}{\varepsilon}} \tag{1.5}$$

has the dimensions of ohms and is called the characteristic or intrinsic impedance of the medium. In free space (vacuum) it is equal to $120\pi \approx 377$ ohms. For uniform plane waves, the electric and magnetic fields are orthogonal to each other as well as to the direction of propagation (transverse electromagnetic (TEM) waves). Consequently, the vector cross product between the electric and magnetic field vectors, ($\overline{E_t} \times \overline{H_t}$), points in the direction of propagation.

### *1.9.2 Standing Waves and Standing Wave Ratio (SWR)*

Consider the case where two plane waves, having the same electric-field components with different complex amplitudes, are travelling in opposite directions. The total electric field at a point in space is then just the sum of the electric fields in the two waves, i.e.,

$$E_{total=} E_1 e^{-jkz} + E_2 e^{jkz} \tag{1.6}$$

where the harmonic temporal variation, $e^{j\omega t}$, has been omitted for convenience. If the magnitude of the total electric field is computed (assuming $|E_2| \le |E_1|$) then it varies as the *cos(2kz)* and has a maximum and minimum value of $|E_1| + |E_2|$ and $|E_1| - |E_2|$, respectively. Shifting the phase of one of the waves with respect to the other causes the positions of these extremes to shift along *z*. This varying amplitude pattern caused by interference between the two waves is called the standing-wave pattern and the ratio

$$SWR = \frac{|E_1| + |E_2|}{|E_1| - |E_2|} \tag{1.7}$$

is called the standing-wave ratio. This standing-wave pattern repeats every one-half wavelength. Thus, if the amplitude and/or phase of one of the waves have been influenced by interaction with a material or structure, direct measurements of the corresponding standing-wave pattern (magnitude and extreme positions) will contain information about that material or structure.

## *1.10 Open-Ended Rectangular Waveguide*

Open-ended rectangular waveguides are hollow tubes with rectangular cross sections. Open-ended rectangular waveguides are one of the primary types of transmission lines and allow for propagation of microwave signals without producing much signal attenuation. They can propagate transverse electric (TE) or transverse magnetic (TM) fields, but cannot propagate transverse electromagnetic (TEM) fields. This is because the waveguides are single conductor transmission lines and the TE and TM modes result from the solution of Maxwell's equations given the boundary conditions inside a waveguide.

Open-ended rectangular waveguides have a cut-off frequency below which no signal can propagate. Therefore, a waveguide functions as a high pass filter. The mode with the lowest cut-off frequency is known as the dominant mode and it is known as $TE_{10}$. This is the mode at which waveguides operate when transferring a microwave signal from one point to another. Furthermore, to avoid the propagation of higher-order modes (i.e., other than the dominant mode) an upper frequency bound is given to each waveguide. This upper bound is at the cut-off frequency of the first higher-order mode that can be generated and it is given, for a waveguide with $a > b$, by:

$$f_{c_{10}} = \frac{k_c}{2\pi\sqrt{\mu\varepsilon}} = \frac{1}{2\sqrt{\mu\varepsilon}}\sqrt{\left(\frac{m\pi}{a}\right)^2 + \left(\frac{n\pi}{b}\right)^2} = \frac{1}{2a\sqrt{\mu\varepsilon}} \tag{1.8}$$

where $m = 1$ and $n = 0$ for the dominant mode $TE_{10}$, $a$ is the broad dimension of the waveguide, and $b$ is the narrow dimension of the waveguide, $\mu$ and $\varepsilon$ are the permeability and permittivity of the waveguide filling material [Poz.05].

Waveguides are also dispersive which means the phase velocity becomes a frequency dependent parameter. Therefore, to prevent excessive dispersion, the operating frequency band of a waveguide is usually 1.25 times the cut-off frequency of the dominant mode and extends to 0.95 of the cut-off frequency of the first higher-order

mode. For example, an X-band rectangular waveguide has a cut-off frequency of 6.557 GHz and an operating frequency range of 8.2 - 12.4 GHz. At this frequency band the waveguide cross-section is 2.286 cm by 1.016 cm.

Waveguide sections can be attached to other sections or waveguide-based microwave components and devices using a flange. Figure 1-8 shows several rectangular waveguides with flanges covering a frequency range of about 1 GHz (the waveguide with the largest cross-section) to 75 GHz (the waveguide with the smallest cross-section). Table 1-1 lists the frequently used microwave band letter designations and their respective operating frequency ranges and the waveguide designation for each band [Poz.05].

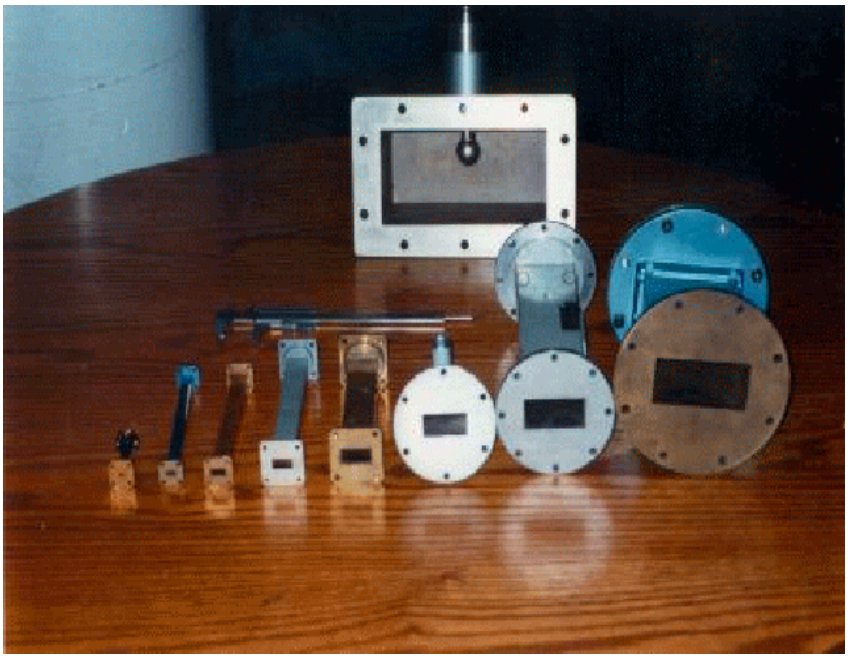

Figure 1-8: Several open-ended rectangular waveguides with different frequency bands.

Table 1-1: Microwave frequency band letter designation for the operating frequency of rectangular waveguides [Poz.05].

| Band | Frequency Range (GHz) | $TE_{10}$ Cut-off Frequency | Designation (WR-XX) |
|---|---|---|---|
| L | 1.12-1.70 | 0.908 | WR-650 |
| R | 1.70-2.60 | 1.372 | WR-430 |
| S | 2.60-3.95 | 2.078 | WR-284 |
| H (G) | 3.95-5.85 | 3.152 | WR-187 |
| C (J) | 5.85-8.2 | 4.301 | WR-137 |
| W (H) | 7.05-10.0 | 5.259 | WR-112 |
| X | 8.2-12.4 | 6.557 | WR-90 |
| Ku (P) | 12.4-18.0 | 9.486 | WR-62 |
| K | 18.0-26.5 | 14.047 | WR-42 |
| Ka (R) | 26.5-40.0 | 21.081 | WR-28 |
| Q | 33.0-50.5 | 26.342 | WR-22 |
| U | 40.0-60.0 | 31.357 | WR-19 |
| V | 50.0-75.0 | 39.863 | WR-15 |
| E | 60.0-90.0 | 48.350 | WR-12 |
| W | 75.0-110.0 | 59.010 | WR-10 |
| F | 90.0-140.0 | 73.840 | WR-8 |
| D | 110.0-170.0 | 90.854 | WR-6 |
| G | 140.0-220.0 | 115.750 | WR-5 |

## *1.11 Near-Field Microwave Theoretical Images*

An image is one of the best sources of information. Inspection of entities (tumours) in opaque mediums is a classical problem in medical and other imaging applications. Over many years, this problem has been inspiring scientists and engineers to develop sensors that can characterize such invisible entities. Most of the imaging systems existing nowadays are intended to address this problem in a wide range of applications; medical imaging, microscopy, material non-destructive evaluation and testing, etc. There are many techniques (modalities) used for imaging purposes within these applications. However, the basic principle of image formation for these techniques is quite similar; an image of an entity is formed as a result of the interaction between the imaging sensor and certain physical and/or chemical properties of that

entity. In essence, this applies for near-field microwave imaging of entities in various structures such as the breast.

A microwave image is obtained by arranging detected microwave signals/data, gathered by performing a raster scan over a structure, to produce a visual impression of the presence of defects or the structural geometry. The microwave data may include information such as the phase and/or the magnitude of either the reflection coefficient or the transmission coefficient. Also, attenuation information can be used to produce a microwave image of a structure as well as any combination of all of the above. The microwave sensor operates at a certain frequency and at a certain standoff distance (the physical distance between the waveguide probe aperture and the first layer of the material under inspection).

Near-field microwave waveguide-based imaging systems are powerful non-destructive and non-invasive evaluation tool. They are based on the basic idea that microwaves, once they are launched into a media, are very sensitive to discontinuities in the material space. A discontinuity could be practically realized as a tumour in a breast tissue. This discontinuity, defined as change in the spatial distribution of the dielectric properties, causes some change in the properties of the reflected and transmitted waves. The power and the phase properties of the forward and backward travelling waves contain valuable information about the type, location, and orientation of the discontinuities seen by the incident wave. Any system located outside the material space and utilized with the intention of measuring the properties of the transmitted and/or reflected microwaves for the purpose of extracting information about material discontinuities, and hence evaluating the material space, is intrinsically a microwave non-destructive and non-invasive evaluation system.

Generally, a near-field waveguide-based microwave imager is an imaging system that utilizes a waveguide as an imaging probe to measure the reflection coefficient in a certain imaging plane as a function of the spatial coordinates and output

that as 1-D line scan or 2-D intensity image. The fundamental objectives of this imager as a near-field microwave NIT&E technique are stated as follows:

a. Detection Problem: Detect a tumour (entity) in the breast such that, from the captured image, the existence of that tumour is guaranteed.
b. Inverse Problem: Assess the detected tumour thorough quantitative interpretation of the captured image to extract the tumour's physical and electrical properties.

Now, one should decide on the type of the images to be captured. Then, an optimization procedure should be carried out to facilitate the inverse problem solution - i.e. image interpretation- in the later stages and for future research. The reflection coefficient, Γ, is a complex parameter that depends directly on the properties of the material discontinuities. Using certain microwave circuitry, the phase and/or the magnitude of the reflection coefficient can be measured. According to the measured parameter, there are three types of images, and thus realizations of the near-field waveguide-based imagers:

I. *Phase Images*: are those intensity images in which the intensity at every spatial point is proportional to the phase of the reflection coefficient at that point. The waveguide is scanned in the imaging plane, and the phase of the reflection coefficient, $\phi$, or a signal proportional to it, will be measured at each scanned point. The dynamic range of the captured phase images span a portion in 180° degrees phase range. These images are captured to inspect surface or subsurface defects (deep tumours) in material structures (breast). For this type of inspection, the sensitivity of a phase image is quantified by the subtraction of the phase of the reflection coefficient between tumour presence and absence.

II. *Magnitude Images*: In a magnitude image, the intensity at each scanned point is proportional to the magnitude of the reflection coefficient. Since the magnitude of the reflection coefficient, Γ, has a range from zero to 1, the dynamic range of the magnitude

images span a portion of this range. Once more for this type of inspection, the sensitivity of a magnitude image is quantified by the subtraction of the magnitude of the reflection coefficient between tumour presence and absence.

III. *Complex Images*: are the simplest types to capture. The intensity at each point in the captured image is proportional to the complex reflection coefficient as a whole. Basically, these images do not convey phase or magnitude information exclusively. Thus, these types of images will be neither targeted theoretically nor experimentally.

The baseline or the reference imaging will be the healthy non-cancerous part of the breast itself, i.e. the uniform background when tumour is absent. This baseline is considered to be valid because the tumour is a localized anomaly.

## *1.12 Noise in Microwave Systems*

Noise can occur in a microwave system due to interference from external sources (extrinsic noise) or be generated within the system itself by the various electronic devices and components (intrinsic noise). Careful system design, for example by proper use of shielding and screening of electronic systems, should routinely be used to minimise the effects of extrinsic noise. Intrinsic noise is however always present and its main contributions are outlined below [Poz.05]:

1. *Thermal noise (Johnson or Nyquist noise*): is caused by thermal vibrations of charge carriers is a form of white noise (i.e. a flat power spectrum).
2. *Shot noise*: arises due to the fact that electric current involves the flow of discrete charges and is not an ideal smooth fluid-like flow; again, its spectrum is white.
3. *Flicker noise (1/f noise)*: is an additional (to thermal and shot noise) electronic noise that occurs in most electronic components and its power varies inversely with frequency, so that it becomes more significant at low frequencies.

In the simulation analysis, due to reasons of complexity, the effects of noise have in general being omitted. The level of noise present in any particular system will however determine the lower bound on the signal strength that can be detected in practice. In order to interpret properly the simulation results it is instructive to estimate typical lower bounds for signal detectability (i.e. the noise floor) in microwave systems of the type used in this thesis. The noise floor of the uncalibrated microwave measurement system presented in chapter 4 of this thesis is estimated to be around -70 dB, as shown in Figure 3-4 that represents the real power pattern as a function of z (direction of propagation) at different tumour depths. The noise floor arises here mainly from the Scalar Network Analyzer (SNA) [Agi.96c]. For the calibrated measurement system presented in chapter 5 the noise floor is typically less than 0.5μV for an output voltage of 100 mV and it is predominantly from the HP diode detector [Agi.96d]. This noise is considered to be very minimal (usually HP products have high dynamic range and low noise floor).

## *1.13 Breast Tissues Dielectric Properties*

At low frequencies, electromagnetic signals conveniently correspond to voltages and currents measured at points within a circuit. Radiation from a slowly varying current is negligible and all circuit elements are small compared to a wavelength (i.e. discrete). The ratio of voltage to current (called impedance) fully expresses the interaction of a source with a load. Conversely, microwave NIT&E technique is comprehended in terms of the interaction between waves (or fields) and breast tissues rather than in terms of voltages and currents. At microwave frequencies (300 MHz – 300 GHz) radiation effects can be significant and circuit elements are typically on the order of a wavelength or larger in size (i.e. distributed). At such high frequencies, it is

usually convenient and best to represent electromagnetic signals by waves. Impedance is still a useful concept, but now it is understood to be given by its more general definition as the ratio of certain electric- to magnetic-field components. Microwave NIT&E technique uses the fact that an electromagnetic wave will have its amplitude and/or phase (delay) changed by passing through, or scattering from, a material body like the breast. The amount of change in these measurable wave characteristics is dictated by the material's dielectric, magnetic, and geometric properties.

Breast tissue interactions with the electromagnetic fields are expressed by their dielectric properties. The dielectric properties of a generally lossy material such as breast tissue are represented by a complex parameter whose real part (permittivity) indicates its ability to store microwave energy and its imaginary part (loss factor) indicates its ability to absorb microwave energy (attenuation or amplitude loss) [Mub.01] [Poz.05]. Relative to the dielectric constant of free-space, the complex relative dielectric property of a tissue is denoted by:

$$\varepsilon_c = \varepsilon_r - j\varepsilon'_r \tag{1.9}$$

where $\varepsilon_r$ and $\varepsilon_r'$ are the relative permittivity and relative loss factor of the tissue respectively [Kra.92].

Although several studies have been conducted to measure the dielectric properties of healthy biological tissues, a rather inadequate number of studies of the dielectric properties of healthy and/or cancerous breast tissues at microwave frequencies has been performed. In 1984, Chaudhary *et al.* measured the relative permittivity ($\varepsilon_r$) and the conductivity ($\sigma$) of removed normal and malignant breast tissue samples obtained from 15 patients for frequency range from 3 MHz to 3 GHz [Cha.84]. The data obtained by Chaudhary *et al.* shows that the dielectric contrast between malignant and normal breast tissues has a ratio of around 5:1. In 1988, the dielectric properties of breast carcinoma and elected contiguous non-malignant tissues in the 20 kHz-100 MHz range were measured by Surowiec *et al.* [Sur.88]. In 1992, another contribution by

Campbell *et al.* was added where the dielectric properties of breast tissues at 3.2 GHz were measured utilizing a resonant cavity method [Cam.92]. Nevertheless, their measurements are not in accord with the data obtained in [Cha.84] [Sur.88]. Also in 1994, the relative permittivity ($\varepsilon_r$) and the conductivity ($\sigma$) of recently extracted tissues from the breast and other body organs from 50 MHz to 900 MHz were measured by Joines *et al.* [Joi.94]. The breast tissue sample was taken from 4 to 7 patients and each sample was measured from three different locations. The data obtained indicate that the ratio of the conductivity ($\sigma$) between malignant and normal breast tissues is 6.4:1, the ratio of the relative permittivity ($\varepsilon_r$) between malignant and normal breast tissues is 3.8:1.

Figure 1-9 summarizes the dielectric properties data for normal and malignant breast tissue by [Cha.84] [Sur.88] [Joi.94] compared with the Debye model given in [Fos.89].

In 1996, Gabriel *et al.* published the most wide-ranging data that involves the dielectric properties measurements of a large collection of healthy tissues over a broad range of frequencies from 10 Hz to 20 GHz [Gab.96a] [Gab.96b] [Gab.96c]. The studies show that the relative permittivity ($\varepsilon_r$) and the conductivity ($\sigma$) of high-water-content tissues (like the muscle or the malignant tumours) are around an order of magnitude greater than low-water-content tissues (like fat or normal breast tissue). In addition, their studies illustrate that the contrast perseveres over the whole radio-frequency (RF) range. All the aforementioned studies and measurements have consistently revealed that the complex dielectric parameters of cancerous breast tissue are much greater than that of the noncancerous breast tissue and that there is a large contrast in the electrical properties between normal breast tissues and malignant tumours. However not all the published data of the dielectric properties of breast tissue agree. There are some slight variations in the measured dielectric and electric properties, and the reason behind this is the physiological structure of the breast such as

the heterogeneity of the breast tissue, the blood volume content, the fat volume matter and the physical dimensions of the breast tissue. Also the menopausal stage of the patient has a great impact on the discrepancies of the dielectric properties of the breast.

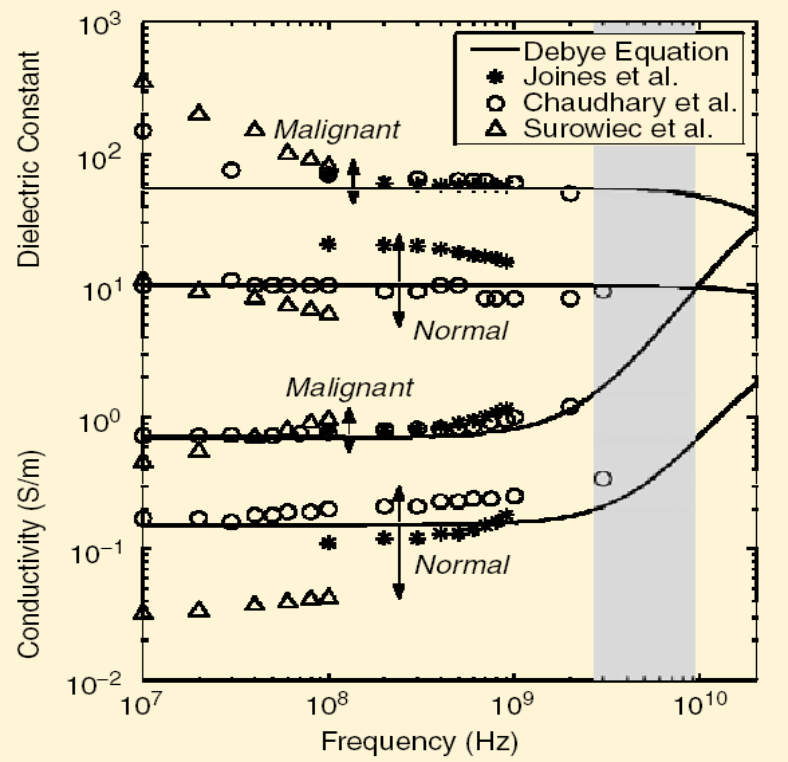


Figure 1-9: Single-pole Debye curve fits of measured baseline dielectric-properties data for normal and malignant breast tissue at radio and microwave frequencies [Li.01].

The selection of complex permittivity values is not a precise process at present because of the uncertainty that exists in the literature on the dielectric properties of normal breast tissue at microwave frequencies [Hur.87]. Three dielectric measurement investigations indicate that the normal breast tissue is a low-dielectric-constant, low-loss material and that the within-patient changeability in dielectric properties is less than 10% around the nominal values [Cha.84] [Joi.94] [Sur.88]. However, the nominal values across these three studies are not in agreement. Other investigations suggest that the influence of normal breast tissue heterogeneity on dielectric-property changeability is more considerable, because the dielectric properties of fat and fibroglandular tissue are manifestly different [Cam.92] [Mea.00] [Bea.03]. Tissue heterogeneity in the breast may justify the discrepancies noticed by the different studies of [Cha.84] [Sur.88] [Joi.94].

This thesis focuses on detecting malignant tumours, particularly those with no microcalcifications (a small build-up of calcium in the breast). A cluster of these very small specks of calcium may imply that cancer is present. Some benign tumours (an abnormal growth that is stable, treatable, and generally not life-threatening) may also have high-water content and could cause reflection response similar to that produced by malignant tumours. However, currently, there exists little trustworthy data regarding the dielectric properties of benign tumours. Studying and investigating the electrical and physiological properties of benign tumours is a broad subject by itself that will aid in developing optimised microwave breast imaging system and can be considered in future research endeavours by others. Here, the focus is only on the dielectric properties of malignant tumours.

Concisely, the published data in the literature shows that there is a large contrast and difference between the normal and cancerous breast tissue at microwave frequencies. The breast model used in this investigation consists of breast tissue with the muscle surrounded by an outer layer of skin. The breast tissue consists of fat, glands and blood. This model is used for feasibility studies of tumour detection in two-dimensional cross sections, for theoretical image formation and for experimental investigation. A skin of 2 mm thickness is assumed with a relative permittivity ($\varepsilon_r$) of 36 and conductivity ($\sigma$) of 4 S/m from 1 to 10 GHz. Breast tissue of 60 mm thickness is used with a relative permittivity ($\varepsilon_r$) of 9 and conductivity ($\sigma$) of 0.4 S/m. A tumour is taken to have a relative permittivity ($\varepsilon_r$) of 50 and conductivity ($\sigma$) of 4 S/m. The model consists of breast tissue surrounded by an outer layer of skin as illustrated in Figure 1-10. Thus the model is composed of the following: layer 1: skin; $\varepsilon_{r1} = 36$ and $\sigma_1 = 4$ S/m, thickness = 2 mm. Layer 2: breast tissue; $\varepsilon_{r2} = 9$ and $\sigma_2 = 0.4$ S/m, thickness = 60 mm. Layer 3: skin; $\varepsilon_{r3} = 36$ and $\sigma_3 = 4$ S/m, thickness = 2 mm. A tumour ($\varepsilon_{ri} = 50$ and $\sigma_i = 4$ S/m) with dimensions of 6 mm x 6 mm x 3 mm is introduced within the breast tissue.

This model with the values mentioned is adopted through out the simulation analysis of chapter 3 of this thesis [Fea.00] [Sal.03b] [Sal.04] [Sal.05] [Sal.06]. 50% of all breast tumours occur 25 mm deep [Par.59]. Nevertheless, tumour depth will be altered through out the simulation analysis to consider the other 50% of breast tumours whether they are deeper or closer to the skin and to analyse the effect of tumour location on the results. Breast tissue is soft enough to be squeezed to accommodate for the tumour location if the tumour is far from the sensor.

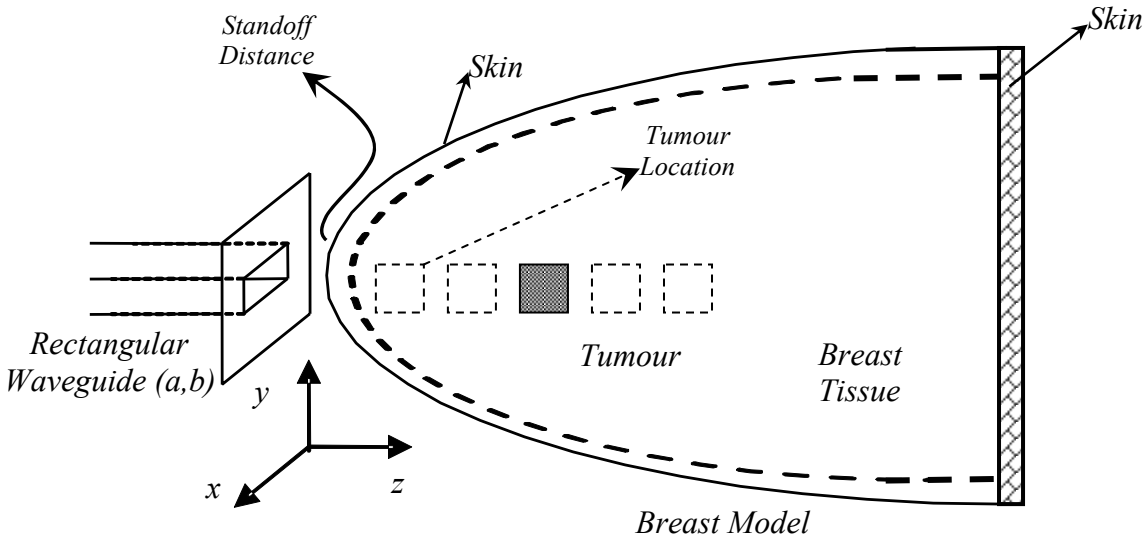


Figure 1-10: Breast model with tumour embedded at different depths in front of the microwave sensor.

## *1.14 Methodology*

Over the past years, extensive research adopting microwave imaging was conducted for the purpose of breast cancer detection [Bea.03] [Che.98] [Fea.00] [Fea.02] [Fra.98] [Hag.98] [Hag.99] [Kru.99a] [Kru.99b] [Li.01] [Li.03] [Miy.93] [Mou.00] [Wan.99]. The high contrast in the dielectric properties between normal and malignant breast tissues is the appealing factor for tumour detection with microwave

imaging and non-invasive testing techniques. The interaction of electromagnetic waves, at microwave frequencies, with multilayered dielectric media is fundamental for any microwave screening or testing application. Also, detection of tumours in their early stages is a very important step in order for the patient to be treated without any surgical operation or medical action that would negatively affect the patient's life. However, an effective detection process can not be achieved without full understanding of the interaction between the microwaves and the breast structure in the near-field region. That is why it is of great importance to understand the interaction of the electric and magnetic fields radiated from the microwave sensor, in this case an open-ended rectangular waveguide sensor, with the breast under inspection. Thus, chapter 2 is assigned to develop a mathematical model of the interaction between electromagnetic waves, at microwave frequencies, with N-layer dielectric media. In chapter 3, an extensive theoretical simulation analysis is conducted to reveal the applicability of near-field microwave NIT&E technique for breast cancer detection. In chapter 4, a breast phantom that closely mimics the dielectric properties contrast ratio of the real breast is obtained. This phantom is utilized for experimental investigation and preclinical examination. Chapter 5 is devoted to test to a greater extent the reliability of the theoretical formulations presented in chapter 3. An experimental system for calibrated measurements is presented and its operation is clarified. A detailed and in-depth analysis and comparison between calibrated measurements and simulation results is studied and illustrated. Chapter 6 concludes the work and outlines the future trends and outlook for breast cancer detection using near-field non-invasive non-ionising microwave testing techniques.

# *CHAPTER 2*

# *Theoretical Modelling of Open-Ended Rectangular Waveguide Probes Radiating into Multilayered Structures*

## *2.1 Field Properties in the Near-Field Region of Open-Ended Rectangular Waveguide Probes*

Modelling the interaction between electromagnetic waves and a multilayer dielectric structure at microwave frequencies is fundamental for a wide range of applications. The mathematical derivations of this chapter were originated by Dr. Nasser Qaddoumi as part of his Ph.D. thesis and a model that describes the interaction of a rectangular waveguide with an infinite half-space of a material (i.e. single layer) was developed [Qad.98a]. The limitation of Dr. Qaddoumi's work is that the model was developed for an infinite half-space of one layer material. The work is expanded here and a general model that describes the near-field radiation properties of the open-ended rectangular waveguide radiating into a multilayered dielectric structure is developed in this chapter. First, the electric field coefficients in each layer should be expressed in terms of the media constitutive parameters for any stratified dielectric media terminated with a dielectric infinite half-space or a conducting sheet. Then, the Fourier transform matching (FTM) technique will be utilized to express the electric field coefficients in a recursive model to obtain the electric and magnetic field coefficients. Once the field coefficients are obtained, the electric field and the power

spatial distributions in the irradiated media will be calculated [Abu.03] [Sal.04a] [Sal.04b] [Sal.04c] [Sal.05] [Sal.06] [Sal.07].

The problem setup is represented in Figure 2-1. A general stratified structure of any number of dielectric layers (N) will be considered. The $n^{th}$ layer has complex relative dielectric constant $\varepsilon_{rn}$ and thickness $d_n$. This structure may be backed by an infinite half-space of material or a conducting sheet. The formulation is general and accounts for the dominant mode. Thus, a waveguide with dominant mode excitation ($TE_{10}$) is used to illuminate the structure with electromagnetic waves at microwave frequencies. The waveguide aperture lies in the xy-plane and is centred at the origin. Since the region of interest for the solution lies in the region z>0, Huygens' sources over the aperture can be introduced. This could be accomplished precisely if it is guaranteed that no radiation will be in the region z<0 [Kra.88] [Bal.97]. To do so, the analysis assumes that the waveguide aperture is mounted on an infinite conducting flange. The dielectric structure is placed in the near-field region of the open-ended rectangular waveguide. The intention is to find the electric field's coefficients in each layer.

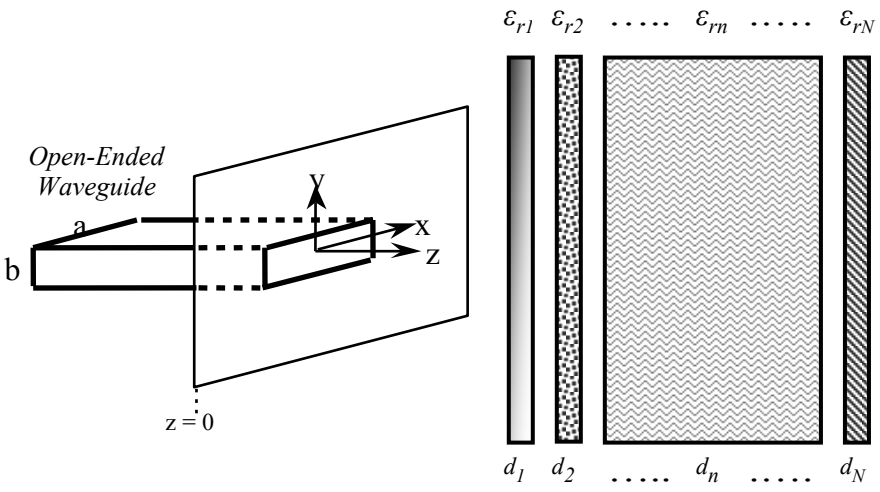


Figure 2-1: The cross-section of an open-ended rectangular waveguide probe radiating into an N-layer dielectric structure.

For the dominant $TE_{10}$ mode, the excitation aperture fields are given by:

$$\overline{E}_{ap}(x,y) = \hat{y}(1+\Gamma)\frac{j\pi\omega\mu}{ak_{c10}^2}\sin(\frac{\pi}{a}x) \tag{2.1}$$

$$\overline{H}_{ap}(x,y) = \hat{x}(1-\Gamma)\frac{j\pi\omega\mu}{ak_{c10}^2}Y_o\sin(\frac{\pi}{a}x) \tag{2.2}$$

Where

$k_{c10} = \frac{\pi}{a}$, and $a$ is the broad dimension of the waveguide

$Y_o = \frac{\sqrt{K^2 - k_{c10}^2}}{\omega\mu}$, is the admittance of the dominant mode, $\hat{x}$ and $\hat{y}$ are unit vectors in the x and y directions of the aperture electric and magnetic fields respectively, $k^2 = \omega^2\mu_c\varepsilon_c$ ($K$ is the propagation constant), $\omega=2\pi f$, and $f$ is the frequency of operation, $\mu_c$ and $\varepsilon_c$ are the complex permeability and complex permittivity of the media respectively. $\Gamma$, is the effective reflection coefficient [Abu.03] [Sal.04b] [Sal.04c] [Poz.05].

To model the interaction between the layered dielectric structure and the electric field, the electric field distribution at every Cartesian coordinate point (x, y, z) must be calculated. This requires finding the field coefficients in each layer of the structure. Starting with Maxwell's equations, the field solution can be obtained by applying the Fourier transform matching technique. This involves expanding the field in each layer in terms of Fourier Integrals and applying boundary conditions at each interface. The boundary conditions simply states that the total tangential electric and magnetic fields must be continuous at each dielectric-dielectric interface and the total tangential electric field must be zero on the surface of the perfect conductor [Sad.95]. Having the solution for the field in the first layer, the reflection coefficient is calculated from the effective admittance at the open-ended rectangular waveguide's aperture. First an infinite half-space of material placed in front of the waveguide is considered. Next, the solution for multilayer structures will be developed.

In a source free region Maxwell's equations for sinusoidal excitation ($e^{-j\omega t}$) can be written as:

$$\overline{\nabla} \times \overline{E}(x,y,z) = -j\omega\mu\overline{H}(x,y,z) \tag{2.3}$$

$$\overline{\nabla} \times \overline{H}(x,y,z) = j\omega\varepsilon\overline{E}(x,y,z) \tag{2.4}$$

$$\overline{\nabla} \bullet \overline{E}(x,y,z) = 0 \tag{2.5}$$

$$\overline{\nabla} \bullet \overline{H}(x,y,z) = 0 \tag{2.6}$$

where $\overline{E}$ is the electric field phasor, $\overline{H}$ is the magnetic field phasor, $\omega$ is the excitation frequency, $\mu_c$ and $\varepsilon_c$ are the complex permeability and complex permittivity of the medium, respectively.

Taking the curl of equation (2.3):

$$\overline{\nabla} \times \overline{\nabla} \times \overline{E}(x,y,z) = -j\omega\mu\overline{\nabla} \times \overline{H}(x,y,z) = \overline{\nabla}\left(\overline{\nabla} \bullet \overline{E}(x,y,z)\right) - \nabla^2 \overline{E}(x,y,z)$$

Substitution of equations (2.4) and (2.5) in the previous equation yields the wave equation in the source-free region.

$$\nabla^2 \overline{E}(x,y,z) + K^2 \overline{E}(x,y,z) = 0 \tag{2.7}$$

Where $K^2 = K_o^2 \varepsilon\mu$ and $K_o = \omega\sqrt{\mu_o \varepsilon_o}$. The electric field can be written using the Fourier integrals in the xy-plane as

$$\overline{E}(x,y,z) = \int_{-\infty}^{\infty}\int_{-\infty}^{\infty} \overline{E}(k_x,k_y,z) e^{j(k_x x + k_y y)} dk_x dk_y \tag{2.8}$$

By substituting equation (2.8) into equation (2.7), the following equation is obtained

$$\left[-k_x^2 - k_y^2 + \frac{d^2}{dz^2} + K^2\right]\overline{E}(k_x,k_y,z) = 0$$

Which can be written as

$$\frac{d^2\overline{E}\left(k_x,k_y,z\right)}{dz^2} - \gamma^2 \overline{E}\left(k_x,k_y,z\right) = 0 \tag{2.9}$$

Where, $\gamma = \sqrt{k_x^2 + k_y^2 - K^2}$

Equation (2.9) has a solution in the form of

$$\overline{E}\left(k_x, k_y, z\right) = \overline{A}e^{-\gamma z} + \overline{B}e^{\gamma z} \tag{2.10}$$

Where, $\overline{A} = \hat{x}A_x + \hat{y}A_y + \hat{z}A_z$ and $\overline{B} = \hat{x}B_x + \hat{y}B_y + \hat{z}B_z$ are unknown vector coefficients to be determined. Using these unknown vector coefficients, the electric field can be written as

$$\overline{E}(x, y, z) = \int_{-\infty}^{\infty}\int_{-\infty}^{\infty}[\hat{x}(A_x e^{-\gamma z} + B_x e^{\gamma z}) + \hat{y}(A_y e^{-\gamma z} + B_y e^{\gamma z}) + \hat{z}(A_z e^{-\gamma z} + B_z e^{\gamma z})]e^{j(k_x x + k_y y)}dk_x dk_y \tag{2.11}$$

Applying equation (2.5) to equation (2.11), the following equations are obtained:

$$(jk_x A_x + jk_y A_y - \gamma A_z)e^{-\gamma z} = 0$$
$$(jk_x B_x + jk_y B_y + \gamma B_z)e^{\gamma z} = 0$$

Solve for $A_z$ and $B_z$:

$$A_z = \frac{jk_x A_x + jk_y A_y}{\gamma}$$
$$B_z = -\frac{jk_x B_x + jk_y B_y}{\gamma}$$

Using the above equations, equation (2.11) is written as

$$\overline{E}(x, y, z) = \int_{-\infty}^{\infty}\int_{-\infty}^{\infty}\overline{F}(k_x, k_y, z)e^{j(k_x x + k_y y)}dk_x dk_y \tag{2.12}$$

Where

$$\overline{F}(k_x, k_y, z) = \left[A_x(\hat{x} + \hat{z}\frac{jk_x}{\gamma}) + A_y(\hat{y} + \hat{z}\frac{jk_y}{\gamma})\right]e^{-\gamma z}$$
$$+\left[B_x(\hat{x} - \hat{z}\frac{jk_x}{\gamma}) + B_y(\hat{y} - \hat{z}\frac{jk_y}{\gamma})\right]e^{\gamma z} \tag{2.13}$$

Using equation (2.3), the $\overline{H}$ -field is given as:

$$\overline{H}(x,y,z)=\frac{j}{\varpi\mu}\int_{-\infty}^{\infty}\int_{-\infty}^{\infty}[(\overline{c}_1A_x+\overline{c}_2A_y)e^{-\gamma z}+(\overline{c}_3B_x+\overline{c}_4B_y)e^{\gamma z}]e^{j(k_xx+k_yy)}dk_xdk_y \tag{2.14}$$

Where,

$$\overline{c}_1=-\hat{x}\frac{k_xk_y}{\gamma}+\hat{y}\frac{K^2-k_y^2}{\gamma}-\hat{z}(jk_y) \tag{2.15.1}$$

$$\overline{c}_2=-\hat{x}\frac{K^2-k_x^2}{\gamma}+\hat{y}\frac{k_xk_y}{\gamma}+\hat{z}(jk_x) \tag{2.15.2}$$

$$\overline{c}_3=\hat{x}\frac{k_xk_y}{\gamma}-\hat{y}\frac{K^2-k_y^2}{\gamma}-\hat{z}(jk_y) \tag{2.15.3}$$

$$\overline{c}_4=\hat{x}\frac{K^2-k_x^2}{\gamma}-\hat{y}\frac{k_xk_y}{\gamma}+\hat{z}(jk_x) \tag{2.15.4}$$

Now, if there are N-layers, we assume $\mu_n=\mu_0 \quad \forall n$ for paramagnetic and diamagnetic materials.

From equation (2.1), it is noticed that the excitation field has the y-component only. In other words, it is y-directed only. So,

$A_{xn}=0 \quad \forall n$
$B_{xn}=0 \quad \forall n$

Then, equation (2.13) has z and y components in $n^{th}$ layer. Thus, let:

$$F_{yn}(k_x,k_y,z)=A_{yn}e^{-\gamma_n z}+B_{yn}e^{\gamma_n z} \tag{2.15.5}$$

$$F_{zn}(k_x,k_y,z)=\frac{jk_yA_{yn}}{\gamma_n}e^{-\gamma_n z}-\frac{jk_yB_{yn}}{\gamma_n}e^{\gamma_n z} \tag{2.15.6}$$

The y-component of the $\overline{E}$ -field in the $n^{th}$ layer is

$$E_{yn}(x,y,z)=\int_{-\infty}^{\infty}\int_{-\infty}^{\infty}F_{yn}(k_x,k_y,z)e^{j(k_xx+k_yy)}dk_xdk_y \tag{2.16}$$

The z-component of the E-field in the $n^{th}$ layer is

$$E_{zn}(x,y,z)=\int_{-\infty}^{\infty}\int_{-\infty}^{\infty}F_{zn}(k_x,k_y,z)e^{j(k_xx+k_yy)}dk_xdk_y \tag{2.17}$$

Also, the $\overline{H}$ -field in each layer is found from equation (2.14)

$$\overline{H}_n(x,y,z) = \frac{j}{\omega\mu_n}\int_{-\infty}^{\infty}\int_{-\infty}^{\infty}(\overline{c}_{2n}A_{yn}e^{-\gamma_n z} + \overline{c}_{4n}B_{yn}e^{\gamma_n z})e^{j(k_x x+k_y y)}dk_x dk_y \tag{2.18}$$

By enforcing the appropriate boundary conditions at the boundaries between the layers, the field coefficients $A_{yn}$ and $B_{yn}$ $\forall n$ are determined.

The above equations will be exploited to find the electric field and power pattern in an N-Layer dielectric structure. But initially, the electric field and power pattern will be calculated for three layers. Then, the electric field and power pattern in N-Layer dielectric structure will be analyzed and determined. Here, four different cases will be considered, namely:

1. 3-Layers dielectric structure terminated by an infinite half-space (IHS).
2. 3-Layers dielectric structure terminated by a conductor sheet (CS).
3. 3-Layers dielectric structure terminated by an infinite half-space (IHS) with a uniform inclusion (tumour) in the second layer.
4. 3-Layers dielectric structure terminated by a conductor sheet (CS) with a uniform inclusion (tumour) in the second layer.

The consistency and uniformity in the solutions of the above four types will lead us to generalize the results for N-layer dielectric structures.

For all types, the electric and magnetic fields in each layer, and consequently, the power can be determined from equations (2.16), (2.17) and (2.18) after obtaining the field coefficients. In the following sections, the field coefficients for all cases mentioned earlier will be presented.

### *2.1.1 Field Properties for a 3-Layer Dielectric Structure Terminated by Infinite Half-Space (IHS) in the Near-Field Region*

The 3-layer structure is represented using its physical and dielectric properties as follows:

Layer 1: thickness $d_1$ and permittivity $\varepsilon_{r1}$.

Layer 2: thickness $d_2$ and permittivity $\varepsilon_{r2}$ .

Layer 3: Infinite Half-Space (IHS) and permittivity $\varepsilon_{r3}$.

Since layer 3 is an infinite half-space, the radiation condition is:

$\overline{E}_3(x,y,z)_{z\to\infty} = 0$. This requires $B_{y3} = 0$.

Now, applying the two boundary conditions; $E_y$ and $H_x$ are continuous at each interface.

At $z = d_2$, the Fourier transform (FT) of $E_{y3}$ and $H_{x3}$ must equal the Fourier transform (FT) of $E_{y2}$ and $H_{x2}$. This will yield the following two equations:

$$A_{y2}e^{-\gamma_2 d_2} + B_{y2}e^{\gamma_2 d_2} = A_{y3}e^{-\gamma_3 d_2} \tag{2.19}$$

$$-C_2 A_{y2}e^{-\gamma_2 d_2} + C_2 B_{y2}e^{\gamma_2 d_2} = -C_3 A_{y3}e^{-\gamma_3 d_2} \tag{2.20}$$

Where $C_2$ and $C_3$ are the x components of $\overline{c}_2$ presented in equation (2.15.2) and $\overline{c}_4$ presented in equation (2.15.4) based on equation (2.18).

At $z = d_1$, the Fourier transform (FT) of $E_{y2}$ and $H_{x2}$ must equal the Fourier transform (FT) of $E_{y1}$ and $H_{x1}$. This will yield another two equations:

$$A_{y1}e^{-\gamma_1 d_1} + B_{y1}e^{\gamma_1 d_1} = A_{y2}e^{-\gamma_2 d_1} + B_{y2}e^{\gamma_2 d_1} \tag{2.21}$$

$$-C_1 A_{y1}e^{-\gamma_1 d_1} + C_1 B_{y1}e^{\gamma_1 d_1} = -C_2 A_{y2}e^{-\gamma_2 d_1} + C_2 B_{y2}e^{\gamma_2 d_1} \tag{2.22}$$

At $z = 0$, The Fourier transform (FT) of $E_{y1}$ must equal the Fourier transform (FT) of the aperture field distribution, *I*. That's to say:

$$A_{y1} + B_{y1} = I \tag{2.23}$$

Where

$$I = \int_0^b \int_0^a E_{ap}(x,y) e^{-j(k_x x + k_y y)} dxdy = (1+\Gamma)\frac{j\pi\omega\mu}{ak_{c10}^2} \int_0^b \int_0^a \sin(\frac{\pi}{a}x) e^{-j(k_x x + k_y y)} dxdy$$

$$= Q\left[\frac{\frac{\pi}{a}}{(\frac{\pi}{a}) - k_x^2}[e^{-jk_x a} + 1]\right]\frac{e^{-jk_y b} - 1}{-jk_y}$$

$$Q = (1+\Gamma)\frac{j\omega\mu_o}{(2\pi)^2 a k_{c10}^2}$$

Solving the above five equations (from 2.19 to 2.23) for five unknowns will result in the following:

$$A_{y1} = \frac{I}{1+g_1} \tag{2.24a}$$

$$B_{y1} = \frac{g_1 I}{1+g_1} \tag{2.24b}$$

$$A_{y2} = \frac{G_1 I}{1+g_1} e^{-\gamma_1 d_1} e^{\gamma_2 d_1} \tag{2.25a}$$

$$B_{y2} = \frac{g_2 G_1 I}{1+g_1} e^{-\gamma_1 d_1} e^{\gamma_2 d_1} \tag{2.25b}$$

$$A_{y3} = \frac{G_1 I}{1+g_1}\left(1 + g_2 e^{2\gamma_2 d_2}\right) e^{-\gamma_1 d_1} e^{\gamma_2 d_1} e^{-\gamma_2 d_2} e^{\gamma_3 d_2} \tag{2.26}$$

Where

$$K_0^2 = \omega^2 \varepsilon_o \mu_o, K_n^2 = K_0^2 \varepsilon_{rn}$$
$$\gamma_n = \sqrt{k_x^2 + k_y^2 - K_n^2}$$

$$C_n = \frac{K_n^2 - k_x^2}{\gamma_n}$$

$$g_2 = \frac{C_2 - C_3}{C_2 + C_3} e^{-2\gamma_2 d_2},\ M_1 = \frac{1 - g_2 e^{2\gamma_2 d_1}}{1 + g_2 e^{2\gamma_2 d_1}}$$

$$g_1 = \frac{C_1 - C_2 M_1}{C_1 + C_2 M_1} e^{-2\gamma_1 d_1},\ G_1 = \frac{1 + g_1 e^{2\gamma_1 d_1}}{1 + g_2 e^{2\gamma_2 d_1}}$$

*a* and *b* are the broad and narrow dimensions of the open-ended rectangular waveguide aperture respectively.

### *2.1.2 Field Properties for a 3-Layer Dielectric Structure Terminated by a Conducting Sheet (CS) in the Near-Field Region*

The 3-layer structure is represented using its physical and dielectric properties as follows:

Layer 1: thickness $d_1$, permittivity $\varepsilon_{r1}$.

Layer 2: thickness $d_2$, permittivity $\varepsilon_{r2}$.

Layer 3: thickness $d_3$, permittivity $\varepsilon_{r3}$.

At the conductor interface ( $z = d_3$ ), the tangential electric field must vanish.

$\overline{E}_3(x, y, z)_{z=d_3} = 0$. This requires:

$$A_{y3} e^{-\gamma_3 d_3} + B_{y3} e^{\gamma_3 d_3} = 0 \tag{2.27}$$

Now, applying the boundary conditions, $E_y$ and $H_x$ are continuous at each interface.

At $z = d_2$, the Fourier transform (FT) of $E_{y3}$ and $H_{x3}$ must equal the Fourier transform (FT) of $E_{y2}$ and $H_{x2}$. This will yield the following two equations:

$$A_{y2} e^{-\gamma_2 d_2} + B_{y2} e^{\gamma_2 d_2} = A_{y3} e^{-\gamma_3 d_2} + B_{y3} e^{\gamma_3 d_2} \tag{2.28}$$

$$-C_2 A_{y2} e^{-\gamma_2 d_2} + C_2 B_{y2} e^{\gamma_2 d_2} = -C_3 A_{y3} e^{-\gamma_3 d_2} + C_3 B_{y3} e^{\gamma_3 d_2} \text{ 、} \tag{2.29}$$

At $z = d_1$, the Fourier transform (FT) of $E_{y2}$ and $H_{x2}$ must equal the Fourier transform (FT) of $E_{y1}$ and $H_{x1}$. This will result into another two equations:

$$A_{y1}e^{-\gamma_1 d_1} + B_{y1}e^{\gamma_1 d_1} = A_{y2}e^{-\gamma_2 d_1} + B_{y2}e^{\gamma_2 d_1} \tag{2.30}$$

$$-C_1 A_{y1}e^{-\gamma_1 d_1} + C_1 B_{y1}e^{\gamma_1 d_1} = -C_2 A_{y2}e^{-\gamma_2 d_1} + C_2 B_{y2}e^{\gamma_2 d_1} \tag{2.31}$$

At $z = 0$, The Fourier transform (FT) of $E_{y1}$ must equal the Fourier transform (FT) of the aperture field:

$$A_{y1} + B_{y1} = I \tag{2.32}$$

The solution of the above equations results in the following:

$$A_{y1} = \frac{I}{1+g_1} \tag{2.33a}$$

$$\mathrm{B}_{y1} = \frac{g_1 I}{1+g_1} \tag{2.33b}$$

$$A_{y2} = \frac{G_1 I}{1+g_1} e^{-\gamma_1 d_1} e^{\gamma_2 d_1} \tag{2.34a}$$

$$B_{y2} = \frac{g_2 G_1 I}{1+g_1} e^{-\gamma_1 d_1} e^{\gamma_2 d_1} \tag{2.34b}$$

$$A_{y3} = \frac{G_2 G_1 I}{1+g_1} e^{-\gamma_1 d_1} e^{\gamma_2 d_1} e^{-\gamma_2 d_2} e^{\gamma_3 d_2} \tag{2.35a}$$

$$B_{y3} = \frac{g_3 G_2 G_1 I}{1+g_1} e^{-\gamma_1 d_1} e^{\gamma_2 d_1} e^{-\gamma_2 d_2} e^{\gamma_3 d_2} \tag{2.35b}$$

Where

$$g_3 = -e^{-2\gamma_3 d_3} \quad , \; M_2 = \frac{1 - g_3 e^{2\gamma_3 d_2}}{1 + g_3 e^{2\gamma_3 d_2}}$$

$$g_2 = \frac{C_2 - C_3 M_2}{C_2 + C_3 M_2} e^{-2\gamma_2 d_2} \; , \; M_1 = \frac{1 - g_2 e^{2\gamma_2 d_1}}{1 + g_2 e^{2\gamma_2 d_1}}$$

$$g_1 = \frac{C_1 - C_2 M_1}{C_1 + C_2 M_1} e^{-2\gamma_1 d_1} \; , \; G_1 = \frac{1 + g_1 e^{2\gamma_1 d_1}}{1 + g_2 e^{2\gamma_2 d_1}}$$

$$G_2 = \frac{1 + g_2 e^{2\gamma_2 d_2}}{1 + g_3 e^{2\gamma_3 d_2}}$$

Note that if $g_3 = 0$, the same results as in section 2.1.1 of the infinite half-space (IHS) termination are obtained.

### *2.1.3 Field Properties for a 3-Layer Dielectric Structure Terminated by Infinite Half-Space (IHS) with an Inclusion (Tumour) in the Near-Field Region*

The inclusion in the second layer can be modelled by defining the permittivity distribution in that layer as a function of x and y. The structure is described as following:

Layer 1: thickness $d_1$, permittivity $\varepsilon_{r1}$.

Layer 2: thickness $d_2$, permittivity $\varepsilon_{r2}(x,y) = \begin{cases} \varepsilon_{r21} & : x \in [x_1, x_2], y \in [y_1, y_2] (inclusion) \\ \varepsilon_{r22} & : otherwise \end{cases}$.

Layer 3: Infinite-half space (IHS), permittivity $\varepsilon_{r3}$.

The key point in the solution is to obtain a measurable parameter that reflects the structure properties (i.e. reflection coefficient). From a practical point of view, the internal reflections in the x and y directions (in the second layer) can not be measured. This is because the measurement setup assumes that the waveguide's aperture lies in the xy-plane.

The same approach as in section 2.1.1 is adopted to solve for the field coefficients. Matching the Fourier Transforms of the tangential fields at the three interfaces results in the following equations:

$$A_{y3}e^{-\gamma_3 d_2} = \begin{Bmatrix} A_{y21}e^{-\gamma_{21}d_2} + B_{y21}e^{\gamma_{21}d_2} & : x \in [x_1, x_2], y \in [y_1, y_2] \\ A_{y22}e^{-\gamma_{22}d_2} + B_{y22}e^{\gamma_{22}d_2} & : otherwise \end{Bmatrix} \tag{2.36}$$

$$-C_3 A_{y3}e^{-\gamma_3 d_2} = \begin{Bmatrix} -C_{21}A_{y21}e^{-\gamma_{21}d_2} + C_{21}B_{y21}e^{\gamma_{21}d_2} & : x \in [x_1, x_2], y \in [y_1, y_2] \\ -C_{22}A_{y22}e^{-\gamma_{22}d_2} + C_{22}B_{y22}e^{\gamma_{22}d_2} & : otherwise \end{Bmatrix} \tag{2.37}$$

$$A_{y1}e^{-\gamma_1 d_1} + B_{y1}e^{y_1 d_1} = \begin{Bmatrix} A_{y21}e^{-\gamma_{21}d_1} + B_{y21}e^{\gamma_{21}d_1} & : x \in [x_1, x_2], y \in [y_1, y_2] \\ A_{y22}e^{-\gamma_{22}d_1} + B_{y22}e^{\gamma_{22}d_1} & : otherwise \end{Bmatrix} \tag{2.38}$$

$$-C_1 A_{y1}e^{-\gamma_1 d_1} + C_1 B_{y1}e^{y_1 d_1} = \begin{Bmatrix} -C_{21}A_{y21}e^{-\gamma_{21}d_1} + C_{21}B_{y21}e^{\gamma_{21}d_1} & : x \in [x_1, x_2], y \in [y_1, y_2] \\ -C_{22}A_{y22}e^{-\gamma_{22}d_1} + C_{22}B_{y22}e^{\gamma_{22}d_1} & : otherwise \end{Bmatrix} \tag{2.39}$$

$$A_{y1} + B_{y1} = I \tag{2.40}$$

The subscript ($m$) of the propagation constant ($\gamma_{2m}$) and ($C_{2m}$) represents the inclusion (tumour) $m$ = 1 and the host (rest of the tissue in that layer) $m$ =2.

Solving the above equations yields into the following field coefficients:

$$A_{y1} = \begin{Bmatrix} \dfrac{I}{1+g_{11}} & : x \in [x_1, x_2], y \in [y_1, y_2] \\ \dfrac{I}{1+g_{12}} & : otherwise \end{Bmatrix} \tag{2.41a}$$

$$B_{y1} = \begin{Bmatrix} \dfrac{g_{11}I}{1+g_{11}} & : x \in [x_1, x_2], y \in [y_1, y_2] \\ \dfrac{g_{12}I}{1+g_{12}} & : otherwise \end{Bmatrix} \tag{2.41b}$$

$$A_{y2} = \begin{Bmatrix} \dfrac{G_{11}I}{1+g_{11}} e^{-\gamma_1 d_1} e^{\gamma_{21} d1} & : x \in [x_1, x_2], y \in [y_1, y_2] \\ \dfrac{G_{12}I}{1+g_{12}} e^{-\gamma_1 d_1} e^{\gamma_{22} d1} & : otherwise \end{Bmatrix} \tag{2.42a}$$

$$B_{y2} = \begin{cases} \dfrac{g_{21} G_{11} I}{1+g_{11}} e^{-\gamma_1 d_1} e^{\gamma_{21} d_1} & : x \in [x_1, x_2], y \in [y_1, y_2] \\ \dfrac{g_{22} G_{12} I}{1+g_{12}} e^{-\gamma_1 d_1} e^{\gamma_{22} d_1} & : otherwise \end{cases} \tag{2.42b}$$

$$A_{y3} = \begin{cases} \dfrac{G_{11} I}{1+g_{11}} (1 + g_{21} e^{2\gamma_{21} d_2}) e^{-\gamma_1 d_1} e^{\gamma_{21} d_1} e^{-\gamma_{21} d_2} e^{\gamma_3 d_2} & : x \in [x_1, x_2], y \in [y_1, y_2] \\ \dfrac{G_{12} I}{1+g_{12}} (1 + g_{22} e^{2\gamma_{22} d_2}) e^{-\gamma_1 d_1} e^{\gamma_{22} d_1} e^{-\gamma_{22} d_2} e^{\gamma_3 d_2} & : otherwise \end{cases} \tag{2.43}$$

Where

$$g_{21} = \frac{C_{21} - C_3}{C_{21} + C_3} e^{-2\gamma_{21} d_2} \ , \ g_{22} = \frac{C_{22} - C_3}{C_{22} + C_3} e^{-2\gamma_{22} d_2}$$

$$M_{11} = \frac{1 - g_{21} e^{2\gamma_{21} d_1}}{1 + g_{21} e^{2\gamma_{21} d_1}} \ , \ M_{12} = \frac{1 - g_{22} e^{2\gamma_{22} d_1}}{1 + g_{22} e^{2\gamma_{22} d_1}}$$

$$g_{11} = \frac{C_1 - C_{21} M_{11}}{C_1 + C_{21} M_{11}} e^{-2\gamma_1 d_1} \ , \ g_{12} = \frac{C_1 - C_{22} M_{12}}{C_1 + C_{22} M_{12}} e^{-2\gamma_1 d_1}$$

$$G_{11} = \frac{1 + g_{11} e^{2\gamma_1 d_1}}{1 + g_{21} e^{2\gamma_{21} d_1}} \ , \ G_{12} = \frac{1 + g_{12} e^{2\gamma_1 d_1}}{1 + g_{22} e^{2\gamma_{22} d_1}}$$

By setting $C_{21} = C_{22}$, the type of structure (i.e. IHS) considered in section 2.1.1 is obtained.

### *2.1.4 Field Properties for a 3-Layer Dielectric Structure Terminated by a Conducting Sheet (CS) with an Inclusion (Tumour) in the Near-Field Region*

The structure can be described as the following:

Layer 1: thickness $d_1$, permittivity $\varepsilon_{r1}$.

Layer 2: thickness $d_2$, permittivity $\varepsilon_{r2}(x, y) = \begin{cases} \varepsilon_{r21} & : x \in [x_1, x_2], y \in [y_1, y_2] \\ \varepsilon_{r22} & : otherwise \end{cases}$.

Layer 3: thickness $d_3$ , permittivity $\varepsilon_{r3}$.

Using the same approach adopted in section 2.1.2, the following equations are obtained:

$$A_{y3}e^{-\gamma_3 d_3} + B_{y3}e^{\gamma_3 d_3} = 0 \tag{2.44}$$

$$A_{y3}e^{-\gamma_3 d_2} + B_{y3}e^{\gamma_3 d_2} = \begin{Bmatrix} A_{y21}e^{-\gamma_{21} d_2} + B_{y21}e^{\gamma_{21} d_2} & : x \in [x_1, x_2], y \in [y_1, y_2] \\ A_{y22}e^{-\gamma_{22} d_2} + B_{y22}e^{\gamma_{22} d_2} & : otherwise \end{Bmatrix} \tag{2.45}$$

$$-C_3 A_{y3}e^{-\gamma_3 d_2} + C_3 B_{y3}e^{\gamma_3 d_2} = \begin{Bmatrix} -C_{21} A_{y21}e^{-\gamma_{21} d_2} + C_{21} B_{y21}e^{\gamma_{21} d_2} & : x \in [x_1, x_2], y \in [y_1, y_2] \\ -C_{22} A_{y22}e^{-\gamma_{22} d_2} + C_{22} B_{y22}e^{\gamma_{22} d_2} & : otherwise \end{Bmatrix} \tag{2.46}$$

$$A_{y1}e^{-\gamma_1 d_1} + B_{y1}e^{y_1 d_1} = \begin{Bmatrix} A_{y21}e^{-\gamma_{21} d_1} + B_{y21}e^{\gamma_{21} d_1} & : x \in [x_1, x_2], y \in [y_1, y_2] \\ A_{y22}e^{-\gamma_{22} d_1} + B_{y22}e^{\gamma_{22} d_1} & : otherwise \end{Bmatrix} \tag{2.47}$$

$$-C_1 A_{y1}e^{-\gamma_1 d_1} + C_1 B_{y1}e^{y_1 d_1} = \begin{Bmatrix} -C_{21} A_{y21}e^{-\gamma 21 d_1} + C_{21} B_{y21}e^{\gamma 21 d_1} & : x \in [x_1, x_2], y \in [y_1, y_2] \\ -C_{22} A_{y22}e^{-\gamma 22 d_1} + C_{22} B_{y22}e^{\gamma 22 d_1} & : otherwise \end{Bmatrix} \tag{2.48}$$

$$A_{y1} + B_{y1} = I \tag{2.49}$$

The subscript ($m$) of the propagation constant ($\gamma_{2m}$) and ($C_{2m}$) represents the inclusion (tumour) $m$ = 1 and the host (rest of the tissue in that layer) $m$ =2.

Solving the above equations yields the following field coefficients:

$$A_{y1} = \begin{Bmatrix} \dfrac{I}{1+g_{11}} & : x \in [x_1, x_2], y \in [y_1, y_2] \\ \dfrac{I}{1+g_{12}} & : otherwise \end{Bmatrix} \tag{2.50a}$$

$$B_{y1} = \begin{Bmatrix} \dfrac{g_{11} I}{1+g_{11}} & : x \in [x_1, x_2], y \in [y_1, y_2] \\ \dfrac{g_{12} I}{1+g_{12}} & : otherwise \end{Bmatrix} \tag{2.50b}$$

$$A_{y2} = \begin{Bmatrix} \dfrac{G_{11} I}{1+g_{11}} e^{-\gamma_1 d_1} e^{\gamma 21 d1} & : x \in [x_1, x_2], y \in [y_1, y_2] \\ \dfrac{G_{12} I}{1+g_{12}} e^{-\gamma_1 d_1} e^{\gamma 22 d1} & : otherwise \end{Bmatrix} \tag{2.51a}$$

$$B_{y2}=\left\{\begin{array}{ll}\dfrac{g_{21}G_{11}I}{1+g_{11}}e^{-\gamma_1 d_1}e^{\gamma_{21}d1} & :x\in[x_1,x_2],y\in[y_1,y_2]\\ \dfrac{g_{22}G_{12}I}{1+g_{12}}e^{-\gamma_1 d_1}e^{\gamma_{22}d1} & :otherwise\end{array}\right\} \tag{2.51b}$$

$$A_{y3}=\left\{\begin{array}{ll}\dfrac{G_{21}G_{11}I}{1+g_{11}}e^{-\gamma_1 d_1}e^{\gamma_{21}d1}e^{-\gamma_{21}d_2}e^{\gamma_3 d_2} & :x\in[x_1,x_2],y\in[y_1,y_2]\\ \dfrac{G_{22}G_{12}I}{1+g_{12}}e^{-\gamma_1 d_1}e^{\gamma_{22}d1}e^{-\gamma_{22}d_2}e^{\gamma_3 d_2} & :otherwise\end{array}\right\} \tag{2.52a}$$

$$B_{y3}=\left\{\begin{array}{ll}\dfrac{g_3G_{21}G_{11}I}{1+g_{11}}e^{-\gamma_1 d_1}e^{\gamma_{21}d1}e^{-\gamma_{21}d_2}e^{\gamma_3 d_2} & :x\in[x_1,x_2],y\in[y_1,y_2]\\ \dfrac{g_3G_{22}G_{12}I}{1+g_{12}}e^{-\gamma_1 d_1}e^{\gamma_{22}d1}e^{-\gamma_{22}d_2}e^{\gamma_3 d_2} & :otherwise\end{array}\right\} \tag{2.52b}$$

Where

$$g_3=-e^{-2\gamma_3 d_3}\quad,\ M_2=\frac{1-g_3e^{2\gamma_3 d_2}}{1+g_3e^{2\gamma_3 d_2}}$$

$$g_{21}=\frac{C_{21}-C_3M_2}{C_{21}+C_3M_2}e^{-2\gamma_{21}d_2}\ ,\ g_{22}=\frac{C_{22}-C_3M_2}{C_{22}+C_3M_2}e^{-2\gamma_{22}d_2}$$

$$M_{11}=\frac{1-g_{21}e^{2\gamma_{21}d_1}}{1+g_{21}e^{2\gamma_{21}d_1}}\ ,\ M_{12}=\frac{1-g_{22}e^{2\gamma_{22}d_1}}{1+g_{22}e^{2\gamma_{22}d_1}}$$

$$g_{11}=\frac{C_1-C_{21}M_{11}}{C_1+C_{21}M_{11}}e^{-2\gamma_1 d_1}\ ,\ g_{12}=\frac{C_1-C_{22}M_{12}}{C_1+C_{22}M_{12}}e^{-2\gamma_1 d_1}$$

$$G_{11}=\frac{1+g_{11}e^{2\gamma_1 d_1}}{1+g_{21}e^{2\gamma_{21}d_1}}\ ,\ G_{12}=\frac{1+g_{12}e^{2\gamma_1 d_1}}{1+g_{22}e^{2\gamma_{22}d_1}}$$

$$G_{21}=\frac{1+g_{21}e^{2\gamma_{21}d_2}}{1+g_3e^{2\gamma_3 d_2}}\ ,\ G_{22}=\frac{1+g_{22}e^{2\gamma_{22}d_2}}{1+g_3e^{2\gamma_3 d_2}}$$

By setting $C_{21}=C_{22}$, the type of structure (i.e. CS) considered in section 2.1.2 is obtained.

### *2.1.5 Field Properties for General N-Layer Dielectric Structure Terminated by Infinite Half-Space (IHS) in the Near-Field Region*

From the above derivations, it is clear that the solutions tend to be consistent. This tendency can be exploited to generalize the derivations for an N-layer dielectric structure with a uniform inclusion in any layer.

The electric field coefficients in an N-layer dielectric structure can be determined using the approach adopted in section 2.1.1. For N-layer structure, there are 2N-1 coefficients to be determined. The coefficients in the $n^{th}$ layer are

$$A_{yn} = \begin{Bmatrix} \dfrac{\left(\prod_{i=1}^{n} G_{i-1}\right) I}{1+g_1}\phi_{n-1} & : n \in [1, N-1] \\ \dfrac{\left(\prod_{i=1}^{n-1} G_{i-1}\right) I}{1+g_1}(1+g_{n-1}e^{2\gamma_{n-1}d_{n-1}})\phi_{n-1} & : n = N \end{Bmatrix} \tag{2.53a}$$

$$B_{yn} = g_n A_{yn} \tag{2.53b}$$

Where

$$g_i = \begin{Bmatrix} \dfrac{C_i - C_{i+1}M_i}{C_i + C_{i+1}M_i}e^{-2\gamma_i d_i} & : i \in [1, N-1] \\ 0 & : i = 0, i = N \end{Bmatrix}$$

$$M_i = \begin{Bmatrix} \dfrac{1-g_{i+1}e^{2\gamma_{i+1}d_i}}{1+g_{i+1}e^{2\gamma_{i+1}d_i}} & : i \in [1, N-2] \\ 1 & : i = N-1 \end{Bmatrix}$$

$$G_i = \begin{Bmatrix} 1 & : i \le 0 \\ \dfrac{1+g_i e^{2\gamma_i d_i}}{1+g_{i+1}e^{2\gamma_{i+1}d_i}} & : i \in [1, N-2] \end{Bmatrix}$$

$$\phi_i = \begin{Bmatrix} 1 & : i = 0 \\ \prod_{j=1}^{i} e^{-\gamma_j d_j} e^{\gamma_{j+1} d_j} & : i \in [1, N-1] \end{Bmatrix}$$

### *2.1.6 Field Properties for General N-Layer Dielectric Structure Terminated by a Conducting Sheet (CS) in the Near-Field Region*

The above approach can be used to find the electric field coefficients in an N-layer structure backed by a conductor sheet. In this case, there are 2N coefficients to be determined. The coefficients in the $n^{th}$ layer are:

$$A_{yn} = \frac{\left(\prod_{i=1}^{n} G_{i-1}\right) I}{1+g_1} \phi_{n-1} \tag{2.54a}$$

$$B_{yn} = g_n A_{yn} \tag{2.54b}$$

Where

$$g_i = \left\{ \begin{array}{ll} \dfrac{C_i - C_{i+1} M_i}{C_i + C_{i+1} M_i} e^{-2\gamma_i d_i} & : i \in [1, N-1] \\ -e^{-2\gamma_i d_i} & : i = N \end{array} \right\}$$

$$M_i = \frac{1 - g_{i+1} e^{2\gamma_{i+1} d_i}}{1 + g_{i+1} e^{2\gamma_{i+1} d_i}} \qquad : i \in [1, N-1]$$

$$G_i = \left\{ \begin{array}{ll} 1 & : i \le 0 \\ \dfrac{1 + g_i e^{2\gamma_i d_i}}{1 + g_{i+1} e^{2\gamma_{i+1} d_i}} & : i \in [1, N-1] \end{array} \right\}$$

$$\phi_i = \left\{ \begin{array}{ll} 1 & : i = 0 \\ \prod_{j=1}^{i} e^{-\gamma_j d_j} e^{\gamma_{j+1} d_j} & : i \in [1, N-1] \end{array} \right\}$$

### *2.1.7 Field Properties for General N-Layer Dielectric Structure Terminated by Infinite Half-Space (IHS) with an Inclusion (Tumour) in the Near-Field Region*

The derivations in section 2.1.3 can be generalized by assuming that the inclusion (tumour) exists at the same location (i.e. 2nd layer). The fields' coefficients are:

$$A_{ynm} = \begin{Bmatrix} \dfrac{\left(\prod_{i=1}^{n} G_{(i-1)m}\right) I}{1+g_{1m}} \phi_{(n-1)m} & : n \in [1, N-1] \\ \dfrac{\left(\prod_{i=1}^{n-1} G_{(i-1)m}\right) I}{1+g_{1m}} (1+g_{(n-1)m} e^{2\gamma_{(n-1)m} d_{n-1}}) \phi_{(n-1)m} & : n = N \end{Bmatrix} \tag{2.55a}$$

$$B_{ynm} = g_{nm} A_{ynm} \tag{2.55b}$$

Where

$$g_{im} = \begin{Bmatrix} \dfrac{C_{im} - C_{(i+1)m} M_{im}}{C_{im} + C_{(i+1)m} M_{im}} e^{-2\gamma_{im} d_i} & : i \in [1, N-1] \\ 0 & : i = 0, i = N \end{Bmatrix}$$

$$M_{im} = \begin{Bmatrix} \dfrac{1 - g_{(i+1)m} e^{2\gamma_{(i+1)m} d_i}}{1 + g_{(i+1)} e^{2\gamma_{(i+1)m} d_i}} & : i \in [1, N-2] \\ 1 & : i = N-1 \end{Bmatrix}$$

$$G_{im} = \begin{Bmatrix} 1 & : i \le 0 \\ \dfrac{1 + g_{im} e^{2\gamma_{im} d_i}}{1 + g_{(i+1)m} e^{2\gamma_{(i+1)m} d_i}} & : i \in [1, N-2] \end{Bmatrix}$$

$$\phi_{im} = \begin{Bmatrix} 1 & : i = 0 \\ \prod_{j=1}^{i} e^{-\gamma_{jm} d_j} e^{\gamma_{(j+1)m} d_j} & : i \in [1, N-1] \end{Bmatrix}$$

The subscript ($m$) indicates the region such that $m$ = 1 refers to the region of inclusion (tumour), i.e. $x \in [x_1, x_2], y \in [y_1, y_2]$. While $m$ = 2 indicates the points out of that region.

### *2.1.8 Field Properties for General N-Layer Dielectric Structure Terminated by a Conducting Sheet (CS) with an Inclusion (Tumour) in the Near-Field Region*

The derivations in 2.1.4 can be generalized by assuming that the inclusion (tumour) exists at the same location (i.e. 2nd layer). The fields' coefficients are

$$A_{ynm} = \frac{\left(\prod_{i=1}^{n} G_{(i-1)m}\right) I}{1 + g_{1m}} \phi_{(n-1)m} \tag{2.56a}$$

$$B_{ynm} = g_{nm} A_{ynm} \tag{2.56b}$$

Where

$$g_{im} = \begin{cases} \dfrac{C_{im} - C_{(i+1)m} M_{im}}{C_{im} + C_{(i+1)m} M_{im}} e^{-2\gamma_{im} d_i} & : i \in [1, N-1] \\ -e^{-2\gamma_{im} d_i} & : i = N \end{cases}$$

$$M_{im} = \frac{1 - g_{(i+1)m} e^{2\gamma_{(i+1)m} d_i}}{1 + g_{(i+1)m} e^{2\gamma_{(i+1)m} d_i}} \qquad : i \in [1, N-1]$$

$$G_{im} = \begin{cases} 1 & : i \le 0 \\ \dfrac{1 + g_{im} e^{2\gamma_{mi} d_i}}{1 + g_{(i+1)m} e^{2\gamma_{(i+1)m} d_i}} & : i \in [1, N-1] \end{cases}$$

$$\phi_{im} = \begin{cases} 1 & : i = 0 \\ \displaystyle\prod_{j=1}^{i} e^{-\gamma_{jm} d_j} e^{\gamma_{(j+1)m} d_j} & : i \in [1, N-1] \end{cases}$$

The subscript ($m$) indicates the region such that $m$ = 1 refers to the region of inclusion (tumour), i.e. $x \in [x_1, x_2], y \in [y_1, y_2]$. Whereas $m$ = 2 indicates the points out of that region.

Note that if the layers are to be homogenous except for the second layer, the subscript $m$ is not needed. Once again, the consistency of the solution suggests that this case is the general form of solution.

## *2.2 Electric Field and Power Pattern Analysis for General N-Layer Dielectric Structure*

After the electric and magnetic field components are formulated and calculated, normalized electric field intensity and power density patterns can be obtained to study the radiation properties of an open-ended rectangular waveguide sensor into the breast under inspection. For the power density calculations, the time average Poynting vector $\overline{P}$ is given by

$$\overline{P} = \frac{1}{2}\left(\overline{E} \times \overline{H^*}\right) \tag{2.57}$$

Where, $*$ denotes the complex conjugate and

$$\overline{E} = \hat{x}E_x + \hat{y}E_y + \hat{z}E_z \tag{2.58a}$$

$$\overline{H} = \hat{x}H_x + \hat{y}H_y + \hat{z}H_z \tag{2.58b}$$

The real part of $\overline{P}$ represents the radiated power density and the imaginary part represents the reactive (stored) power density.

## *2.3 Reflection Coefficient Analysis at the Aperture of the Open-Ended Rectangular Waveguide Sensor in the Near-Field Region*

To find the reflection coefficient, the x-component of the magnetic field:

$$\overline{H}_n(x,y,z) = \frac{j}{\varpi\mu_n}\int_{-\infty}^{\infty}\int_{-\infty}^{\infty}(\overline{c}_{2n}A_{yn}e^{-\gamma_n z} + \overline{c}_{4n}B_{yn}e^{\gamma_n z})e^{j(k_x x + k_y y)}dk_x dk_y \tag{2.59}$$

has to be expressed at the aperture, i.e., at $z = 0$, i.e. in the first layer. Thus

$$H_{x1}(x,y,0) = \frac{j}{\varpi\mu_1}\int_{-\infty}^{\infty}\int_{-\infty}^{\infty}(\overline{c}_{21}A_{y1} + \overline{c}_{41}B_{y1})e^{j(k_x x + k_y y)}dk_x dk_y \tag{2.60}$$

Where (from equations (2.15.2) and (2.15.4)):

$$\overline{c}_{21} = -\hat{x}\frac{K_1^2 - k_x^2}{\gamma_1} + \hat{y}\frac{k_x k_y}{\gamma_1} + \hat{z}(jk_x)$$

$$\overline{c}_{41} = \hat{x}\frac{K_1^2 - k_x^2}{\gamma_1} - \hat{y}\frac{k_x k_y}{\gamma_1} + \hat{z}(jk_x)$$

and

$$\gamma_1 = \sqrt{k_x^2 + k_y^2 - K_1^2}\ ,$$

$$K_1^2 = K_0^2\varepsilon_r\mu_r\ ,$$

$K_0^2 = \omega^2\varepsilon_o\mu_o$ and let $\mu_o = \mu_1 = 1$.

But from equation (2.2), $\overline{H_{ap}}$ has x-component only. Thus:

$$H_{x1}(x,y,0)=\frac{j}{\varpi}\int_{-\infty}^{\infty}\int_{-\infty}^{\infty}\left[\frac{K_1^2-k_x^2}{\gamma_1}B_{y1}-\frac{K_1^2-k_x^2}{\gamma_1}A_{y1}\right]e^{j(k_x x+k_y y)}dk_x dk_y \tag{2.61}$$

For these derivations, we have assumed $TE_{10}$ mode as the *only* incident mode and reflected mode at the aperture. For the $TE_{10}$ mode, the aperture tangential electric and magnetic fields are y and x directed respectively. Since the tangential fields must be continuous at the aperture satisfying boundary conditions, the reflected magnetic field has only x term (it has also a z term, but it is not tangential to the aperture). That is why at z=0, x term only for the magnetic field should exist. (Note the aperture by itself is not a "mode-converter", meaning that, if the incident fields have a certain polarization, the reflected fields should have the same polarization). Higher order modes based derivations are more complete for this case. This is true since the discontinuouity instituted by the aperture excites higher order modes although the incident mode from z<0 is only $TE_{10}$. The effect of higher order modes can be neglected especially for lossy material like the breast tissue [Enc.86] [Mac.80] [She.97] [Teo.85].

Now, let

$c_{11}=\frac{K_{11}^2-k_x^2}{\gamma_{11}}$, $K_{11}$ and $\gamma_{11}$ for inclusion (tumour) region.

$c_{12}=\frac{K_{12}^2-k_x^2}{\gamma_{12}}$, $K_{12}$ and $\gamma_{12}$ for the breast region.

From equations (2.55a) and (2.55b); {n=1}:

$$A_{y11}=\frac{I}{1+g_{11}},\ A_{y12}=\frac{I}{1+g_{12}} \tag{2.62}$$

$$B_{y11}=g_{11}A_{y11},\ B_{y12}=g_{12}A_{y12} \tag{2.63}$$

Also, it can be shown that the Fourier transform of the aperture field is given by [Qad.98a]:

$$I = QI^* = \int_0^b \int_0^a \overline{E}_{ap}(x,y) e^{j(k_x x + k_y y)} dk_x dk_y$$

$$= Q\left[\frac{\pi/a}{\pi/a - k_x^2}\left(e^{-jk_x a} + 1\right)\right]\frac{e^{-jk_y b} + 1}{jk_y} \tag{2.64}$$

Where $Q = (1+\Gamma)\dfrac{j\omega}{(2\pi)^2 a k_{c10}^2}$ (2.65)

and $I^*$ is the normalized aperture integral.

Substituting equation (2.64) into equations (2.63) and (2.62), then in equation (2.61) yields:

$$H_{x1}(x,y,0) = \frac{-(1+\Gamma)}{(2\pi)^2 a k_{c10}^2}\left\{\begin{array}{l}\displaystyle\int_{-\infty}^{\infty}\int_{-\infty}^{\infty}\frac{c_{11}I^*}{1+g_{11}}(-1+g_{11})e^{j(k_x x+k_y y)}dk_x dk_y \ldots\ldots : x\in[x_1,x_2], y\in[y_1,y_2] \\ \displaystyle\int_{-\infty}^{\infty}\int_{-\infty}^{\infty}\frac{c_{12}I^*}{1+g_{12}}(-1+g_{12})e^{j(k_x x+k_y y)}dk_x dk_y \ldots\ldots : otherwise\end{array}\right\} \tag{2.66}$$

Over the aperture, equation (2.66) can be equated with equation (2.2). This will result in:

$$(1-\Gamma)\frac{j\pi\omega\mu}{a k_{c10}^2} Y_o \sin(\frac{\pi x}{a}) = \frac{-(1+\Gamma)}{(2\pi)^2 a k_{c10}^2}\left\{\begin{array}{l}\displaystyle\int_{-\infty}^{\infty}\int_{-\infty}^{\infty}\frac{c_{11}I^*}{1+g_{11}}(-1+g_{11})e^{j(k_x x+k_y y)}dk_x dk_y \ldots\ldots : x\in[x_1,x_2], y\in[y_1,y_2] \\ \displaystyle\int_{-\infty}^{\infty}\int_{-\infty}^{\infty}\frac{c_{12}I^*}{1+g_{12}}(-1+g_{12})e^{j(k_x x+k_y y)}dk_x dk_y \ldots\ldots : otherwise\end{array}\right\} \tag{2.67}$$

From, the above, the admittance at the waveguide aperture as a function of x and y can be written as:

$$Y_s(x,y) = \frac{j}{4\pi^3 \omega\mu Y_o \sin(\frac{\pi x}{a})}\left\{\begin{array}{l}\displaystyle\int_{-\infty}^{\infty}\int_{-\infty}^{\infty}\frac{c_{11}I^*}{1+g_{11}}(-1+g_{11})e^{j(k_x x+k_y y)}dk_x dk_y \ldots\ldots : x\in[x_1,x_2], y\in[y_1,y_2] \\ \displaystyle\int_{-\infty}^{\infty}\int_{-\infty}^{\infty}\frac{c_{12}I^*}{1+g_{12}}(-1+g_{12})e^{j(k_x x+k_y y)}dk_x dk_y \ldots\ldots : otherwise\end{array}\right\} \tag{2.68}$$

The complex reflection coefficient at the aperture of the waveguide, $\Gamma$ , is related to the complex admittance at the waveguide aperture, $Y_s$ , by:

$$\Gamma = |\Gamma| e^{j\phi} = \frac{1 - Y_s}{1 + Y_s} \tag{2.69}$$

Which is a complex quantity whose phase and magnitude can be calculated and measured for comparison and optimisation. The above expression is valid for those points (x, y) Є aperture. The above derivations apply for all types and scenarios for N-layer dielectric material with inclusion (tumour). This is the reflection coefficient measured at each scanned point in the imaging plane. Using this model, the image formation process can be analyzed and simulated.

## *2.4 Summary and Remarks*

After developing a general model that describes the near-field radiation properties of the open-ended rectangular waveguides radiating into infinite half-space of dielectric, it is worthwhile to summarize the above sections and emphasize the final model and parameters that will be the point of interest in the simulation analysis because there are many equations and derivations in the previous sections. Thus, as mentioned earlier, the intention is to calculate and simulate the near-field radiation properties, namely the normalized electric field, the real power pattern and the imaginary power pattern. Then, calculate and obtain theoretical 2-D images of the phase and magnitude of the reflection coefficient at the rectangular waveguide aperture. Thus, equations (2.16) (2.57) and (2.69) will be the explicit solutions for the simulation analysis that will be presented in Chapter 3 of this thesis.

Moreover, the general N-layer dielectric structure terminated by infinite half-space (IHS) with an inclusion (tumour) in the near-field region developed in section

2.1.7 will be employed. This is because the breast is a high-loss dielectric material, even if the breast is conductor backed; the signal will not reach the end of the breast. Also, it will be easier and smoother for the patient when imaging the breast since there will be no need to locate any metallic plate at the opposite end of the imaging plane and no need to compress the breast tissue. But the conductor-backed scenario is derived here for the purpose of future research in case there is a possibility of integrating near-field microwave imaging with other screening tools or testing techniques. Additionally, if the breast size is small and the penetration depth is high, then there is a chance that the signal will reach the end of the breast. Then, adding a conductor sheet at the end will increase the detection sensitivity since total reflection will occur and the breast is effectively screened twice.

Last but not least, obtaining a general model for N-layer dielectric structure rather than for few layers can be the basis for advanced research and investigation concerning breast cancer detection using near-field microwave techniques. The N-layer model will be particularly useful when precise measurements of the dielectric properties of breast tissues and its constituents exist, leading to a detailed ideal breast model based on the parts of the breast (such as fat, blood, skin, muscle, etc.), their quantity, their dielectric properties and their physical dimensions. Having a detailed breast model should therefore help to obtain an optimized microwave breast cancer detection system.

# *CHAPTER 3*

## *Radiation Patterns and Reflection Coefficient Simulation Analysis Applied to Breast Cancer Detection*

### *3.1 Code Development*

From the nature of the mathematical model presented in the previous chapter, it shows that the model is quite complex and it is hard to interpret the physical interaction by looking at the equations directly. Thus, it is essential to code the mathematical model efficiently so the patterns and the field interaction with the breast tissue model under inspection as well as the reflection theoretical images can be visualized and analysed.

The MATLAB programming environment was utilized extensively to code, analyze and simulate the interaction model. Figure 3-1 shows the flowchart of the code developed. The code developed performs the following task:

a. Calculation of the electric field and power patterns in multilayer dielectric structure with any type of termination, as represented in equations (2.16) and (2.57) respectively as follows:

$$E_{yn}(x,y,z) = \int_{-\infty}^{\infty}\int_{-\infty}^{\infty} F_{yn}(k_x,k_y,z)e^{j(k_x x+k_y y)}dk_x dk_y \tag{3.1}$$

$$\overline{P} = \frac{1}{2}\left(\overline{E}\times\overline{H^*}\right) \tag{3.2}$$

b. Calculation of the reflection coefficient at the waveguide aperture, as has been derived in equation (2.69), i.e.

$$\Gamma = \left|\Gamma\right|e^{j\phi} = \frac{1-Y_s}{1+Y_s} \tag{3.3}$$

c. Formation of reflection 2-D theoretical images for possible inclusion (tumour).

The developed code was subjected to a theoretical verification process. The theoretical validation relied on the basic electromagnetic theory of uniqueness. Simply, this theory states that the solution of the electric field that satisfies the boundary conditions in the problem is the only solution [Bal.97]. Since the derivation of the model was fundamentally based on enforcing the boundary conditions at the interfaces between the dielectric layers, it is rational to expect that the derived solution of the electric field does satisfy the boundary conditions. In fact, this resulted in the consistency found in the solution, as it was pointed out in chapter 2 of this thesis.

The developed code for some cases has a long execution time because of the use of many numerical vector analyses and "if loops" statements. For example, Figure 3-14 took several hours if not a whole day till the image was obtained. Thus, further research can be done in future to obtain more efficient code with reduced execution time, if necessary. Also, it is advisable to put the developed code with all its subroutines into a single user-friendly graphical user interface, a feature not offered in the present version of the code. Finally, the code developed in this chapter is based on so many mathematical approximations and this might result in small discrepancies between the simulation and experimental results as will be shown in results of chapter 5 of this thesis.

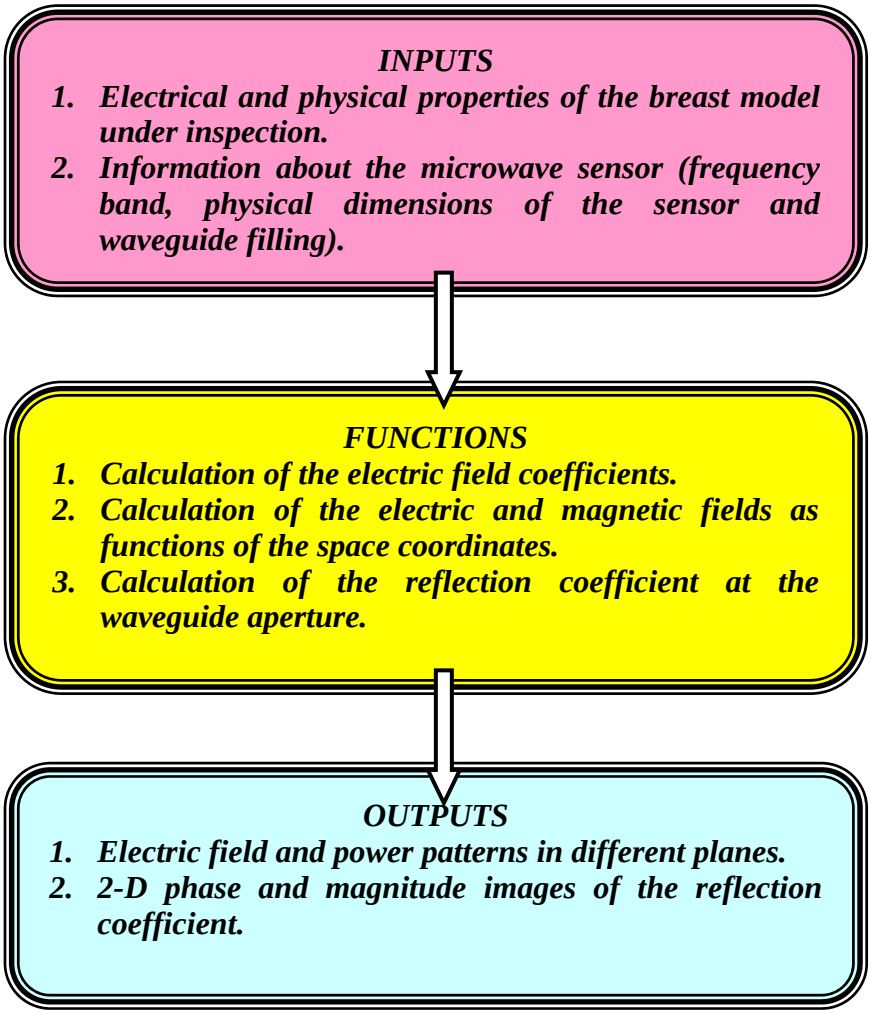


Figure 3-1: Flow chart for the code developed.

## *3.2 Radiation Patterns and Reflection Images of Cancerous Breast Tissues for Different Tumour Depths*

The breast model used in this investigation is assumed to be a 3-layer dielectric structure with a tumour (inclusion) embedded within the breast tissue. This model is consistent with the N-layer dielectric structure model presented in chapter 2 and shown in Figure 2-1. The model consists of breast tissue surrounded by an outer layer of skin as mentioned in chapter 1 and illustrated in Figure 3-2. Thus the model is composed of the following: layer 1: skin; $\varepsilon_{r1} = 36$ and $\sigma_1 = 4$ S/m, thickness = 2 mm. Layer 2: breast

tissue; $\varepsilon_{r2}$ = 9 and $\sigma_2$ = 0.4 S/m, thickness = 60 mm. Layer 3: skin; $\varepsilon_{r3}$ = 36 and $\sigma_3$ = 4 S/m, thickness = 2 mm. A tumour ($\varepsilon_{ri}$ =50 and $\sigma_i$ = 4 S/m) with dimensions of 6 mm x 6 mm x 3 mm is introduced within the breast tissue and its location is at z = 25, 20, 15, 10, and 5 mm (where z is the direction of propagation) as shown in Figure 3-2 [Fea.00] [Sal.03b] [Sal.04] [Sal.05] [Sal.06].

The breast might be terminated by an infinite half-space (IHS) of air or a conductor sheet (CS). All the theoretical and experimental investigations are conducted for an infinite half-space of air termination because the breast is classified as high lossy material and few portion of the microwave signal will reach the termination point. In addition, it is more comfortable for the patient because the metallic sheet is not attached to the breast and thus breast compression is avoided. The open-ended rectangular waveguide sensor is centred at the origin with its board dimension ($a$) along the x-axis and the narrow dimension ($b$) along the y-axis. The $TE_{10}$ excitation mode for the open-ended rectangular waveguide with propagation in the z-direction is considered. An X-band (8.2 GHz – 12.4 GHz) ($a$ = 22.86 mm, $b$ = 10.16 mm) rectangular waveguide sensor in contact with the breast is utilized in the simulation analysis.

The simulation results include the radiation patterns and the reflection coefficient. The radiation patterns are presented as the magnitude of the normalized electric field, $\overline{|E|}$, real, and imaginary power patterns in different planes and for different tumour depths. The field distributions are obtained with steps of 0.1 mm, 0.1a, and 0.1b in the z, x, and y directions, respectively. The magnitude of the radiated field is either normalized for the electric field or in decibels (dB) for the radiated power. Then the effective reflection coefficient at the probe's aperture is illustrated as magnitude and phase for several scenarios in 1-D and 2-D fashions.

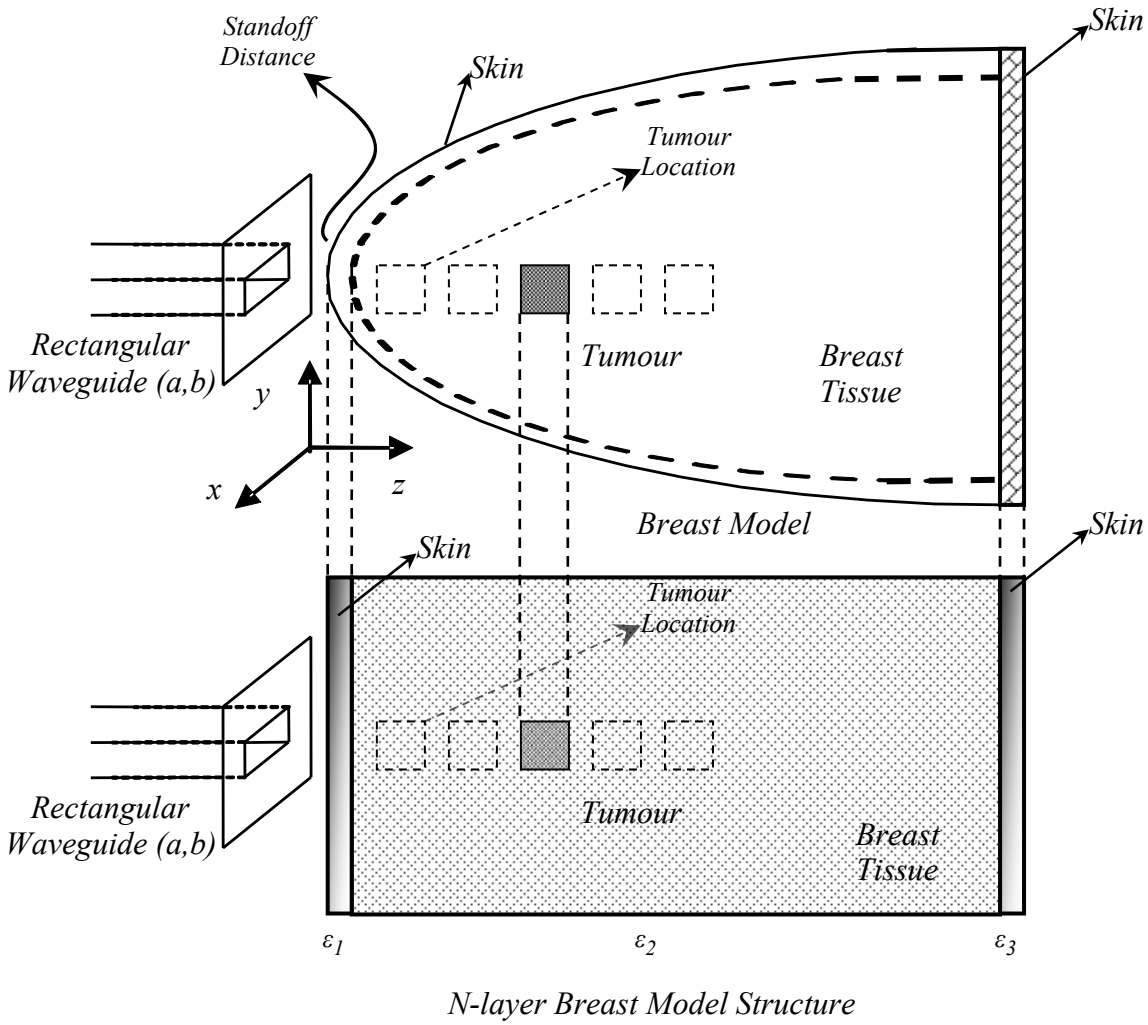


Figure 3-2: Breast model analogy with N-layer dielectric model developed in chapter 2 with an open-ended rectangular waveguide sensor for tumour detection.

Figures 3-3 to 3-5 show the normalized electric field, real power pattern (in dB) and imaginary power pattern (in dB) (as one dimensional pattern) as a function of the direction of propagation (z) at $x = \frac{a}{2}$ mm and $y = \frac{b}{2}$ mm for multiple tumour depths of 25, 20, 15, 10, and 5 mm and with 10.5 GHz operating frequency. As expected, for all tumour depths, the electric field as well as the power decrease as the waves propagate and interact with the breast tissue. The fields and power trends for all tumour depths match closely each other. This shows the consistency of the fields behaviour when they interact with the breast under inspection.

For each tumour depth, there is a notable change in the electric field properties at the tumour interface. For example when the tumour is 5 mm depth, the electric field

intensity changes at z = 5 mm (i.e. tumour interface) accordingly. Since breast tissue is a lossy dielectric material, it exhibits small (but nonzero) conductivity and absorbs some electromagnetic energy. This results in the attenuation of the electromagnetic waves as they propagate through the breast tissue. Referring to equation (3.1) and its details in chapter 2 of this thesis, the electric field, and hence the power, has a complex propagation constant, $\gamma$ whose real part represents the attenuation factor, $\alpha$, that is a measure of the spatial rate of decay of the microwave signal in the breast tissue.

Although Figures 3.3 to 3.5 are useful to show how the field interacts with the breast tissue, there is no information that can be extracted to obtain optimisation parameters. For example, it is not evident that the chosen frequency of 10.5 GHz frequency is an optimum frequency or not. Further analyses have to be conducted and more results have to be presented in more expressive way to help understand and optimise the near-field imaging system.

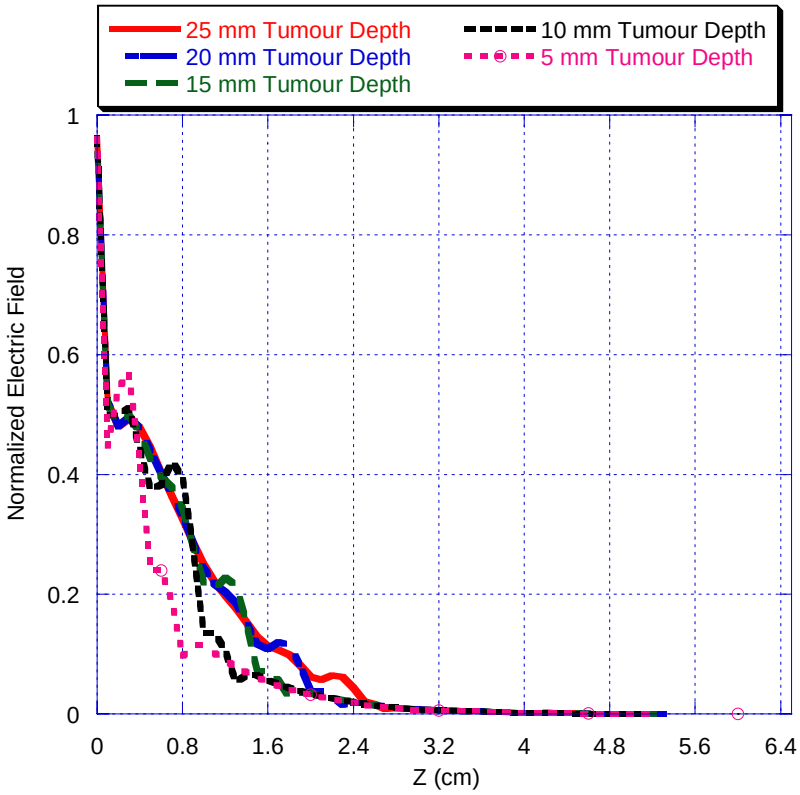


Figure 3-3: Normalized electric field as a function of z at x=a/2 and y=b/2 with a 6x6x3 mm³ tumour at different depths and for 10.5 GHz operation.

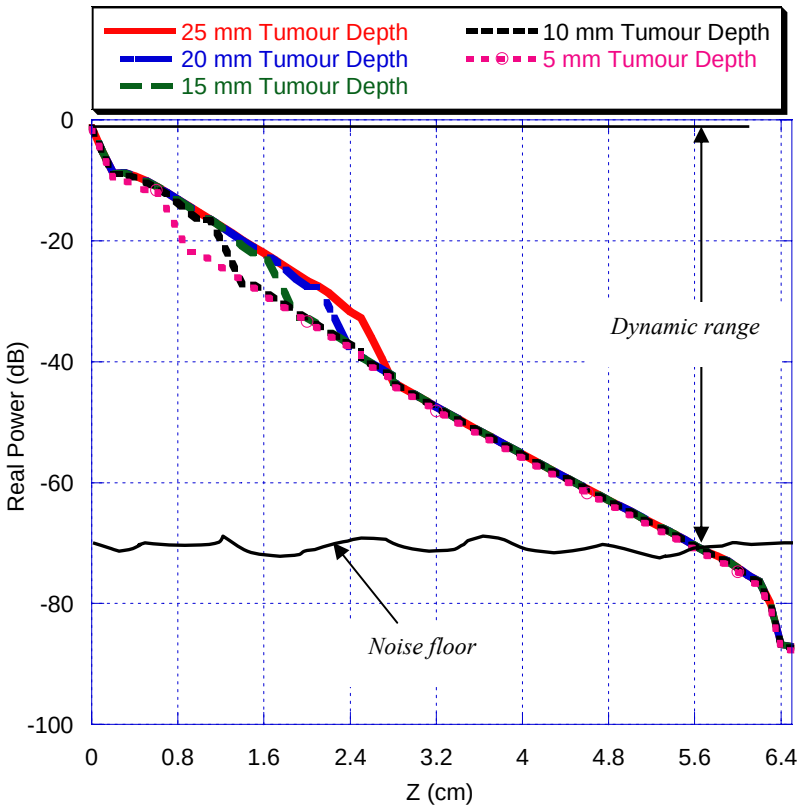


Figure 3-4: Real power as a function of z at x=a/2 and y=b/2 with a 6x6x3 mm³ tumour at different depths and for 10.5 GHz operation.

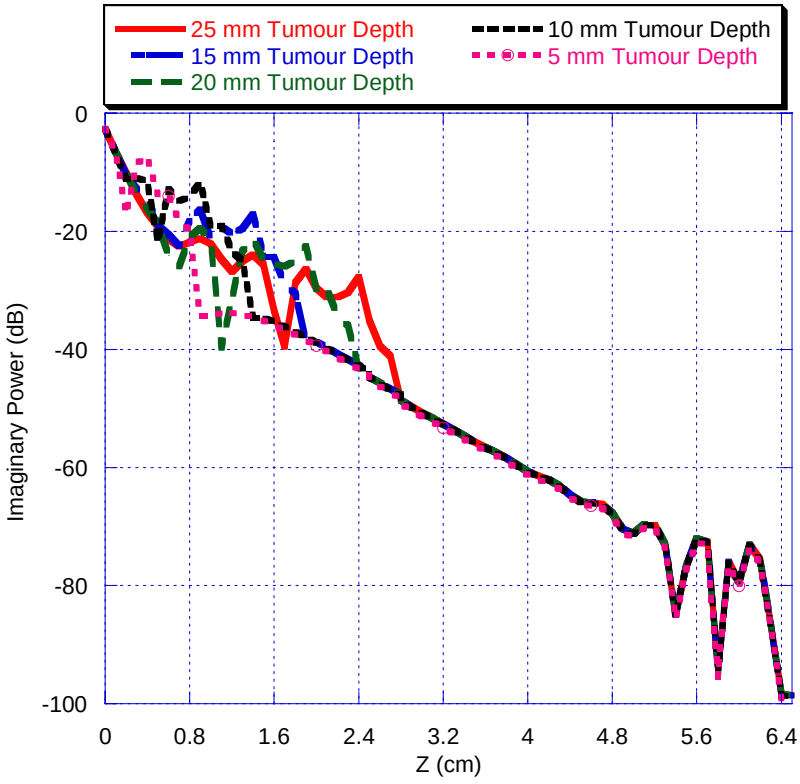


Figure 3-5: Imaginary power as a function of z at x=a/2 and y=b/2 with a 6x6x3 mm³ tumour at different depths and for 10.5 GHz operation.

Figure 3-6 shows the real power pattern (in dB) (as one dimensional pattern) as a function of x at $y = \frac{b}{2}$ mm and z = tumour depth (tumour interface) for multiple tumour depths at 10.5 GHz. It is clear from the figure that whenever the tumour becomes deeper, the power radiated from the sensor to the breast decreases. The maximum power is attained when the tumour is 5 mm deep. Furthermore, when the microwave probe is directly in front of the tumour, the power increases compared to power when over 'normal' breast tissue. The reason behind this is that the conductivity for tumour ($\sigma_i$ = 4 S/m) is ten times the breast tissue conductivity ($\sigma_2$ = 0.4 S/m). As a consequence, the power is proportional to the conductivity according to Joule's law [Sad.95] [Ina.99].

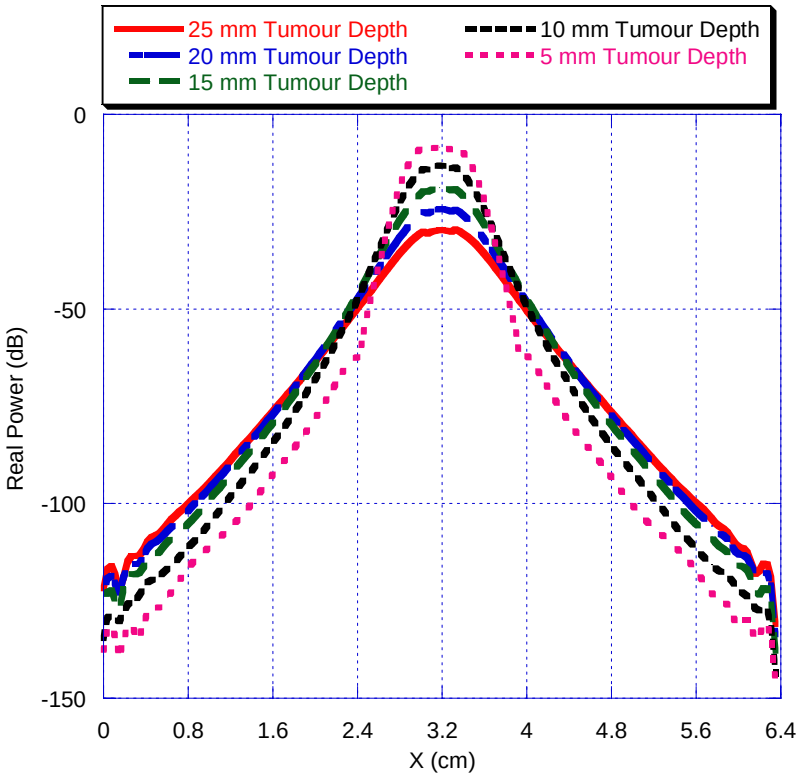


Figure 3-6: Real power as a function of x at y=b/2 and z=tumour depth with a 6x6x3 mm³ tumour at different depths and for 10.5 GHz operation.

The radiation patterns for all tumour depths are quite similar in terms of their general shape and behaviour. Therefore, the radiation patterns for 5 mm tumour depth are analysed comprehensively for different planes and in 2-D fashion, and this should

give an indication of behaviour at other tumour depths. Figure 3-7 shows the real power pattern in the yz-plane at $x = \frac{a}{2}$ operating at 10.5 GHz. The real power is dropped 10 dB below its maximum (at the aperture) at a distance of 2 mm from the aperture; in other words, when the microwaves penetrate the breast tissue and leave the skin. The fields are not confined within the aperture's *b*-dimension. At z = 5 mm and due to the presence of tumour, the real power again is dropped around 25 dB below its maximum (at the aperture). The presence of a tumour alters the radiation field distribution inside the breast tissue. Also, the tumour cell acts as a radiating aperture within the breast tissue since the fields' uniformity changes and the radiation intensity varies. There is almost no presence of sidelobes on the real power pattern in the yz-plane.

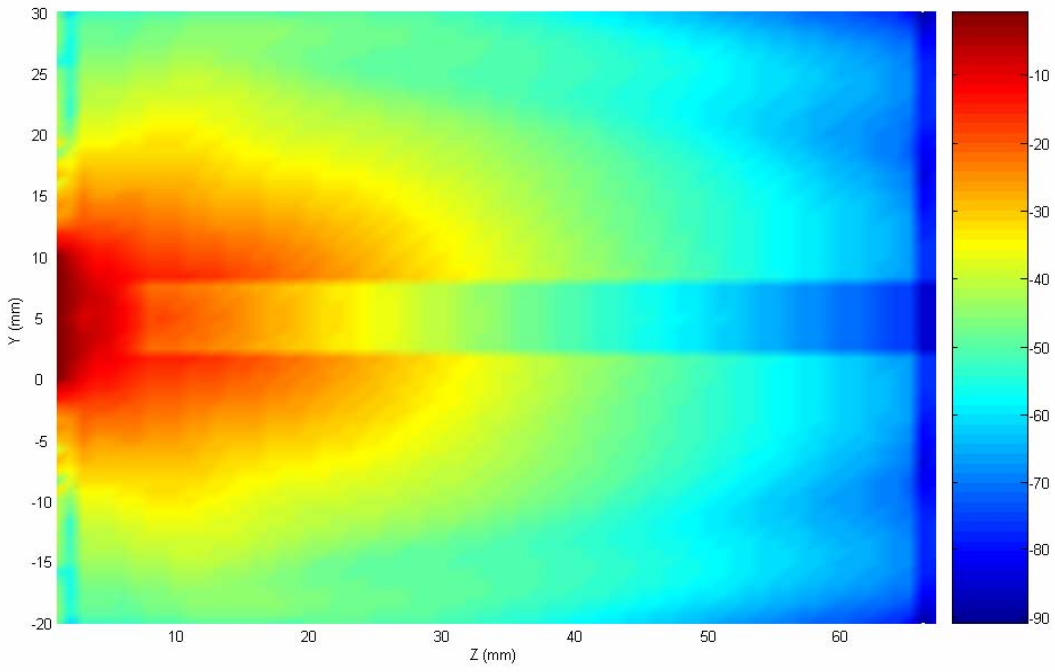


Figure 3-7: Real power pattern (dB) in the yz-plane of the breast with 6x6x3 mm³ tumour at 5 mm depth operating at 10.5 GHz.

Figure 3-8 shows the real power pattern, for the same parameters as in Figure 3-7, in the xz-plane at $y = \frac{b}{2}$. The fields are confined in this plane more than in the yz-plane, and lie generally within the aperture's *a*-dimension up to a long distance inside

the breast tissue. The dielectric mismatch between the skin and the breast tissue is not obvious as in Figure 3-7. The effect of sidelobes appears slightly in this plane, especially at z = 5 mm due to tumour presence. The tumour's finite dimensions as an inclusion within the breast tissue might cause such sidelobes. The interaction of sidelobes with an anomaly (tumour) with high conductivity might produce extra features and information within the reflection image [Qad.95b] [Sal.07].

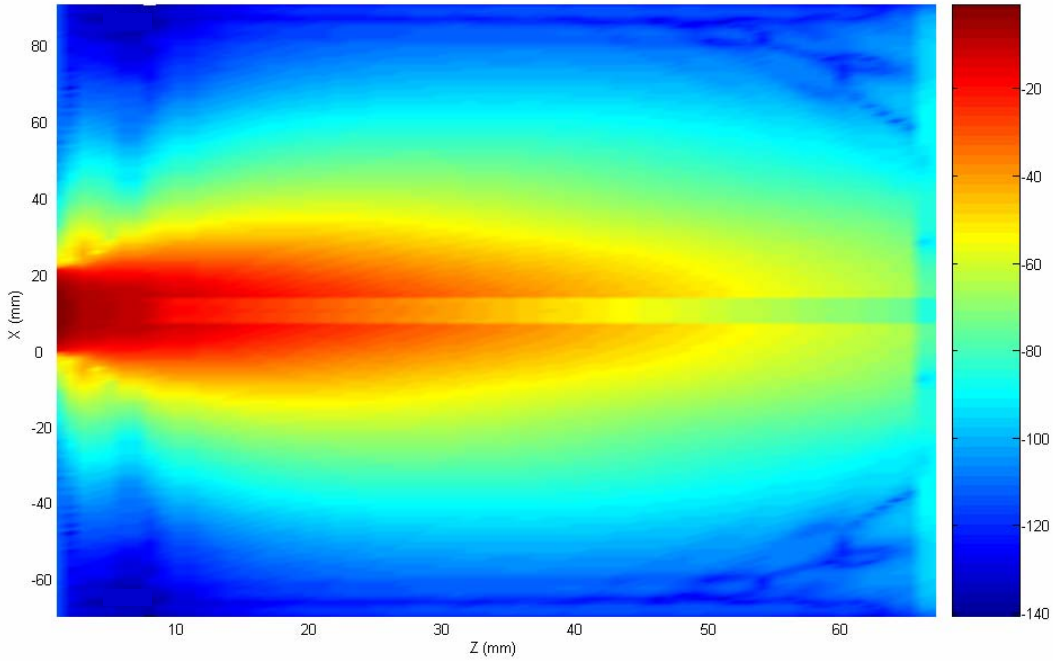


Figure 3-8: Real power pattern (dB) in the xz-plane of the breast with 6x6x3 mm³ tumour at 5 mm depth operating at 10.5 GHz.

Due to the multiple reflections within each layer (media discontinuity) and the nature of the breast being high lossy dielectric material, there is certain amount of power stored in the standing waves in these layers. This power is imaginary in nature, and it is concentrated along the axis of the waveguide on each interface. The imaginary power pattern in the yz-plane at $x = \frac{a}{2}$ for 5 mm tumour depth is shown in Figure 3-9. The fields are again not confined within the aperture's *b*-dimension. Basically, the presence of tumours alters the electric field distribution, and hence the power pattern inside the breast tissue. The presence of sidelobes is not visible in this plane, but there are some sidelobes that do exist especially at the tumour interface.

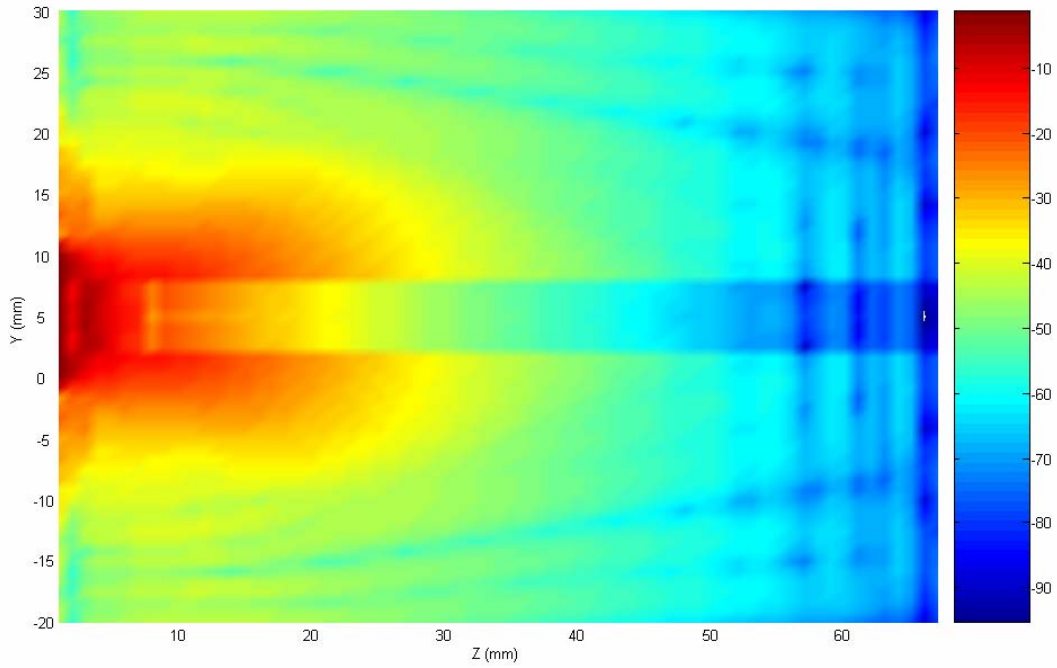


Figure 3-9: Imaginary power pattern (dB) in the yz-plane of the breast with 6x6x3 mm³ tumour at 5 mm depth operating at 10.5 GHz.

To obtain a better vision of the sidelobes, the imaginary power pattern in the xz-plane at $y = \frac{b}{2}$ for 5 mm tumour depth is obtained as shown in Figure 3-10. Two symmetrical sidelobes (marked by X in Figure 3-10), located at 2 mm $\leq$ z $\leq$ 15 mm, forming along the broad sides of the waveguide are observed on the pattern. The presence and effect of the sidelobes may be visualized clearly if higher order modes at the probe aperture are considered in the mathematical derivations [Boi.99]. Yet again, from the pattern it is clear that the fields are confined within the aperture of the waveguide. The fact that the fields in the breast remain confined within the aperture dimensions of the waveguide explains the high resolution associated with the near-field microwave images that can be obtained.

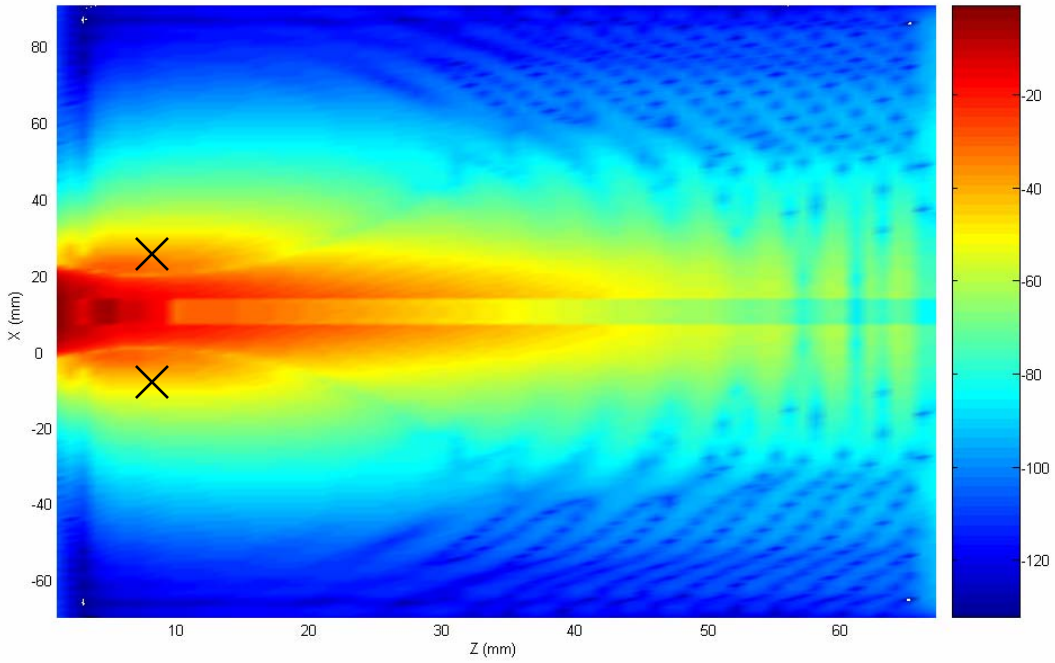


Figure 3-10: Imaginary power pattern (dB) in the xz-plane of the breast with 6x6x3 mm³ tumour at 5 mm depth operating at 10.5 GHz.

To show more clearly the relationship between the power pattern in the breast and the model itself, Figure 3-11 shows the real power pattern of the breast with 6x6x3 mm³ tumour superimposed on the breast model adopted in this thesis. The tumour in this case is at 20 mm depth and the frequency of operation is 10.5 GHz. The effect of skin layer is clearly visible on the pattern, where discontinuity of the fields takes place due to the dielectric mismatch between the skin and the breast tissue. Also, the tumour presence is observable from the pattern, and the location of the tumour can be obtained from the power pattern. The fact that the fields' interaction with the breast under inspection is demonstrated so clearly gives an impression of the promise of near-field microwave non-invasive testing and evaluation (NIT&E) technique for breast cancer detection. However, this doesn't guarantee that the running parameters (such as frequency of operation, probe's loading material, standoff distance) are optimised. Thus, the effective reflection coefficient at the sensor's aperture must be calculated and presented in terms of magnitude and phase in 1-D and 2-D fashions to obtain optimised parameters.

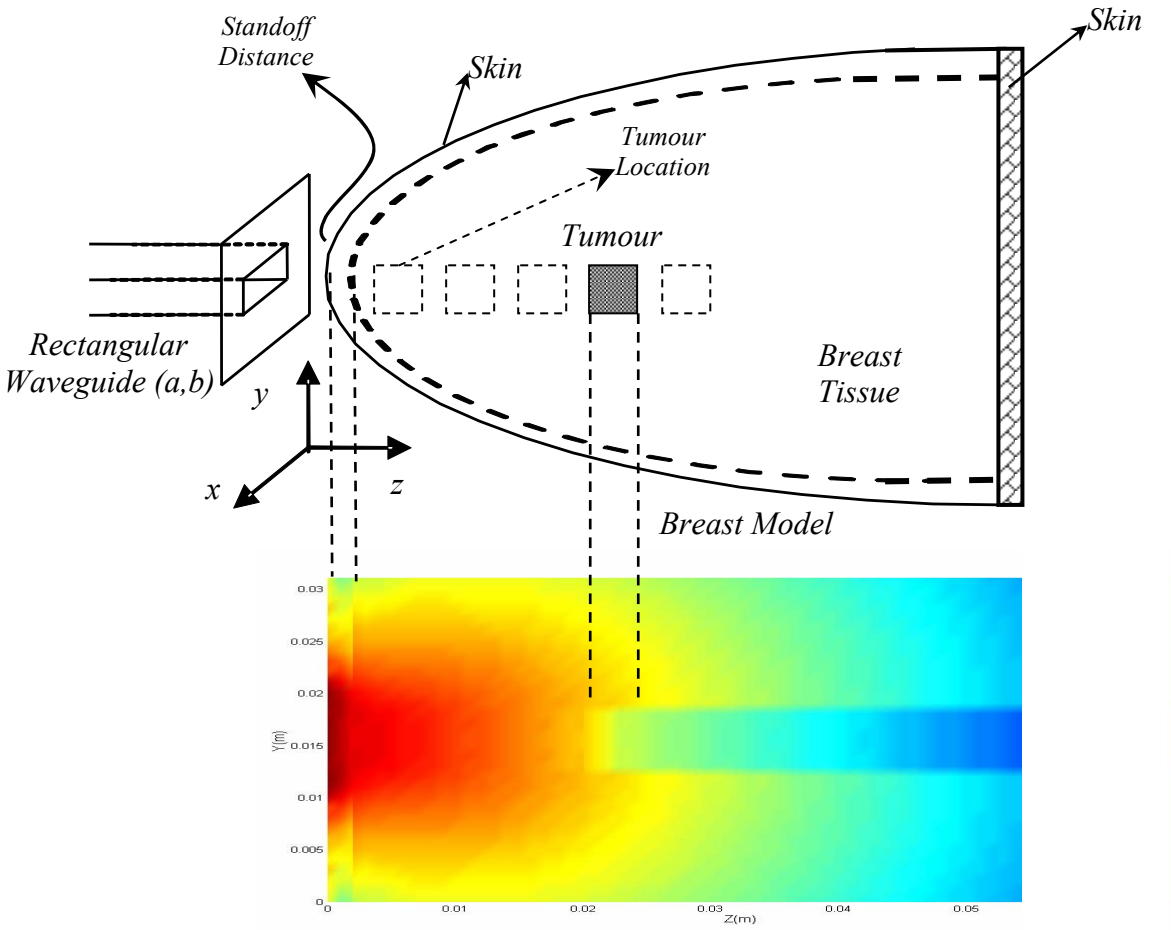


Figure 3-11: Superimposing real power pattern (dB) of the breast with 6x6x3 mm³ tumour at 20 mm depth at 10.5 GHz on the breast model.

## *3.3 Effect of Loading an Open-Ended Rectangular Waveguide Probe on the Radiation Patterns and Reflection Images of Cancerous Breast Tissues*

When optimum detection of malignant tumour is sought, it becomes crucial to understand how microwaves interact with that layer. Fundamentally, the spatial power pattern inside the breast under inspection constitutes a quantitative measure of the interaction between illuminating microwave fields and the tumour inclusion. The sensitivity and lateral resolution of the proposed technique depends highly on the features of that interaction. While the sensitivity to detect a tumour depends on the amount of power coupled to the layer, the capability of the technique to resolve tumour

of finite extent depends on the sensor footprint at the tumour location. Moreover, lower frequencies penetrate more (deeper) in breast tissue, nevertheless, the size of the waveguide sensor increases drastically at lower frequencies and consequently the resolution degrades rapidly as well.

To overcome this dilemma, open-ended rectangular waveguide sensors loaded with a coupling material may be used to detect tumour presence. This loading increases the amount of power coupled to the breast, reduces the frequency of operation and keeps the small size of the waveguide probe (i.e. increases the penetration depth and maintains the resolution). Previous studies have proved that waveguide filling constitutes a powerful optimisation parameter to inspect material of very high loss tangent [Sal.03a] [Sal.03b]. Basically, the loading of the waveguide sensor confines the spread of radiated power to sensor's aperture further inside the breast. This does not only increase effective coupling of the power into the breast tissue, and hence the sensitivity, but also it enhances the resolution.

To investigate this assertion, the magnitude difference along with the phase difference of the effective reflection coefficient at the sensor's aperture for breast tissue with tumour located at 5 mm depth operating at X-Band are shown in Figures 3-12 and 3-13, respectively. Two configurations for the waveguide probe are adopted for these results; first the waveguide probe is empty and then it is fully loaded with a dielectric material of relative permittivity $\varepsilon_r = 12.25$. Due to the waveguide loading, the frequency band drops from 8.2GHz – 12.4GHz to 2.34GHz – 3.54GHz. This drop is calculated from the open-ended rectangular waveguide probe cut-off frequency equation given by:

$$f_{c_{10}} = \frac{k_c}{2\pi\sqrt{\mu\varepsilon}} = \frac{1}{2\sqrt{\mu\varepsilon}}\sqrt{\left(\frac{m\pi}{a}\right)^2 + \left(\frac{n\pi}{b}\right)^2} = \frac{1}{2a\sqrt{\mu\varepsilon}} \tag{3.4}$$

where $m = 1$ and $n = 0$ for the dominant mode $TE_{10}$, $a$ is the broad dimension of the waveguide, $\mu$ and $\varepsilon$ are the permeability and permittivity of the waveguide filling material [Poz.05].

The upper x-axis in Figures 3-12 and 3-13 shows the frequency for the loaded waveguide and the lower x-axis shows the frequency for the empty waveguide. For the empty waveguide, there is nearly 0.05 in the magnitude difference and 1.2° degrees in the phase difference but there is no obvious optimum frequency of operation. Whereas when the waveguide is completely filled with a dielectric material of relative permittivity $\varepsilon_r = 12.25$, there exists a maximum magnitude difference and a maximum phase difference. The maximum magnitude difference is achieved at the end of the frequency band and it is around 0.57. Whereas the maximum phase difference is obtained at the beginning of the frequency band and it is around 24° degrees. Thus, optimising both magnitude and phase differences together at the same time is not possible, but the frequency around 3.0 GHz appears to be a good compromise choice. The magnitude difference at 3.0 GHz is around 0.53 and the phase difference is 15° degrees.

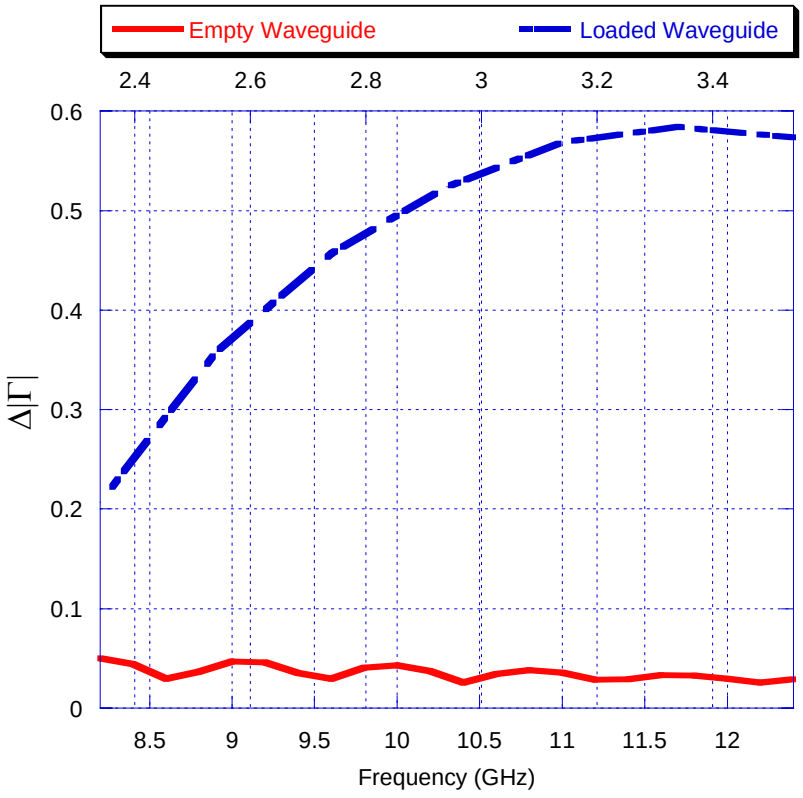


Figure 3-12: The magnitude difference of the effective reflection coefficient at the sensor's aperture for breast tissue with tumour located at 5 mm depth operating at X-Band.

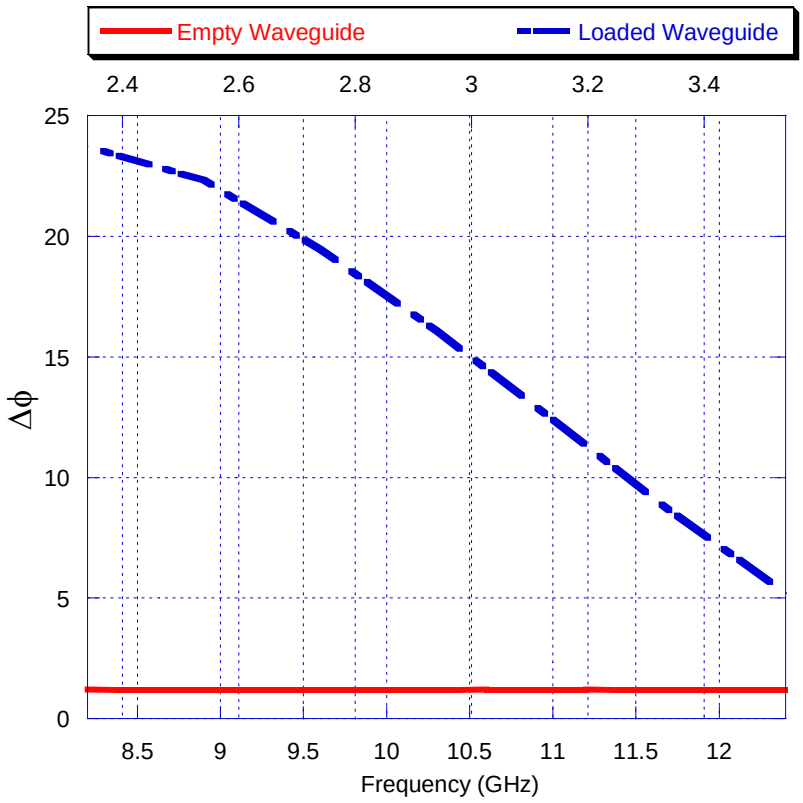


Figure 3-13: The phase difference of the effective reflection coefficient at the sensor's aperture for breast tissue with tumour located at 5 mm depth operating at X-Band.

One of the important factors that controls the selection of the relative permittivity, $\varepsilon_r$, of the loading material is the dielectric properties of the breast model itself, which should be known at the appropriate frequency band. Another factor is the viability of obtaining practically loading material with the desired dielectric properties.

To demonstrate the potential of the theoretical image formation capability on the optimisation process, such as via the use of waveguide probe filling, magnitude and phase reflection images of the breast model mentioned above and illustrated in Figure 3-2 were formed. Two-dimensional reflection images were produced for empty and loaded waveguide probes using equation (3.3) to form the magnitude and phase reflection images for the tumour model considered above.

Figures 3-14a and 3-14b show theoretical 2-D reflection magnitude images of the breast with a 6x6x3 mm³ tumour at 5 mm depth for an empty waveguide probe operating at 10.5 GHz and for a loaded waveguide sensor with dielectric material of $\varepsilon_r =$

12.25 operating at 3.0 GHz, respectively. For the empty waveguide probe, the maximum dynamic range for the magnitude image is 0.05 for 5 mm tumour depth. Whereas for the loaded waveguide, the maximum magnitude difference, $\Delta|\Gamma|$, becomes 0.53. At 10.5 GHz the contrast is positive whereas 3.0 GHz the contrast negative. The reason behind this is that when the waveguide is loaded, the waveguide effective impedance has changed, i.e. the effective admittance has changed and hence the effective reflection coefficient will change (remember the purpose behind loading the waveguide is matching it with the environment, i.e. breast under inspection. These 2-D reflection magnitude images match closely with the results obtained in Figure 3-12. Hence, the magnitude detection sensitivity becomes around ten times better when the microwave sensor is loaded. Accordingly, the detection sensitivity has drastically improved and the presence of the tumour cell can be easily detected. Since the images are obtained in the xy-plane, they can offer direct information about the physical size in x and y dimensions of the tumour [Sal.07].

The reflection magnitude images shown for both waveguide probe settings represent the absolute magnitude difference of the effective reflection coefficient at the probe's aperture. This output is a result of many parameters that are dependent on the microwave sensor settings (such as frequency band, narrow and broad physical dimensions, waveguide filling, etc.) and the properties of the breast under inspection (breast model, dielectric properties and thickness of each constituent, etc.). Furthermore, the microwave probe's aperture acts as a spatial integrator over the exposed area that is of interest. The microwave signal received from the exposed area is integrated by this aperture. As a consequence, the reflection coefficient varies gradually as it approaches the tumour region and its variation becomes maximum when it fully faces the tumour region. The same interpretation holds for the reflection phase images presented next.

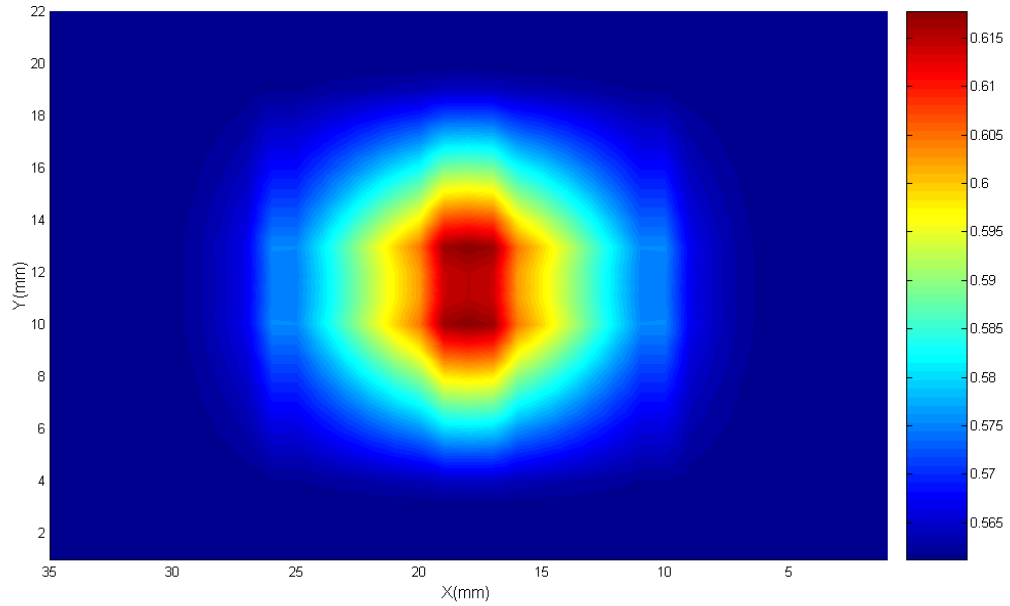


(a)

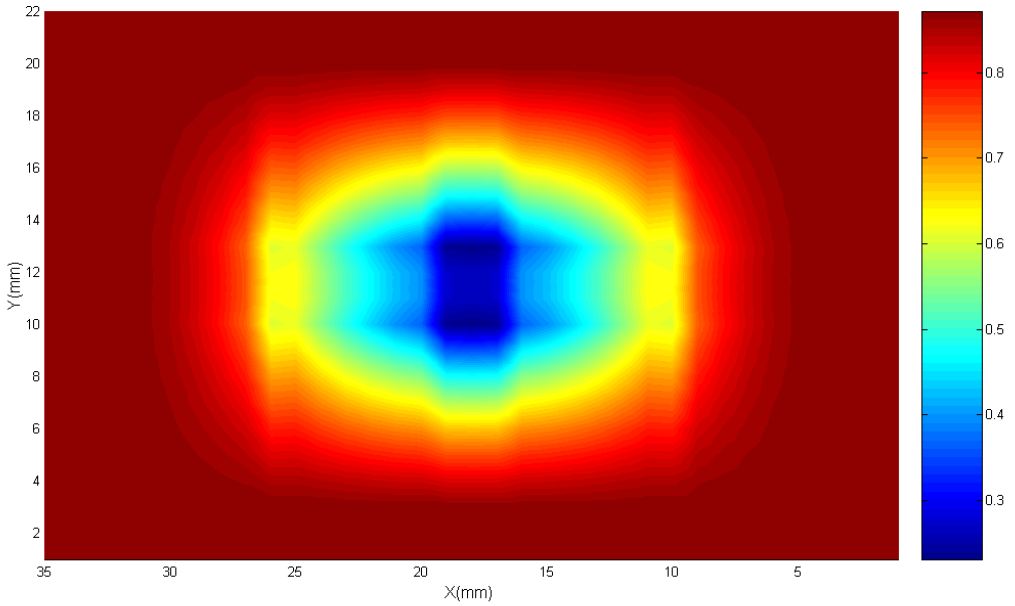


(b)

Figure 3-14: Theoretical 2-D reflection magnitude image of the breast with 6x6x3 mm³ tumour at 5 mm depth: (a) at 10.5 GHz for empty waveguide probe (b) at 3.0 GHz for loaded waveguide probe with dielectric material of $\varepsilon_r = 12.25$.

The theoretical 2-D reflection phase images of the breast with the same scenario of the magnitude image for empty and loaded waveguide sensors are presented in Figures 3-15a and 3-15b respectively. The maximum dynamic range for the phase image is around 1.2° degrees for 5 mm tumour depth when the waveguide sensor is empty. Whereas the maximum dynamic range for the phase image becomes around 15°

degrees for the same tumour depth when the waveguide probe is totally loaded. As a result, the detection sensitivity has been improved when the waveguide sensor is loaded. Again, the physical size in x and y dimensions of the tumour can be estimated from the image itself. Figure 3-16 shows a superimposed theoretical 2-D reflection phase image presented in Figure 3-15b on the breast model in the xy-plane. This superimposed image shows the promise of near-field microwave NIT&E technique for breast cancer detection.

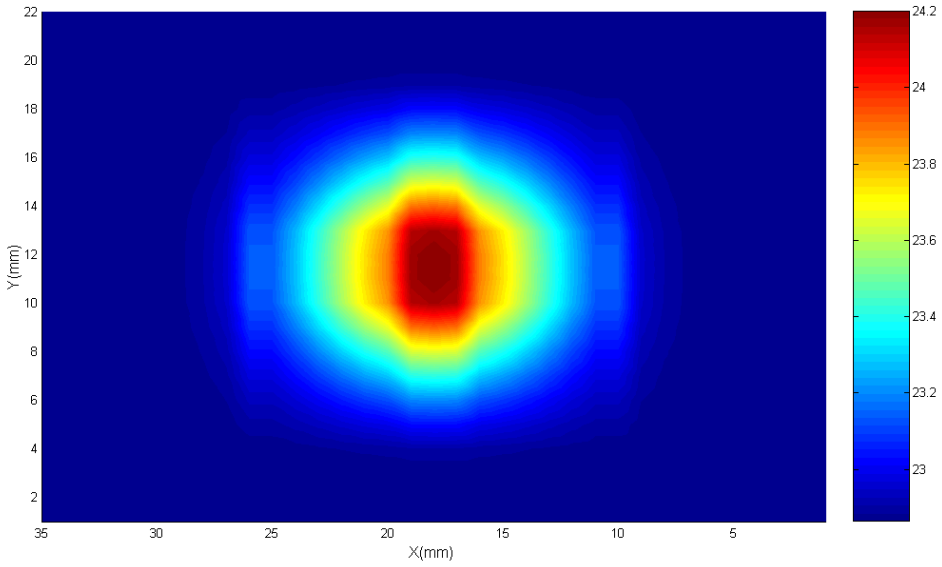


(a)

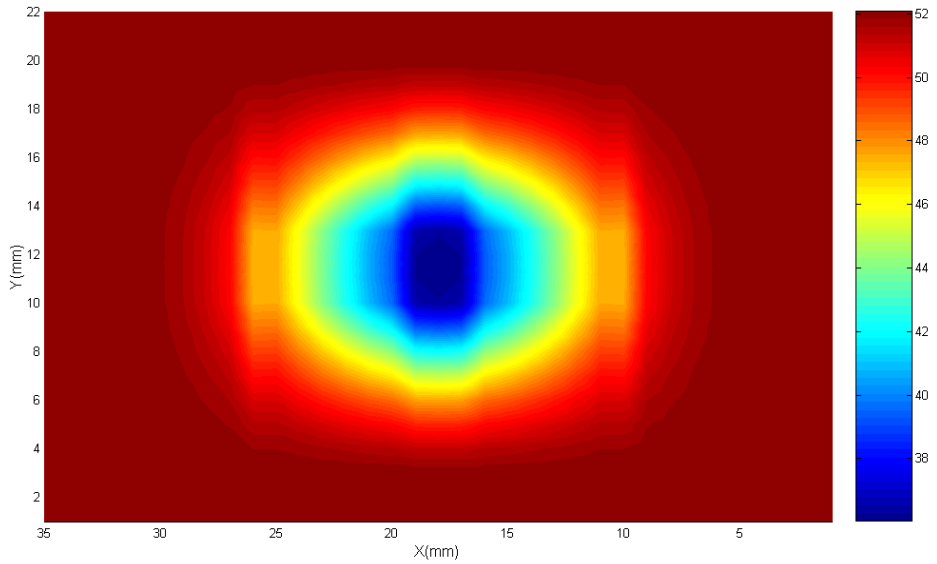


(b)

Figure 3-15: Theoretical 2-D reflection phase image of the breast with 6x6x3 mm³ tumour at 5 mm depth: (a) at 10.5 GHz for empty waveguide probe (b) at 3.0 GHz for loaded waveguide probe with dielectric material of $\varepsilon_r = 12.25$.

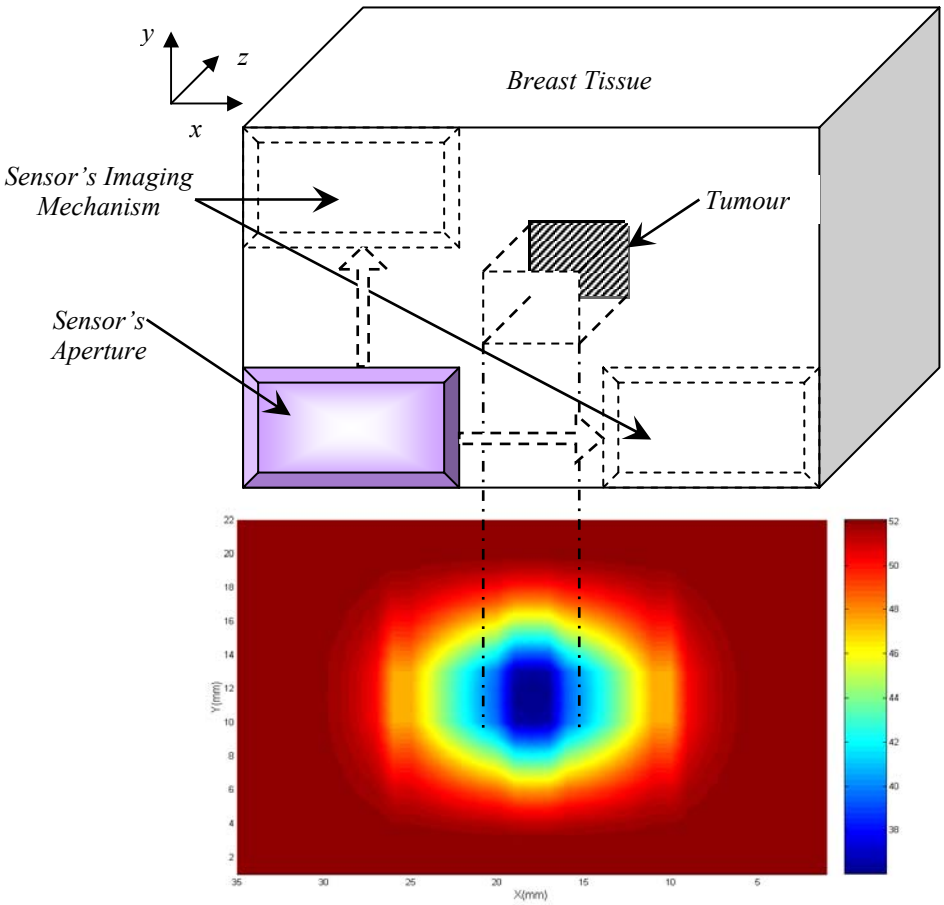


Figure 3-16: Superimposing theoretical 2-D reflection phase image of the breast with 6x6x3 mm³ tumour at 5 mm depth on the breast model.

To show the impact of the waveguide filling on the radiation patterns to a greater extent, Figure 3-17 shows the real power pattern (in dB) (as one dimensional pattern) as a function of x at $y = \frac{b}{2}$ mm and z = tumour depth (tumour interface). The power pattern is calculated for multiple tumour depths at 3.0 GHz and when the waveguide is fully loaded with a dielectric material of relative permittivity $\varepsilon_r$ = 12.25. Whenever the tumour becomes deeper, the power radiated from the sensor to the breast decreases. When the tumour is 5 mm deep, the power at the tumour is maximum. Furthermore, when the microwave probe fully faces the tumour, the coupled power increases. As explained previously, the conductivity of the tumour ($\sigma_i$ = 4 S/m) compared the breast tissue conductivity ($\sigma_2$ = 0.4 S/m) is the main reason behind this effect. The coupling power for all tumour depths increases when the sensor is loaded

compared to empty waveguide. For example, the power for 10 mm tumour depth at x = 2.4 cm was -50 dB for empty waveguide (shown in Figure 3-6). While it becomes -30 dB for the same tumour depth and scanning point when the waveguide is loaded (shown in Figure 3-17).

Figure 3-18 shows this fact in clearer way as it represents the real power pattern as a function of z (direction of propagation) at $x = \frac{a}{2}$ and $y = \frac{b}{2}$ of the breast. The tumour is 5 mm deep. When the microwave sensor is loaded (i.e. operating at 3.0 GHz), the real power coupled into the breast increases compared to the unloaded case. In conclusion, loading the waveguide probe with certain dielectric material confines the radiated power to lie more closely within a spatial extent equivalent to the sensor's aperture further inside the breast and increases the penetration depth. This increases the power coupling to the breast, hence the sensitivity, and enhances the resolution.

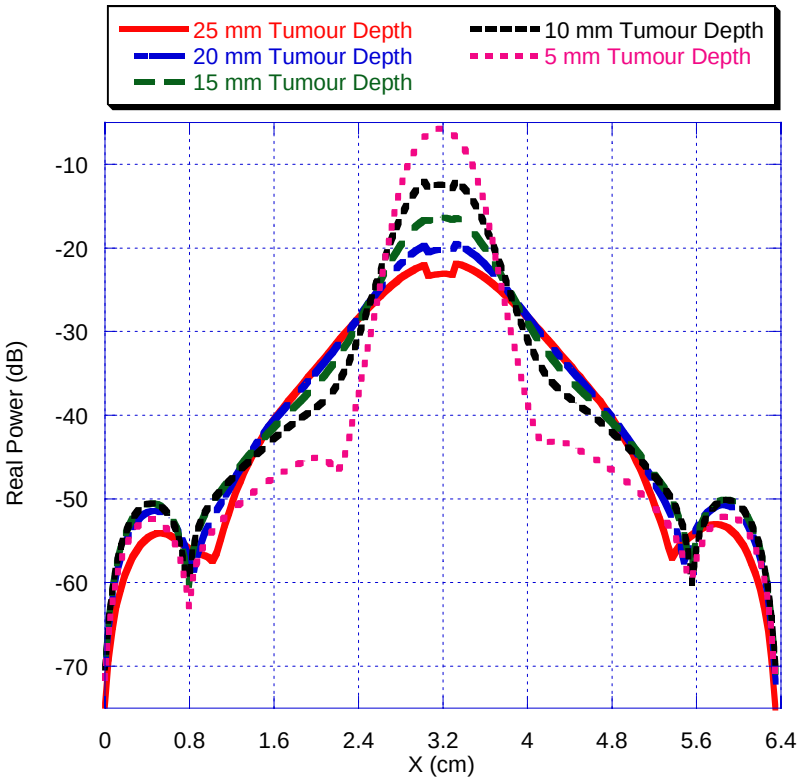


Figure 3-17: Real power as a function of x at y=b/2 and z=tumour depth of the breast with 6x6x3 mm³ tumour operating at 3.0 GHz for different tumour depths.

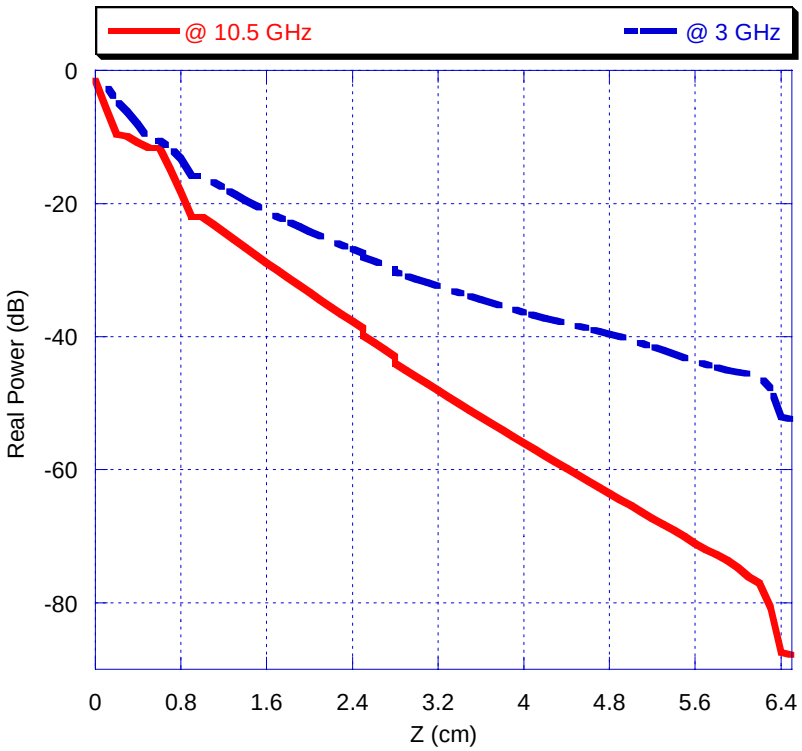


Figure 3-18: Real power as a function of z (direction of propagation) at x=a/2 and y=b/2 of the breast with 6x6x3 mm³ tumour for 5 mm tumour depth.

## *3.4 Influence of Standoff Distance Dielectric Properties on the Radiation Patterns and Reflection Images of Cancerous Breast Tissues*

The dielectric properties of the material between the sensor aperture and the breast, here termed the standoff distance dielectric properties can play an important role in optimising the theoretical image formation process of the cancerous breast. The standoff (SOD), or lift-off, distance is the physical distance between the waveguide sensor aperture and the skin (first layer) of the breast under screening. The standoff distance dielectric properties, if optimised, will confine the radiated power to the sensor's aperture further inside the breast. This tactic can further enhance the image sensitivity and resolution [Sal.07].

Optimising the standoff distance dielectric properties and thickness is a problem in its own right and forms a suitable topic for future detailed research. The magnitude

and the phase differences of the effective reflection coefficient at the sensor's aperture are calculated as a function of standoff distance relative permittivity. The range for the standoff distance relative permittivity is between 30 and 40. The reason behind choosing this range is to minimize the reflections as much as possible between the standoff distance and the skin layer since the relative permittivity, $\varepsilon_{r1}$, of the skin is taken to be 36. Thus, standoff distance relative permittivity in the range of 30-40 is acceptable and is also close to the skin relative permittivity. On the other hand, it is not wise to use a lossy material (i.e. $\varepsilon_r'' \neq 0 \Rightarrow \tan\delta \neq 0$) in the standoff distance since that will kill most of the signal before reaching the skin. Thus, the standoff dielectric is lossless (i.e. $\sigma \approx 0$) as opposed to the skin layer ($\sigma$ = 4 S/m).

Figures 3-19 and 3-20 show the magnitude and the phase differences of the effective reflection coefficient at the sensor's aperture as a function of standoff distance relative permittivity, $\varepsilon_r$, for breast tissue with a tumour 10 mm deep, and with operation at 3.0 GHz. The standoff distance thickness is fixed at 1.0 mm (not thin to show its effect on the radiation patterns and the reflection images; and not thick so not most of the signal will die before reaching the breast. But still an analytical solution has to be derived to obtain the effective and best standoff distance dielectric properties and thickness). The standoff distance relative permittivity, $\varepsilon_r$, varies from 30 to 40. The magnitude difference increases while the phase difference decreases as the standoff distance relative permittivity increases. Choosing one of the local optimum standoff distance relative permittivity will increase the detection sensitivity of the tumour. Thus, optimising both magnitude and phase differences concurrently, $\varepsilon_r$ = 35.3 seems to be the one of the local optimum standoff distance relative permittivities (remember 35.3 is very close to 36, the skin's relative permittivity to minimise reflections). $\varepsilon_r$ = 35.3 is not the global optimum and not the *only* local optimum; all values close to 36 are considered to be local optimum. Also, the magnitude and phase differences of the

effective reflection coefficient for $\varepsilon_r$ = 35.3 and $\varepsilon_r$ = 36 is very close. As illustrated in Figure 3-19, the magnitude difference for $\varepsilon_r$ = 35.3 and $\varepsilon_r$ = 36 is 0.2003 and 0.2005 respectively. Also as shown in Figure 3-20, the phase difference for $\varepsilon_r$ = 35.3 and $\varepsilon_r$ = 36 is 2° and 1.95° respectively.

Again, to obtain the global optimum standoff dielectric properties and thickness is a worthy research topic in near-field microwave non-invasive testing and a full detailed analysis should be carried out later. The solution will be dependent on many factors such as the dielectric and physical properties of the material under inspection (such as the breast or any other biological structure), the frequency of operation, etc.

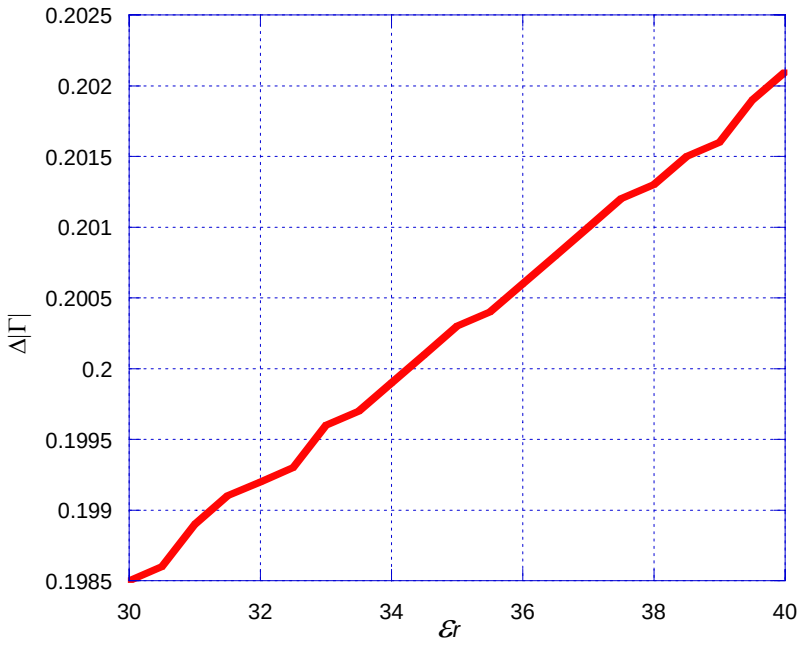


Figure 3-19: The magnitude difference of the effective reflection coefficient at the sensor's aperture as a function of standoff distance relative permittivity for breast tissue with tumour 10 mm deep, and for operation at 3.0 GHz.

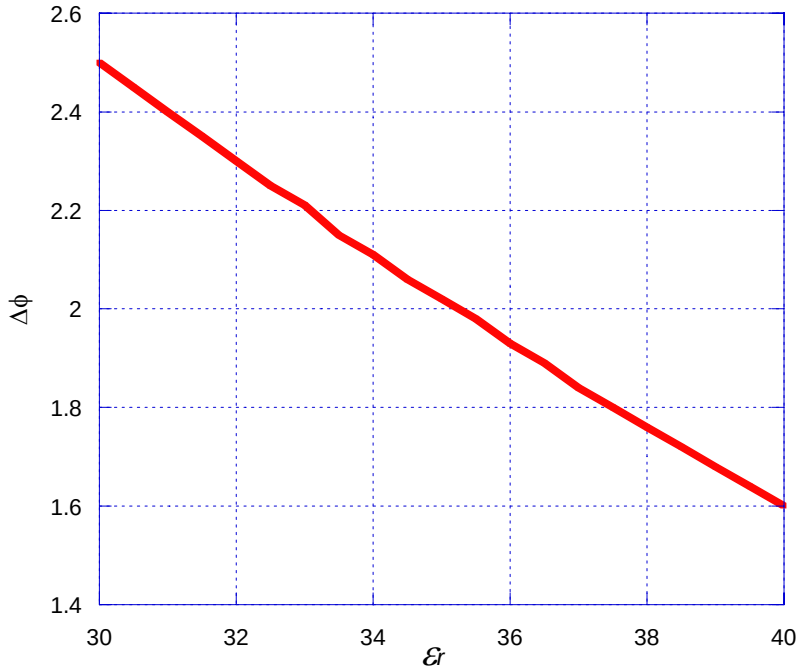


Figure 3-20: The phase difference of the effective reflection coefficient at the sensor's aperture as a function of standoff distance relative permittivity for breast tissue with tumour 10 mm deep, and for operation at 3.0 GHz.

To show the effect of inserting a standoff distance dielectric layer, Figure 3-21 represents the real power pattern as a function of z (direction of propagation) at $x = \frac{a}{2}$ and $y = \frac{b}{2}$ of the breast for 10 mm tumour depth. The real power pattern is displayed for three different arrangements; namely when: (1) the waveguide sensor is empty operating at 10.5 GHz; (2) the waveguide probe is fully loaded with a dielectric material of relative permittivity $\varepsilon_r$ = 12.25 operating at 3.0 GHz; and (3) the waveguide probe is fully loaded with a dielectric material of relative permittivity $\varepsilon_r$ = 12.25 and 1.0 mm standoff distance with relative permittivity $\varepsilon_r$ = 35.3 is introduced operating at 3.0 GHz. When the microwave sensor is loaded (i.e. operating at 3.0 GHz) and the 1.0 mm standoff distance is attached to the sensor's aperture, the real power is coupled more into the breast. Figure 3-22 is a zoomed version of Figure 3-21 where it shows the increment in the coupling power clearly. For example, at z = 10 mm (i.e. tumour presence) the power shifts from -16 dB to -13 dB. Therefore, the real power density

increases when a standoff distance medium with finite dimensions and known relative permittivity is introduced at the sensor's aperture.

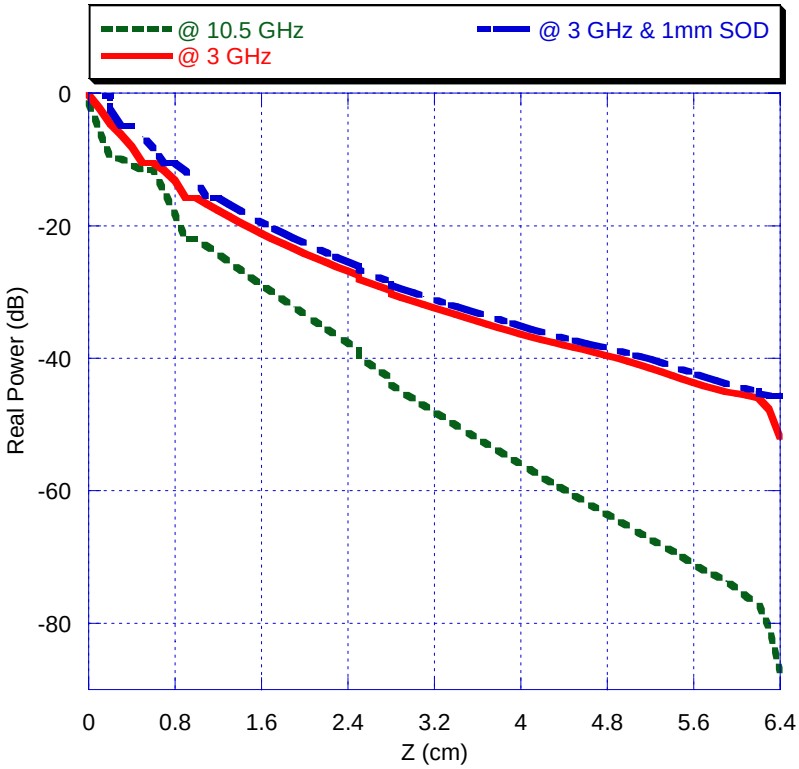


Figure 3-21: Real power as a function of z (direction of propagation) at x=a/2 and y=b/2 of the breast with 6x6x3 mm³ tumour and 5 mm deep.

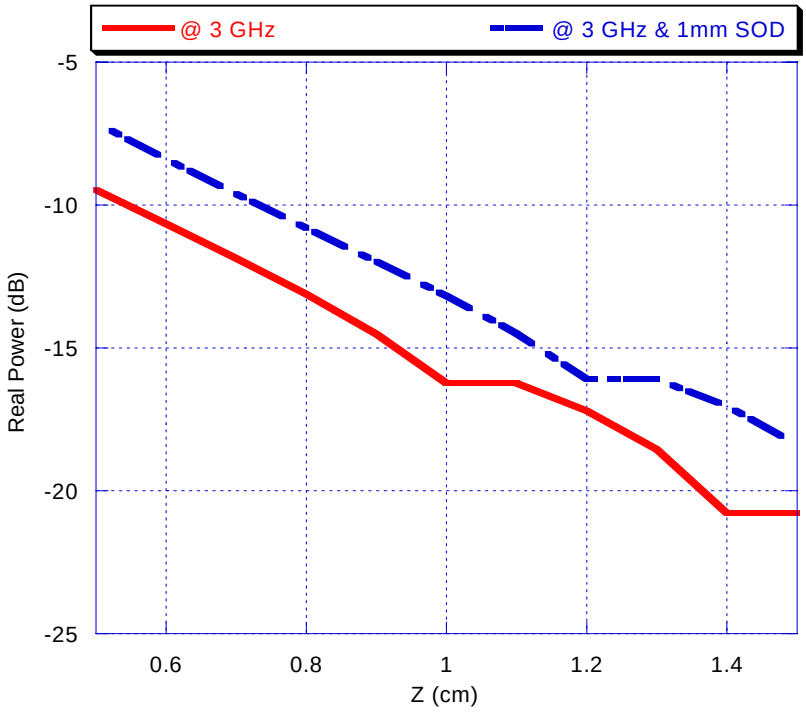


Figure 3-22: Zoomed version of Figure 3-21.

The promise of the theoretical image formation for the optimisation of the tumour detection process, by varying the standoff distance dielectric layer is demonstrated next. Magnitude and phase reflection images of the breast model are produced with and without the standoff distance dielectric layer. The waveguide probe is fully loaded. The tumour with 6x6x3 $mm^3$ dimensions is located at z = 10 mm. The frequency of operation is 3.0 GHz. Figures 3-23 and 3-24 show the 2-D reflection magnitude images with and without the standoff distance dielectric layer, respectively. The maximum difference in the magnitude image when there is no standoff dielectric is 0.16. However, when the 1.0 mm standoff dielectric is present, the maximum difference in the magnitude image becomes 0.2. Thus the detection sensitivity becomes 1.25 times better when the standoff dielectric is present.

Then the 2-D reflection phase images for the standoff distance dielectric layer absence and presence are illustrated in Figures 3-25 and 3-26 respectively. The dynamic range of the phase image when there is no standoff dielectric is 0.5° degrees. But when the 1.0 mm standoff dielectric is introduced, the dynamic range of the phase image becomes 2° degrees. As a result, the detection sensitivity becomes four times better.

Such numerical approaches to optimisation are most useful, but can be very time consuming and it is difficult with numerical techniques to perform a full parameter search. Thus, obtaining an analytical solution for the effective dielectric properties of the standoff distance medium, which will maximize the difference in the magnitude and phase of the effective reflection coefficient and will focus the radiated power from the probe's aperture deep inside the breast, should be considered and studied in future.

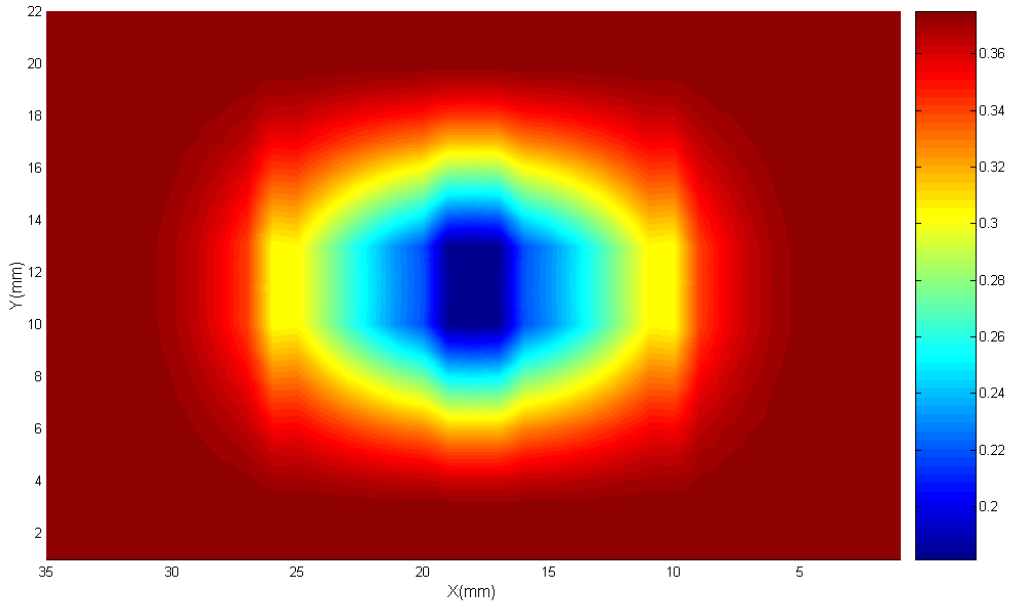


Figure 3-23: Magnitude image of the breast with 6x6x3 mm³ tumour at 10 mm depth at 3.0 GHz in contact fashion.

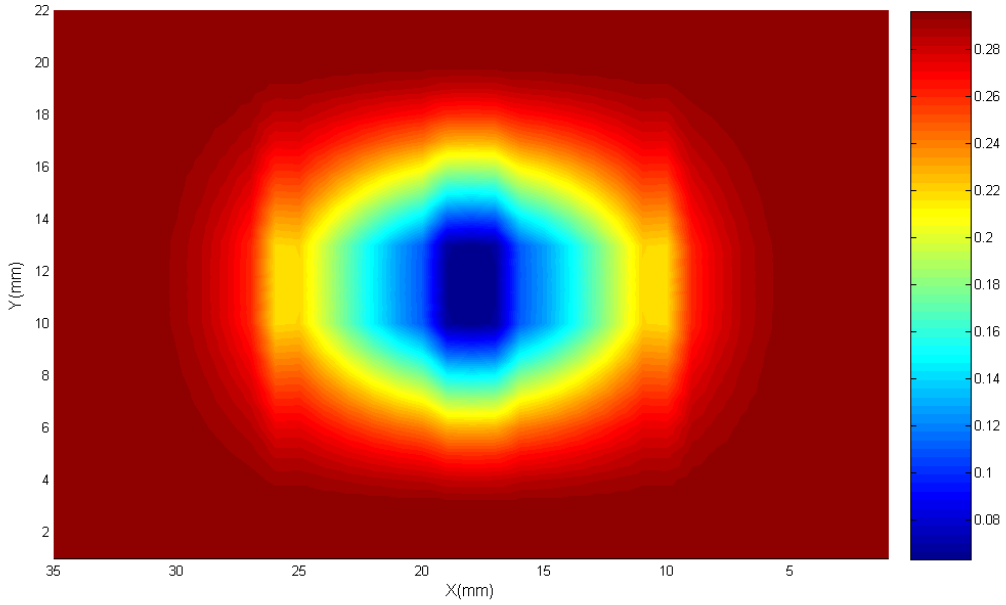


Figure 3-24: Magnitude image of the breast with 6x6x3 mm³ tumour at 10 mm depth at 3.0 GHz with 1 mm dielectric standoff distance of relative permittivity $\varepsilon_r = 35.3$.

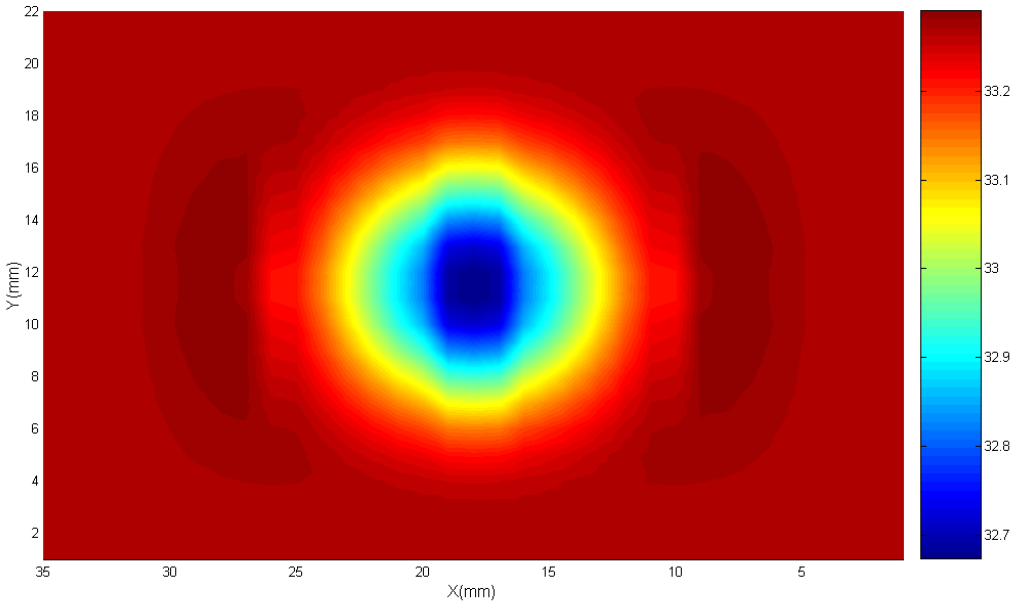


Figure 3-25: Phase image of the breast with 6x6x3 mm³ tumour at 10 mm depth at 3.0 GHz in contact fashion.

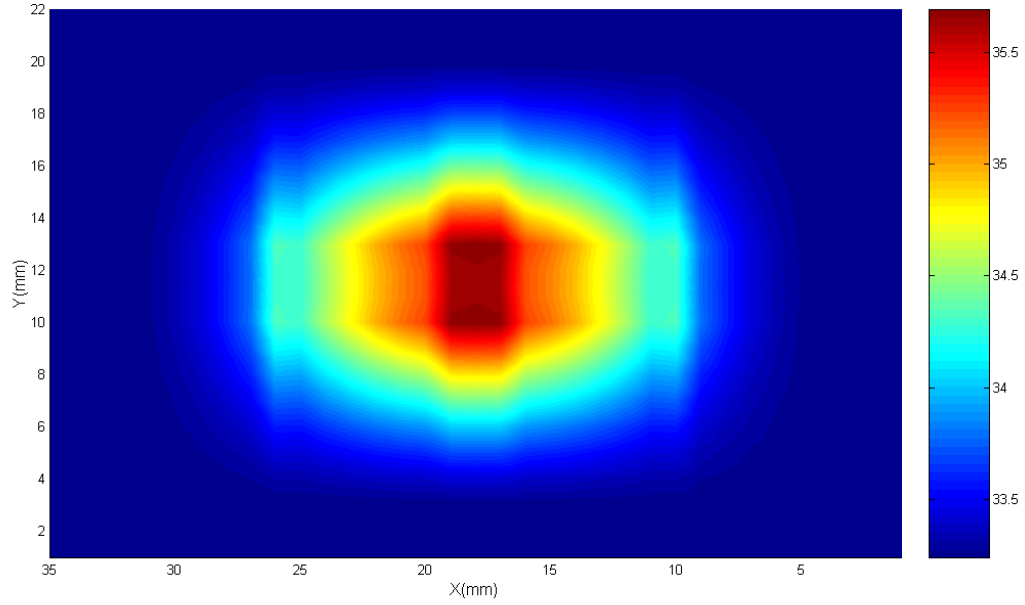


Figure 3-26: Phase image of the breast with 6x6x3 mm³ tumour at 10 mm depth at 3.0 GHz with 1 mm dielectric standoff distance of relative permittivity $\varepsilon_r$ = 35.3.

## *3.5 Summary and Remarks*

In this chapter, extensive theoretical simulation analyses have been conducted to reveal the aptitude of near-field microwave NIT&E technique for breast cancer detection. Radiation patterns (normalized electric field, real power pattern and imaginary power pattern) are vital to understand the imaging mechanism of the rectangular waveguide probe. The analysis of these patterns allows us to interpret the captured images and assess the presence of a tumour within the breast tissue. Theoretical reflection images (magnitude and phase images) of cancerous breast have shown that detection of tumour presence is feasible. Essentially, forming the images theoretically constitute a powerful tool to optimise the resolution and sensitivity of the acquired images. Being able to form these images theoretically will aid in solving the inverse problem in the future.

The study includes investigating the influences of frequency of operation, loading of the waveguide sensor and the dielectric properties of the standoff distance medium. Appealing optimisation tactics, namely the waveguide filling and the standoff distance dielectric, have been adopted and their effects on the radiation patterns and theoretical images have been illustrated. The detection sensitivity has been improved, the penetration depth increases (lower frequency of operation), the spatial resolution has been enhanced and the tumour presence within the breast can easily be detected. The simulations demonstrate and prove the practical feasibility of the developed image formation model.

Obtaining an analytical solution to the global optimum standoff dielectric properties and thickness must be taken into consideration in future as a research topic in near-field microwave non-invasive testing. Also, calculating the effective dielectric properties of heterogeneous materials and structures such as the breast is a classical problem in microwave non-destructive non-invasive testing and an analytical solution

should be investigated taking into considerations many parameters such as the volume fraction, dielectric properties and physical dimensions of each constituent of the structure to obtain an explicit form of the effective dielectric constant that can represent the whole structure.

According to the Institutional Review Board (IRB) rules and regulations, experimental investigation can't be performed on real breast tissues without certain rules and safety precautions and regulations being in place[1]. To avoid such difficulties microwave researchers in the field commonly utilize breast phantoms [Li.03] [Li.04].

Thus, in chapter 4, a breast phantom that mimics the properties of the real breast is developed and used for experimental investigation. An experimental setup for uncalibrated measurements is presented and its operation is discussed. Several experimental results are shown and relative information, such as tumour existence, about the cancerous cell within the breast is obtained.

[1]The Institutional Review Board (Independent Ethics Committee / Research Ethics Board) of *Institutional Review Board Services* is constituted and operated according to the rules and regulations as detailed in the Canadian Food & Drug Regulations, Division 5 (Clinical Trials), ICH GCP E6, the Canadian TCPS, U.S. CFR Title 21 Parts 50 and 56, and CFR Title 45 Part 46. ICH GCP E6 1.31: "Institutional Review Board (IRB): An independent body constituted of medical, scientific, and non-scientific members whose responsibility is to ensure the protection of the rights, safety, and well-being of human subjects involved in a trial".

# *CHAPTER 4*

## *Uncalibrated Experimental Measurements for Breast Cancer Detection*

### *4.1 Breast Phantom*

After understanding the interaction between the microwave sensor and the breast structure under inspection and conducting extensive simulations, it is also important to study breast cancer detection with near-field microwave testing experimentally. This will aid in verifying the potential of near-field microwave non-invasive testing and evaluation (NIT&E) techniques as a successful candidate for breast cancer detection. As mentioned at the end of chapter 3, a breast phantom instead of real breast will be used to conduct the experimental investigation because of the Institutional Review Board (IRB) rules and regulations and for the reason that microwave researchers in the field exploit breast phantoms [Li.03] [Li.04].

Two types of microwave measurements will be conducted, namely calibrated and uncalibrated. This current chapter deals with the uncalibrated measurements, while chapter 5 presents the results obtained when using calibrated microwave measurement systems. The objective from conducting uncalibrated measurements is to qualitatively show the promise of NIT&E techniques practically and to obtain relative information (such as tumour existence or not) about the properties of a tumour within the breast phantom. Calibrated measurements, on the other hand, show that more detailed information may be attained, and are a most useful vehicle for validation of the simulation results obtained from our theoretical investigations. The microwave

measurement systems used consist of a microwave frequency generator, a probe or a sensor, a microwave component to separate the incident signal from the reflected signal and an analyzer to analyze the output signal obtained by the sensor.

Both breast and tumour phantoms that closely imitate the dielectric properties contrast of the real breast model (presented in section 1.11 of this thesis) were developed as part of the current work. The constituents of the phantom were chosen based on the dielectric contrast ratio between the tissue simulant and the tumour simulant. The breast tissue phantom includes a thin layer of skin simulant, normal breast tissue simulant and malignant breast tissue simulant that closely emulate the dielectric properties contrast observed in real breast tissue at microwave frequencies.

The simple breast phantom used here is shown in Figure 4-1 and consists of a rectangular shaped container of size 20 cm x 20 cm x 10 cm filled with a normal breast tissue simulant. The breast-tissue-mimicking material is homogeneous corresponding to an average of the fat, veins, blood and glandular parenchyma. The skin simulant is the container itself and is represented by a 4-mm layer of plexiglass. Its relative dielectric constant ($\varepsilon_r$) is 2.59 and the skin depth ($\delta$) is 0.007 m for a frequency range from 8.2 GHz to 12.4 GHz [Bak.93]. Soybean oil is used as the normal breast tissue simulant since it is an economical and harmless liquid. Its relative dielectric constant ($\varepsilon_r$) is 2.6 and its conductivity ($\sigma$) is 0.05 S/m at 6 GHz. The artificial tumour is represented by a diacetin solution poured into a 2 cm by 3 cm balloon. Its relative dielectric constant ($\varepsilon_r$) is 8.7 and its conductivity ($\sigma$) is 1.9 S/m at 6 GHz [Li.03] [Li.04].

There is a relative permittivity contrast ratio of 3.3:1 between the malignant and normal tissue simulants. Recalling from chapter 1 that the breast model is composed of the following: layer 1: skin; $\varepsilon_{r1} = 36$ and $\sigma_1 = 4$ S/m, thickness = 2 mm. Layer 2: breast tissue; $\varepsilon_{r2} = 9$ and $\sigma_2 = 0.4$ S/m, thickness = 60 mm. Layer 3: skin; $\varepsilon_{r3} = 36$ and $\sigma_3 = 4$

S/m, thickness = 2 mm and a tumour ($\varepsilon_{ri}$ =50 and $\sigma_i$ = 4 S/m) with dimensions of 6 mm x 6 mm x 3 mm (these values are based on literature review where they represent real measured tissue data). Thus the ratio of the real breast model to tumour is around 5.5:1. The relative permittivities as well as the conductivities of the model are higher in values than the phantom for all breast constituents. For example, the relative permittivity of the tumour model is 5.7 times bigger than the tumour simulant. However, the dielectric contrast of the phantom closely imitates the contrast noticed in the model. Furthermore, other issues such as accessibility, cost, and toxicity are taken into account in selecting the phantom materials. The phantom ratio is even less than the actual ratio of breast tissue to tumour. The configuration when the dielectric contrast is reduced from 5.5:1 to 3.3:1 is more challenging for tumour detection especially when experimental results are sought. Thus this will show the promise of near-field microwave NIT&E techniques.

Recalling from chapter 3, the optimum frequency for the real breast model was 3.0 GHz and that was when the waveguide sensor was fully loaded with dielectric material of relative permittivity $\varepsilon_r$ = 12.25. Due to this loading, the frequency of operation dropped to 3.0 GHz. For the experimental investigation, the waveguide probe is not loaded and the optimum frequency is between 8.2 GHz and 12.4 GHz. This is because breast phantom is used instead of real breast and since the dielectric properties contrast ratio between tissue and tumour is the important factor. Consequently, the frequency of operation is scaled and there is no need for loading the waveguide experimentally. Loading the waveguide probe experimentally will be essential when measurements on real breasts are conducted because even if the contrast is obvious, still the actual absolute dielectric contrast of the material under inspection will have an impact on the reflection coefficient measurement. Remember from the analytical solution of the reflection coefficient developed in section 2.3 of this thesis that the reflection coefficient is dependent on the material dielectric properties.

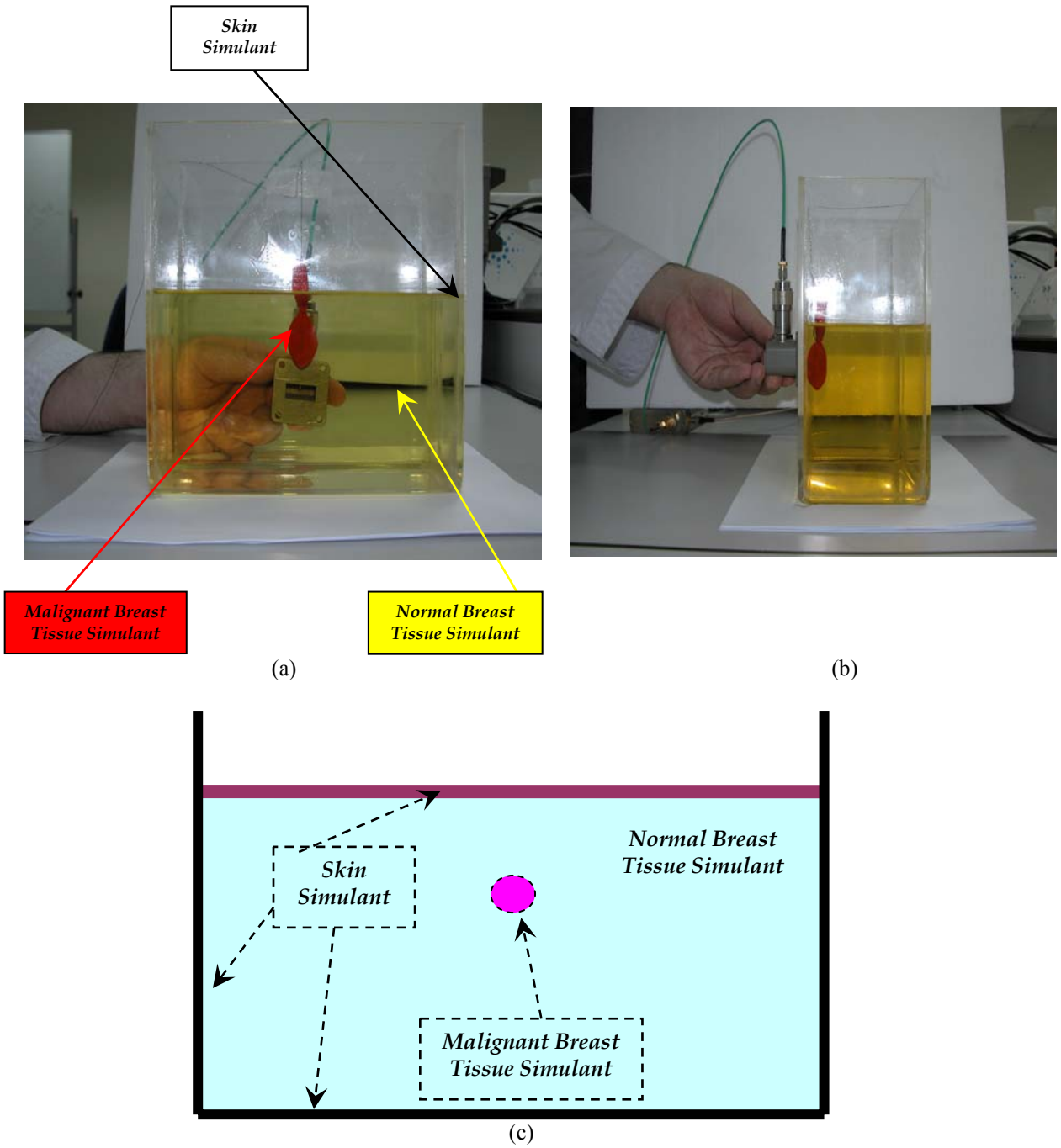


Figure 4-1: (a) Back view (b) side view (c) schematic diagram of the cancerous breast phantom under inspection.

## *4.2 Uncalibrated Microwave Measurement Setup*

Microwave researchers have focused on developing novel inspection techniques and increasing their realm of applications. One such technique involves using various microwave probes or sensors whose near-field (rather than far-field) properties form the

basis of the inspection process. In near-field, the field properties vary nonlinearly as functions of distance from the sensor (standoff distance). Three basic regions can be identified that surround a microwave radiator or source [Bal.97]. The region closest to the radiator is known as the reactive near-field region in which reactive (quasi-static) fields predominate. The next region further away from the radiator is known as the radiating near-field region in which both radiating and reactive fields are present, but here the radiating fields begin to predominate. The third region (furthest away from the radiator) is known as the far-field region in which only radiating (travelling-wave) fields exist. At great enough distances from the source the fields in this region have planar phase fronts, and thus they are called uniform plane waves. They are also referred to as transverse electromagnetic (TEM) waves since the electric- and magnetic-field vectors are orthogonal to each other and to the direction of propagation.

It will be helpful to compare far-field and near-field microwave imaging techniques in a little more detail. Far-field techniques are typically characterized by the following features:

1) The material under inspection is placed in the far-field region of the antenna.
2) The antenna and the material are not in physical contact.
3) The number of suitable antenna designs is limited because the antenna should be an efficient radiator/receiver.
4) The mathematical models that describe the plane waves' interactions with the material under inspection are relatively simple and easy to evaluate.
5) There is a limitation in the number of controllable measurement parameters available for optimizing the inspection process.
6) There is a low sensitivity to the structural parameters of the material under inspection such as thickness variations in complex stratified dielectric structures.
7) The spatial (lateral) resolution is relatively coarse and mainly determined by the size of the operating wavelength (and the signal-processing techniques applied).

On the other hand, the characteristics of near-field techniques are typically exemplified by the following features:

1) The material under inspection is located in the near-field region of a probe or sensor.
2) The sensor and the material under inspection may or may not be in contact based on the standoff distance.
3) A wide variety of useful near-field probes are available, for example:
    - open-ended rectangular and circular waveguides,
    - open-ended coaxial lines,
    - short monopole antennas,
    - microstrip patches, and
    - open-cavity resonators.
4) The mathematical models that describe the interaction of near fields with material media are relatively complex and generally require extensive computer resources for their evaluation.
5) Further measurement parameters are accessible for optimizing the inspection process, for example, the standoff distance properties and the probe filling (as discussed in chapter 3).
6) A high level of measurement sensitivity to small dissimilarities in dielectric or geometrical parameters of the material under inspection can be obtained because the probe fields are more concentrated.
7) The spatial (lateral) resolution can be quite high, since in the near-field region this resolution is primarily determined by the physical dimensions of the probe and not by the operating wavelength.
8) Relative phase shifts in the reflection or transmission coefficients are more readily measured than in the far-field case.

9) A near-field microwave imaging system is usually simpler, and more compact and portable than a far-field system [Bah.02] [Sal.03b].

The experimental arrangement used for the uncalibrated near-field measurements is shown in Figure 4-2. It consists of:

(1) HP/Agilent 83752A Synthesized Microwave Sweeper (microwave source),

(2) HP/Agilent 8757A Scalar Network Analyzer (SNA),

(3) HP/Agilent 85027B Directional Bridge,

(4) Coaxial Cables and

(5) HP/X281B X-band Open-Ended Rectangular Waveguide Probe.

(6) The breast phantom

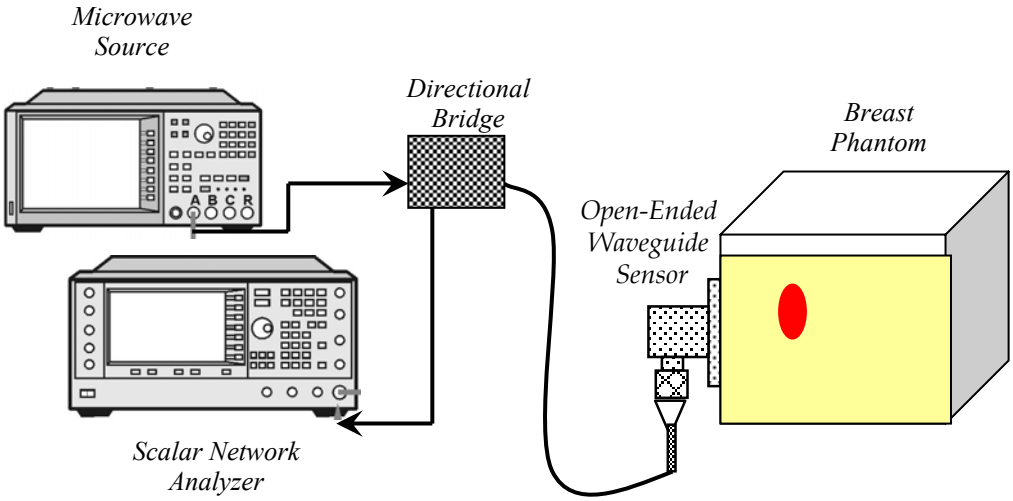


(a)

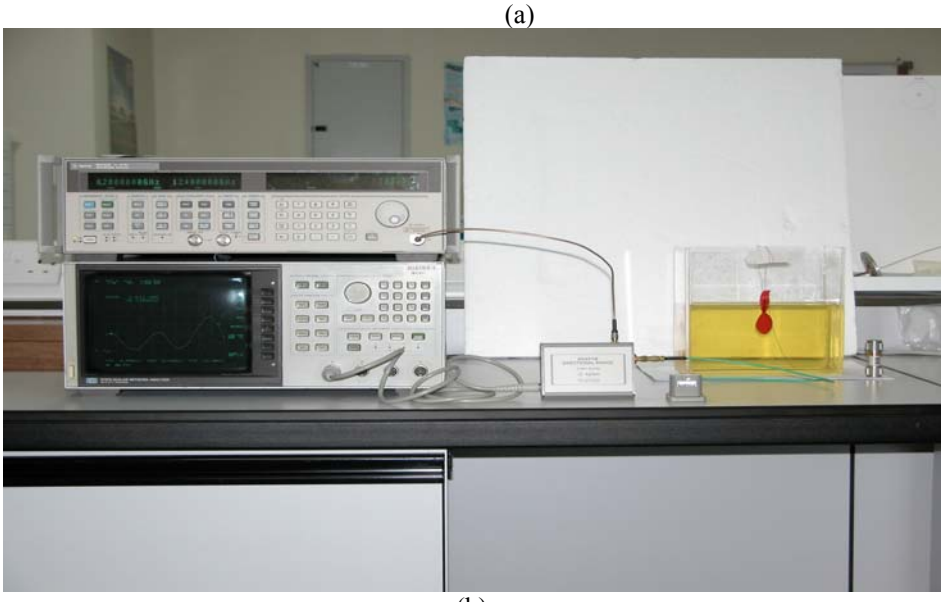

(b)

Figure 4-2: Near-field microwave uncalibrated measurement system: (a) schematic diagram (b) real system.

**1- HP/Agilent 83752A Synthesized Microwave Sweeper:**

The microwave sweeper, shown in Figure 4-3, is used for swept test and/or scalar applications. It has excellent accuracy and stability while maintaining the speed of an analogue source. The typical accuracy is ±10mV where the voltage is proportional to the output frequency [Agi.96b]. This device has fully synthesized continuous wave (CW), and different sweep modes that are available in broadband and narrowband operation. Furthermore, the power of the output signal is controlled in units of dBm. As for this research, this device is employed to sweep or generate a range of frequencies at X-band, from 8.2 GHz to 12.4 GHz. The output of the sweeper is fed to the HP 85027 directional bridge [Agi.96a].

Figure 4-3: HP/Agilent 83752A Synthesized Microwave Sweeper.

**2- HP/Agilent 8757A Scalar Network Analyzer (SNA):**

This device, shown in Figure 4-4, is a microprocessor-based receiver that is capable of making scalar magnitude only reflection and/or transmission measurements over a frequency range that is determined by the external detectors used. The 8757A SNA is capable of performing scalar measurements over the frequency range of 10MHz to 40GHz. Furthermore, and in terms of power; it is capable of measuring over the range from +10 dBm to -50 dBm. The SNA will provide us with the magnitude of the reflection coefficient only (scalar measurement) and for calibrated measurements; magnitude and phase of the reflection coefficient are of interest. Thus, the SNA will be utilized to conduct uncalibrated measurements and a different experimental

measurement setup will be used for the calibrated measurements, as discussed in chapter 5.

The SNA is used in order to measure the reflection coefficient that is obtained from the HP/X281B X-band open-ended rectangular waveguide probe. However, the reflection coefficient is not obtained directly using the SNA. That is, when measuring, the standing wave ratio (SWR) is obtained and is used to calculate the reflection coefficient from equation (4.1) shown later.

Figure 4-4: HP/Agilent 8757A Scalar Network Analyzer.

### 3- HP/Agilent 85027B Directional Bridge:

The directional bridge, shown in Figure 4-5, is designed to detect radio frequency (RF) or microwave signals, which are either 27.8 kHz square wave, modulated or unmodulated signals. In both modes, the output to the analyzer is a 27.8 kHz square wave signal that is used by the SNA to interpret and display. In this research the AC mode was used and the bridge demodulates the signal using envelope detection technique, producing a 27.8 kHz square signal whose peak-to-peak voltage corresponds to the magnitude of the signal at the bridge test port. The advantage of this technique is that a low noise signal is produced since the modulated signal is detected by the bridge [Agi.85].


Figure 4-5: HP/Agilent 85027B Directional Bridge.

**4- HP/X281B X-band Open-Ended Rectangular Waveguide Probe:**

The HP/X281B X-band open-ended rectangular waveguide, seen in Figure 4-1, is a hollow tube with rectangular cross section. Waveguides have a cut-off frequency below which no signal can propagate. Therefore, a waveguide functions as a high pass filter. The mode with the lowest cut-off frequency is known as the dominant mode. This is the mode at which waveguides operate when transferring a microwave signal from one point to another. Additionally, to avoid the propagation of higher-order modes (i.e., other than the dominant mode) an upper frequency bound is associated with a waveguide. This upper bound is at the cut-off frequency of the first higher-order mode that can be generated. Waveguides are also dispersive which means the phase velocity becomes a frequency dependent parameter. Therefore, to avoid excessive dispersion, the operating frequency band of a waveguide is usually 1.25 times the cut-off frequency of the dominant mode and extends to 0.95 of the cut-off frequency of the first higher-order mode. For this research, an X-band rectangular waveguide is utilized and it has a cut-off frequency of 6.557 GHz and an operating frequency range of 8.2 - 12.4 GHz. At this frequency band the waveguide cross-section (inside dimensions) is 2.286 cm by 1.016 cm [Poz.05].

As for the cables and connections, the scalar network analyzer is connected to the sweeper using a special cabling setup as shown in Figure 4-6. In addition, the directional bridge is connected to the sweeper and the network analyzer as shown in the same figure.

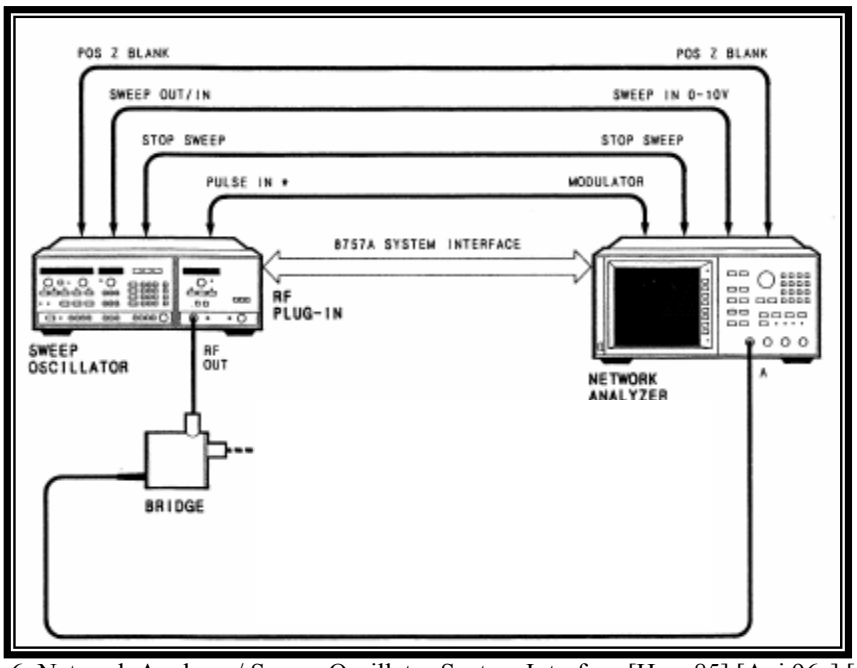


Figure 4-6: Network Analyzer/ Sweep Oscillator System Interface [Hew.85] [Agi.96a] [Agi.00].

Before performing any type of measurements, the SNA was calibrated by attaching two types of load to the directional bridge, the short and open loads. The calibration process however is incomplete because two loads (unavailable at the time of carrying out the measurements) are missing, namely fixed load and sliding load as shown in Figure 4-7. Thus, the experimental results presented in this chapter are not exactly calibrated, but they still allow a qualitative assessment of the tumour presence within the breast tissue phantom to be performed, which is the aim here.

As for the short load, which represents a short circuit, the entire transmitted signal via the terminal is reflected to yield the maximum output of the system. On the other hand, when an open load[1] (in fact it is a matched load) is connected, the transmitted signal is completely absorbed having no reflection at all to give out the system's minimum output. The two types of loads that are used with the bridge are shown in Figure 4-8.

[1] Open load for the calibration process for the HP/Agilent 8757A Scalar Network Analyzer means 'matched load' in terms of transmission line theory. Thus, the open load shown in Figure 4-8 is in fact a matched load where the whole wave is transmitted and there is no reflection. This makes sense since calibration is the process of measuring known standards to characterize a network analyzer's systematic (repeatable) errors and usually these standard loads must give minimum (represented by matched load) and maximum (represented by short load) outputs to cover the whole range of the output value.

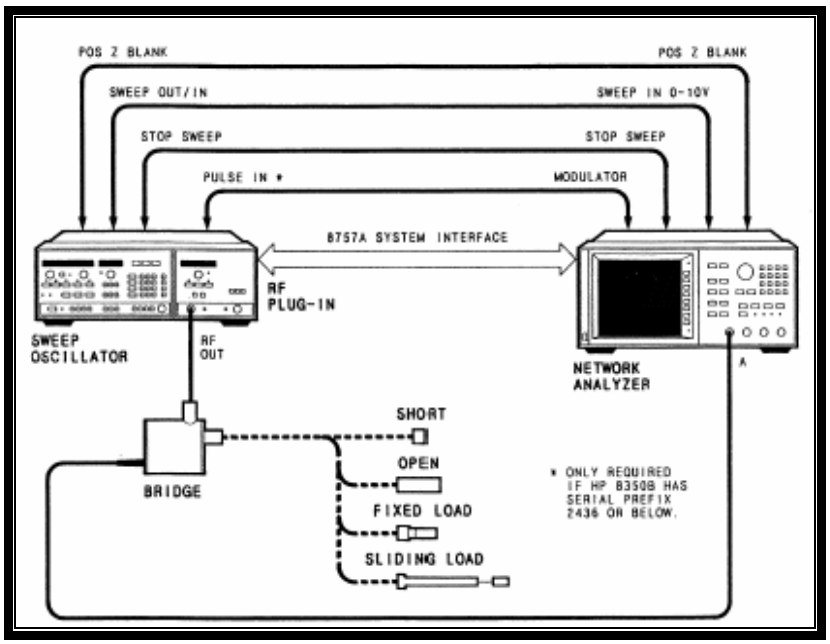


Figure 4-7: System performance test setup [Hew.85] [Agi.96a] [Agi.00].

Figure 4-8: A 3.5 mm open/short load.

After setting the range of frequencies to be swept, an incomplete calibration process was preformed by first pressing the "CAL" button on the SNA and then connecting the open load to the test port and storing the output. Then the short load is connected and the resulting output stored again to have the SNA calibrated but, as explained above, not fully calibrated. Using a coaxial connection, the X-band open-ended rectangular waveguide probe was connected to the test port. To make a measurement; the open-ended rectangular waveguide probe was in contact with the skin simulant (plexiglass) to obtain the SWR at the SNA which is to be used to obtain the magnitude of the reflection coefficient of the malignant and normal tissue simulants.

A microwave oscillator is used to generate a continuous-wave (CW) signal at a given frequency. The directional bridge is placed between the oscillator and the rest of the system to prevent reflections from reaching the oscillator and detuning or damaging it. The signal is then split into test and reference signals. The reference signal becomes

the input signal to the reference channel for the network analyzer. The test signal is fed to the rectangular waveguide sensor from which it radiates and illuminates the breast phantom under inspection. The signal then propagates through the phantom and then reflections are received by the rectangular waveguide sensor and subsequently fed into the test channel of the network analyzer. The network analyzer compares the standing wave ratio of the reflected test signal with those of the reference signal and displays the resulting relative values.

## *4.3 Uncalibrated Experimental Results*

Based on the experimental setup discussed above, different scenarios for experimental measurements have been conducted. The optimum frequency of operation can be determined either using analytical solutions and simulation analysis such as that presented in chapter 3, or it can be determined experimentally as shown here. For near-field frequency optimization measurement, the following procedure is followed:

1. The rectangular waveguide probe is placed over a region away from the tumour region and in contact with the breast phantom. The frequency is then varied within the X-band by an average step of 0.35 GHz while recording the measured output signal or SWR.
2. The waveguide sensor is then placed over the tumour region and the same process in (1) is repeated.
3. From the SWR, the magnitude of the reflection coefficient, |Γ|, can be calculated from the following equation:

$$|\Gamma| = \frac{SWR - 1}{SWR + 1} \tag{4.1}$$

4. The frequency at which the difference between the two reflection coefficients (for no-tumour and tumour regions) is maximum is taken as the optimum frequency for the in-contact measurement.

Figure 4-9 shows the magnitude of the reflection coefficient, $|\Gamma|$, as a function of frequency at X-band for cancerous and normal breast tissue. It is evident from the graph that there is a difference in the magnitude reflection measurements during tumour presence and absence. But at certain frequencies, the difference appears to be more than at others. Figure 4-10 shows the magnitude difference of the reflection coefficient as a function of frequency. From Figure 4-10, 9.5 GHz seems to be the optimum frequency since the maximum magnitude difference is attained at this frequency. The magnitude difference of the reflection coefficient is around 0.1 (full range of $|\Gamma|$ is from 0 to 1) [Sal.07]. There is a harmonic pattern seen in Figures 4-9 and 4-10 and this is because the reflection coefficient is dependent on the standing wave ratio (SWR) and it is known that the SWR has a harmonic attitude. Additionally, there are several practical examples that show this fact about the reflection coefficient [Bak.93] [Qad.96c]. The difference in the magnitude of the reflection coefficient measurement due to tumour presence and absence cannot be considered as uncertainty measurement because of the following:

(1) It is known that the SNA's uncertainty measurement in the reflection coefficient measurement, $\Gamma$, is $\leq 0.01$ and here all the $\Gamma$ values are $> 0.2$.

(2) From Figure 4-9, it is clear that there is a pattern for the reflection coefficient, $\Gamma$, measurement and the difference cannot be due to uncertainty because it varies with frequency.

(3) Also, the peaks and the minimum values of the reflection coefficient measurement, $\Gamma$, for tumour presence and absence are matched and it shows there is a consistency in the measured values.

(4) Figure 4-11 shows the accuracy of the reflection coefficient measurement, $\Gamma$, measurements obtained by the SNA, since when there is no tumour, the difference is almost zero.

(5) The reflection coefficient range is $0 \leq \Gamma \leq 1$ and obtaining a $\Delta\Gamma \leq 0.1$ which is one tenth of the maximum value cannot be due to uncertainty.

But for frequency starting from 8.2 GHz ending to 8.8 GHz, the magnitude difference is around 0.06. Even though this difference is not so large as the magnitude difference at 9.5 GHz, the tumour presence can still be detected. The good feature about this frequency range is that the value of $\Delta\Gamma$ is more consistent than 9.5 GHz. In other words and referring to Figure 4-10, the magnitude difference at 9.5 GHz is so sharp that a slight shift in the frequency results in a large shift in the signal. Whereas, over a frequency range from 8.2 GHz to 8.8 GHz, the magnitude difference is fairly constant. It is also notable that at certain frequencies, specifically at 9.15 GHz, 10.8 GHz, and 12.2 GHz, the rectangular waveguide sensor can't detect the tumour presence. Thus, optimizing the frequency of operation is a crucial issue when a near-field microwave detection system is sought.

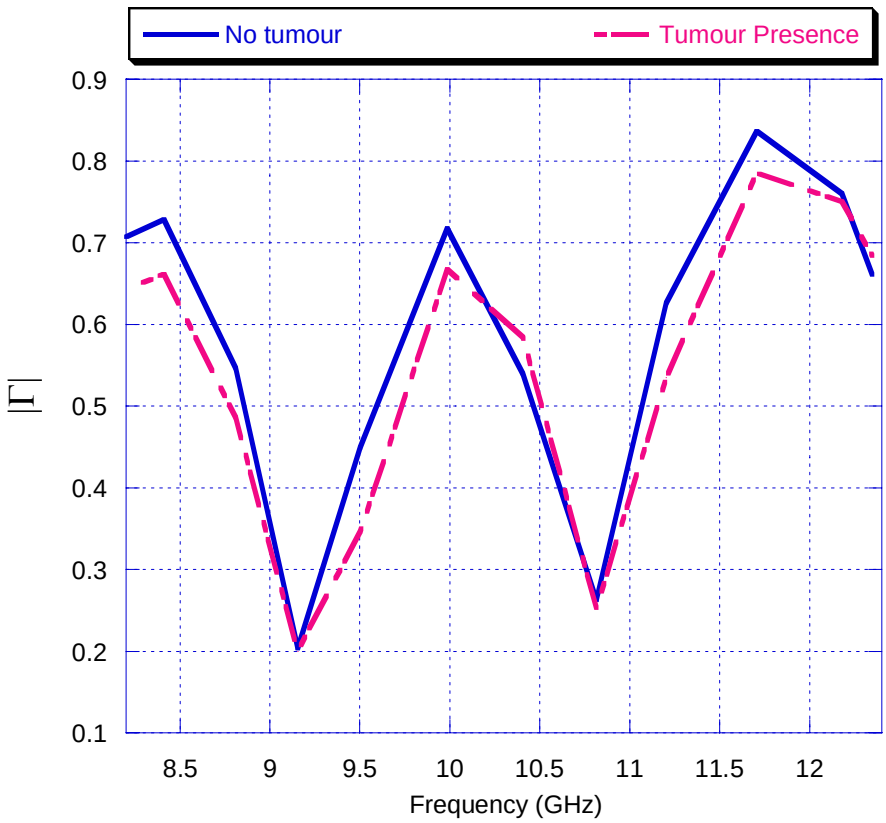


Figure 4-9: The magnitude of the reflection coefficient as a function of frequency at X-band for cancerous and normal breast tissue.

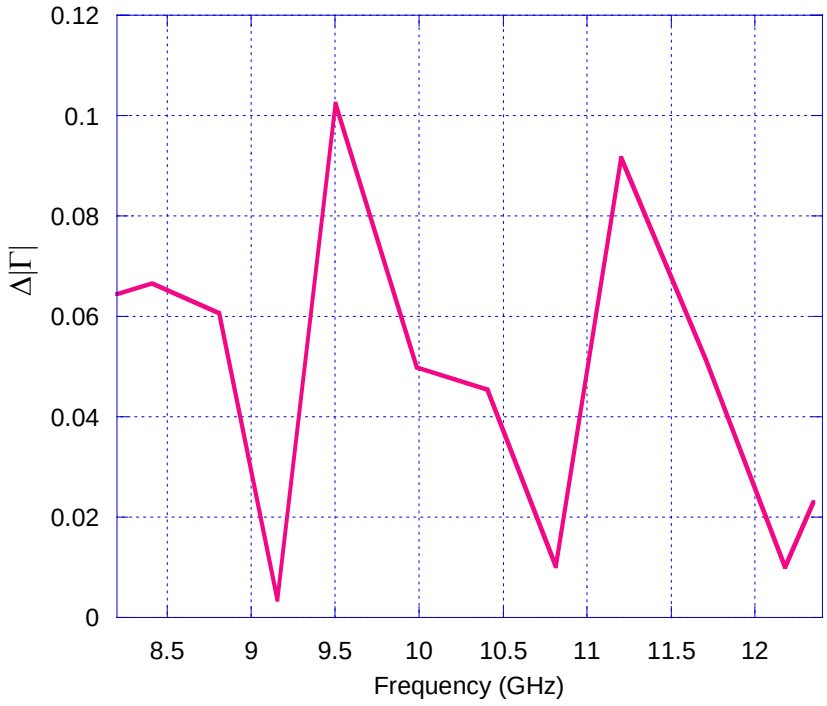


Figure 4-10: The magnitude difference of the reflection coefficient as function of frequency at X-band for cancerous and normal breast tissue.

As mentioned earlier, the artificial tumour has been poured into a 2 cm by 3 cm balloon and it is placed at the centre of the phantom in the xy-plane and directly after

the skin simulant at a certain depth (i.e. at constant z, where z- direction is the direction of wave propagation). Operating at the optimum frequency 9.5 GHz, the sensor was moved horizontally on the surface of skin simulant (plexiglass) and the magnitude difference of the reflection coefficient has been measured as a function of breast phantom x-displacement as shown in Figure 4-11. From the reflection coefficient measurements, the tumour size (width) can be estimated. The estimated tumour width is thus around 2 cm as shown in Figure 4-11. This is because the sensor's aperture is exposed to a certain area of the breast phantom. Once the probe starts moving and recording output signals in 1-D fashion to produce a line scan of the magnitude difference of the reflection coefficient of the phantom under inspection, its aperture acts as a spatial integrator over the exposed area. The probe's aperture will see the tumour region gradually and the reflection coefficient measurements will vary accordingly. Then the maximum difference of the magnitude of the reflection coefficient will occur when the sensor's aperture fully face the tumour region. This is clearly observed in Figure 4-11. Another remark is that the magnitude difference of the reflection coefficient is almost zero when the probe scans from 2 cm to 8 cm and from 12 cm to 18 cm. This is because of the homogeneity of the breast phantom simulants used.

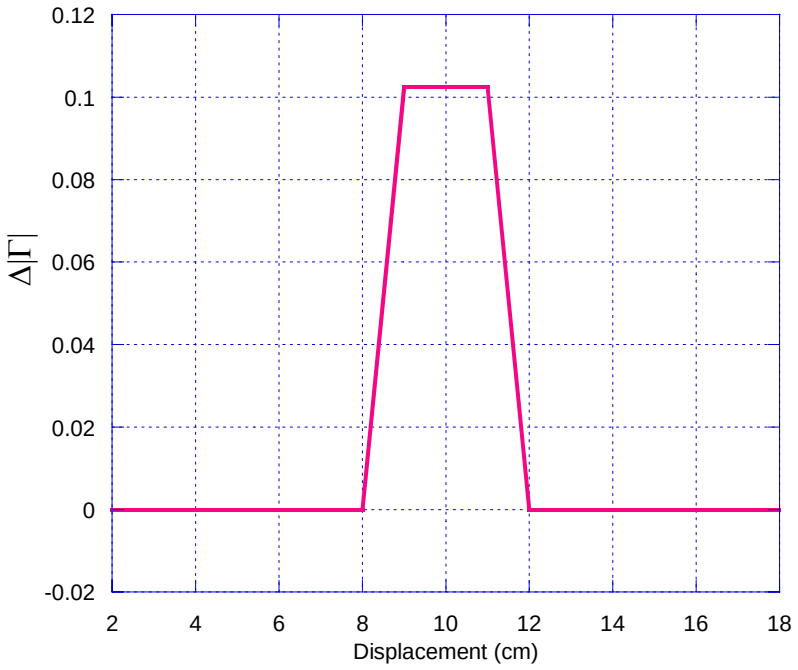


Figure 4-11: The magnitude difference of the reflection coefficient at 9.5 GHz (optimum frequency) as a function of the breast x-position for cancerous and normal breast tissue.

Different tumour depths can influence the reflection coefficient at the rectangular waveguide aperture. This is because the breast phantom is composed of layers with different thicknesses and dielectric properties (including tumour simulant). Thus when microwave signal penetrates the breast phantom, multiple internal reflections occur due to the mismatch of the dielectric properties of the different layers of the phantom. Varying the tumour position will change the multiple internal reflections and hence will alter the effective reflection coefficient at the rectangular waveguide probe's aperture.

Figure 4-12 shows the magnitude difference of the reflection coefficient at X-band for two tumour locations, namely at 0.4 cm and at 2.4 cm away from the sensor's aperture. It is obvious from the graph that when the tumour is 2.4 cm away from the probe, the magnitude difference of the reflection coefficient is greater than when the tumour is 0.4 cm away. This is because the fields propagating from the microwave probe interact nonlinearly with the tumour and the whole phantom under inspection. There are several practical examples which show that the reflection coefficient is not inversely proportional to the defect (inclusion) location within the material under

inspection, i.e. if the defect location becomes close to the probe, then the difference in the reflection coefficient does not necessarily becomes higher [Gra.97]. The relation between the tumour depth and the reflection coefficient is not linear and simple; instead, simulation analysis and experimental investigation have to be conducted in order to obtain the maximum difference in the magnitude of the reflection coefficient. So, even if the tumour is located deep inside the breast, it can be detected when the frequency of operation is optimized.

For the case of Figure 4-12, the frequency of 12.3 GHz appears to be the optimum frequency for tumour detection. Indeed, operation over a range from 11.3 GHz to 12.3 GHz seems to be appropriate, yielding a $\Delta\Gamma \geq 0.15$ over this whole range.

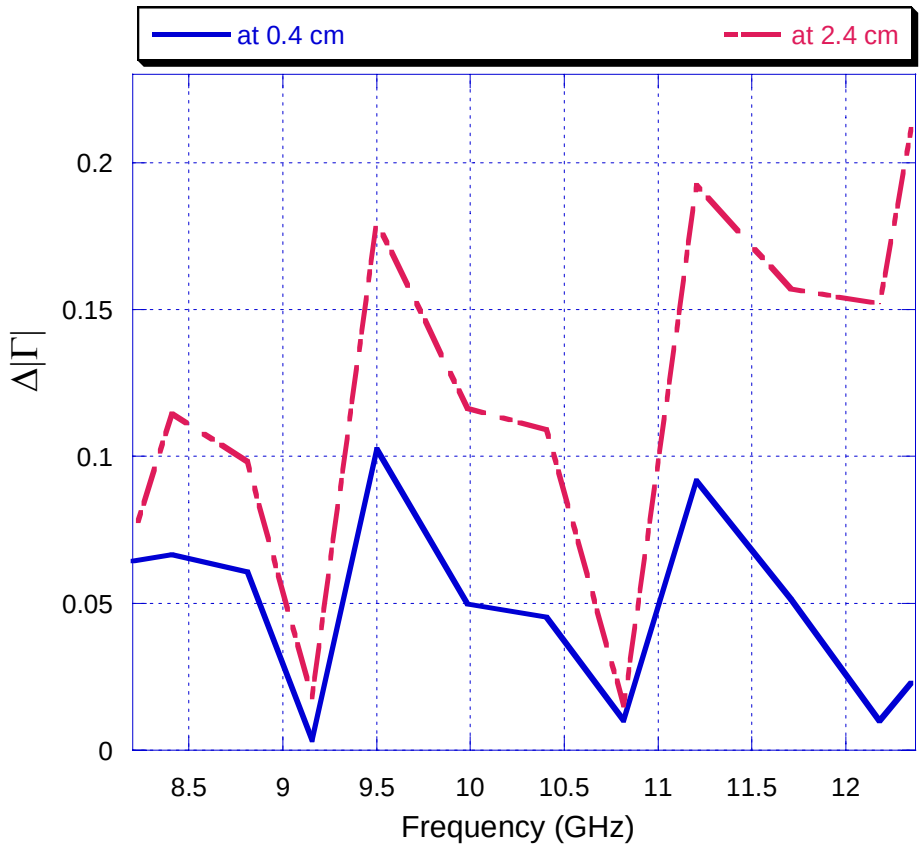


Figure 4-12: The magnitude difference of the reflection coefficient for two tumour locations, at 0.4 cm and 2.4 cm, at X-band for cancerous and normal breast tissue.

## *4.4 Summary and Remarks*

In summary, the experiments conducted using the uncalibrated measurement system show great potential of the near-field microwave non-invasive testing techniques for breast cancer detection. The experimentally obtained line scans provide detailed information about the breast under inspection, such as tumour presence, tumour size, and tumour location in the xy-plane. The relation between the reflection coefficient measurements and tumour location is not inversely proportional. Obtaining optimum operating frequency for each set of tumour 'settings' (such as physical dimensions, depth, dielectric properties) is necessary and has a great impact in increasing tumour detection sensitivity. Clearly the effects of altering the tumour size and dielectric properties and its influence on the reflection coefficient measurements have to be studied theoretically and experimentally in future research.

The breast phantom doesn't have the same dielectric properties as the real breast. Instead it has a smaller ratio in the dielectric contrast compared to normal and malignant tissues. The experimental results will be more precise if the dielectric properties of the real breast tissue parts are measured and obtained accurately. Measuring and getting the dielectric properties of the real breast tissue parts as well as malignant and benign at microwave frequencies will enhance the designing of an optimum microwave detection system that can detect tumour presence and distinguish a benign cyst from cancer.

# *CHAPTER 5*

## *Calibrated Experimental Measurements for Breast Cancer Detection*

### *5.1 Calibrated Microwave Measurement Setup*

The uncalibrated experimental results utilizing a rectangular waveguide probe in chapter 4 demonstrated the potential of near-field microwave techniques for breast cancer detection. Calibrated measurements should show in more detail the aptitude of near-field microwave techniques to be a successful medical accompaniment to existing screening tools for breast cancer detection, as well as providing authentication and verification of the simulation results developed in chapter 3. Calibrated measurements are based on measuring the complex reflection coefficient, $\Gamma$, at the rectangular waveguide sensor's aperture, whose magnitude and phase are then used to extract information about the tumour presence. Calibration adopted in this chapter is the process of determining the magnitude and phase of the reflection coefficient then comparing it with standard measurements and/or theoretical results. The calibration assures that the microwave system will produce results with a degree of confidence. Thus, the calibration process utilizing a slotted rectangular waveguide is primary performed with a short circuit at the termination point which will result in an infinite SWR (i.e. total reflection) and sharply defined voltage minima. Then the short circuit is removed and replaced with the breast phantom. Explicitly and consequently the maximum and minimum voltages with their relevant locations are measured and recorded to obtain the calibrated magnitude and phase of the reflection coefficient at the

waveguide sensor's aperture. The main difference between calibrated results and uncalibrated results is that the calibrated measurements have a frame of reference that gives them a quantitative assessment whereas the uncalibrated results (presented in chapter 4) are evaluated qualitatively. The calibrated microwave experimental system, shown in Figure 5-1, is composed of a microwave sweeper, sliding probe, diode detector, digital voltmeter and X-band rectangular slotted waveguide. A slotted line is a transmission line configuration (either rectangular waveguide or coax) that allows electric field amplitude sampling along a terminated line.

The microwave sweeper generates a microwave signal at the desired frequency, which is then fed into the slotted waveguide. The sliding probe senses the fields in the waveguide and the microwave signal is then applied to the diode detector. The rectified output is then low-pass filtered to prevent wasteful leakage of the microwave signal. If the microwave signal is amplitude modulated, then the detected output is the modulation signal. The standing-wave characteristics, shown in Figure 5-2, inside the slotted waveguide (which are related to the complex reflection coefficient) will be measured using a diode detector and a sensitive digital voltmeter. The standing-wave ratio, SWR, is measured by sliding the detector along the slotted waveguide and recording the maximum and minimum voltages. The ratio of these two voltages gives the standing-wave ratio.

The two measured parameters are the standing-wave ratio, SWR, and the position of a standing-wave minimum, $l_{min}$, in the slotted waveguide. A calibrated scale is marked along the slotted waveguide to provide the measurement of the physical distance moved by the carriage. The magnitude of the reflection coefficient is related to SWR by the following:

$$|\Gamma| = \frac{SWR - 1}{SWR + 1} \tag{5.1}$$

Knowing that the voltage minimum for a short circuit termination occurs when $e^{j(\phi-2\beta l)} = -1$, where $\phi$ is the phase of the reflection coefficient, the phase of the reflection coefficient, $\phi$, is given by:

$$\phi = \pi - 2\beta l_{\min} \tag{5.2}$$

where $\beta$ (given by $2\pi/\lambda_g$) is the wavenumber inside the waveguide, $l_{min}$ is the distance from the material under inspection to the first voltage minimum and $\lambda_g$ is the wavelength inside the waveguide [Poz.05].

Thus, the procedure for calibrated measurements utilizing a slotted rectangular waveguide is summarized as follows:

1. Place a short circuit at the termination point. This will result in a standing wave on the line with infinite SWR (i.e. total reflection) and sharply defined voltage minima (i.e. V = 0). On the arbitrarily positioned scale on the slotted line, the locations at which a minimum voltage occurs are recorded.
2. The short circuit is removed and replaced with the material under inspection. Then the maximum and minimum voltages are recorded to obtain the standing wave ratio, SWR, and the new locations for minimum voltage to occur are recorded as well.
3. Knowing that voltage minima and the reflection coefficient repeat every $\lambda/2$, $l_{min}$ can be found by taking the difference between two locations representing the minimum voltages for the short circuit and the material under inspection respectively. To confirm $l_{min}$ is correct, it must be less than $\lambda/2$.
4. Apply equations (5.1) and (5.2) to find the complex reflection coefficient, $\Gamma$, at the rectangular waveguide sensor's aperture.

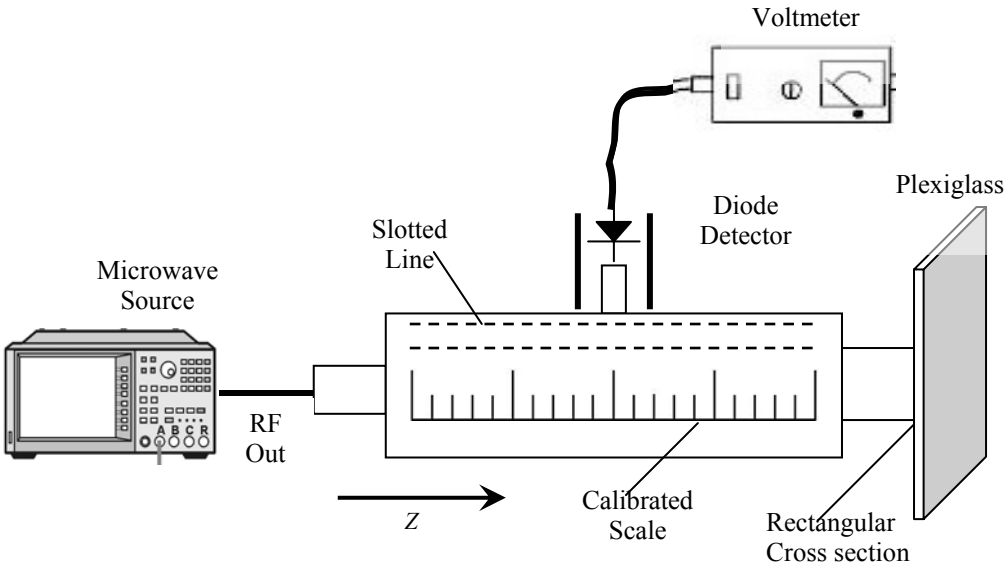


(a)

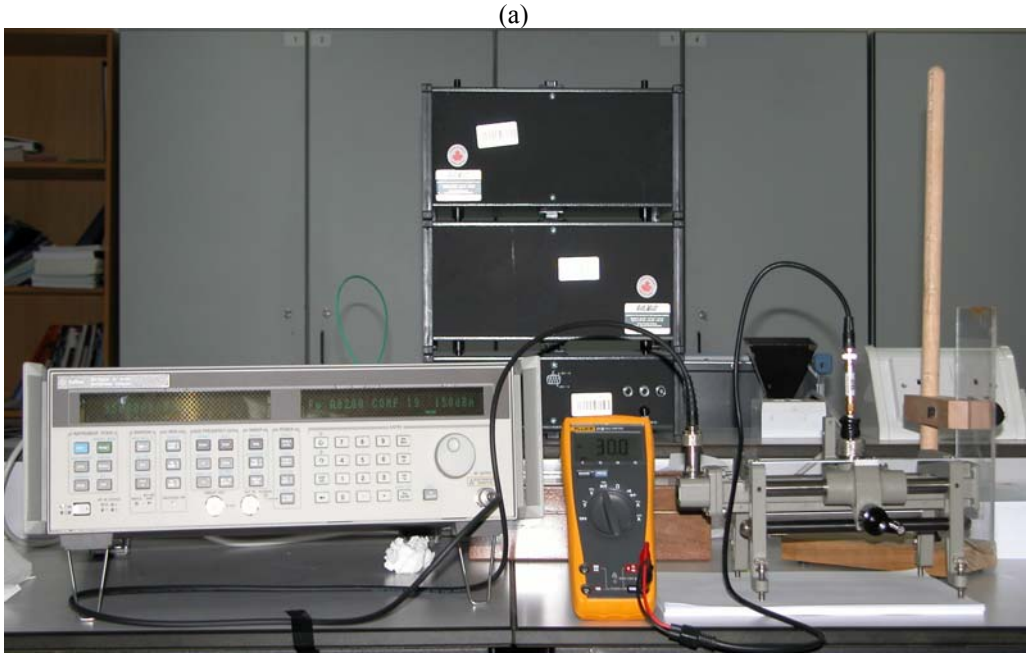

(b)

Figure 5-1: Near-field microwave calibrated measurement system: (a) schematic diagram (b) real system.

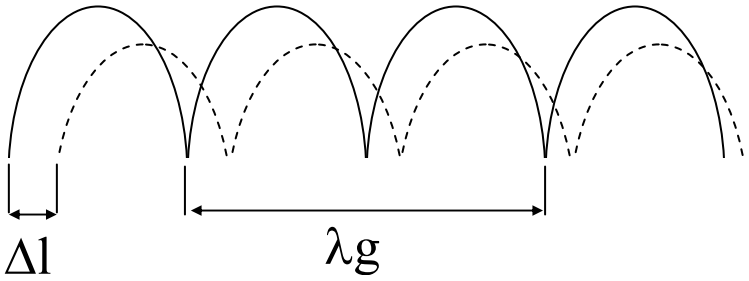


Figure 5-2: Standing wave patterns in a waveguide produced with and without a defect.

## *5.2 Validation of the Calibrated Microwave Measurement Setup Using Simple Dielectric Structure*

To obtain a better insight into the nature of the calibrated measurement approach and the resulting imaging mechanism, and to minimize the sources of errors, it is worth first applying the above mentioned setup to standard loads and a simple dielectric 'test' structure, rather than apply it directly for breast cancer detection. Once the system is shown to work properly and the measured data agree with the theoretical results, then the same setup can be applied with confidence to the breast phantom. The two standard loads that will be utilized to test the integrity of the system are a matched load and a metallic sheet, as shown in Figure 5-3. The properties of the matched load are that all the incident signal is absorbed by the matched load and none is reflected back. Thus, it has no reflected power and the return loss is infinity dB, i.e. its reflection coefficient is zero ($\Gamma = 0$). With the metallic sheet as a load however, all incident power is reflected and total reflection occurs (i.e. $\Gamma = -1$) and the return loss is zero dB. These two standard loads were placed in front of the slotted line and in contact with the slotted rectangular waveguide aperture (in place of the plexiglass sheet shown in Figure 5-1). The maximum and minimum voltages were recorded for both loads. The minimum voltage for the sheet of metal was indeed zero, i.e. total reflection occurs. Also the minimum and maximum voltages for the matched load changed only very slightly resulting in SWR of 1.04, i.e. very close to 1, confirming a reflection coefficient in this case of almost zero. Thus the theoretical results agree very well with measurements for the standard loads.

After these initial measurements, a further evaluation of the proposed calibrated test system was performed, using a plexiglass sheet, as shown in Figure 5-1. The plexiglass was chosen because its dielectric properties are well documented at X-band

and it is readily available. The thickness of plexiglass was measured by a vernier calliper as shown in Figure 5-4. The plexiglass sheet relative dielectric constant ($\varepsilon_r$) is 2.59 and the skin depth ($\delta$) is 0.007 m for frequency range from 8.2 GHz to 12.4 GHz [Bak.93].

Three sets of measurements for two parameters, namely the magnitude and the phase of the reflection coefficient, were thus determined for 4.0 mm plexiglass sheet backed by an infinite half-space of air. Figures 5-5 and 5-6 show the magnitude and phase of the reflection coefficient that have been calculated and measured as a function of frequency at X-band using two measurement techniques and the theoretical results obtained from the mathematical model of chapter 2. Namely, equation (2.69) was used to calculate the theoretical results for the magnitude and phase of the reflection coefficient. The two measurement techniques implemented were that using the slotted waveguide technique discussed in this chapter and shown in Figure 5-1 and, for comparison purposes, one using a vector network analyser (VNA)[1].

From Figures 5-5 and 5-6, the theoretical and experimental results have the same trend and follow each other closely. It is essential here to remember that the range of the reflection coefficient magnitude, $|\Gamma|$, varies from 0 to 1 ($0 \leq |\Gamma| \leq 1$). The small variation of the measured values from those calculated theoretically is attributed to several factors. Some of these factors are the nonlinearities and the noise associated with the measurement apparatus, the slight variations in the dielectric properties of the plexiglass sheet in the swept frequency range and the dimensional precision in order to minimize air gaps between the plexiglass sheet and the waveguide flange. Also, the theoretical model obtained in chapter 2 of this thesis accounts for the dominant mode excitation ($TE_{10}$) only and has not account for higher-order modes. Also, the plexiglass sample is low-loss dielectric (assuming $\sigma \approx 0$); then there will be some differences between the

measurements and the simulation results. There might be small discrepancies between the simulation and experimental results due to the numerical technique adopted and mathematical approximations since the solution of the equations is not obtained in closed form. Besides, the code developed for the theoretical model assumes an infinite waveguide flange, where as for the measurements, 41 mm x 41 mm flange is used. Last but not least, the standing-wave ratio is measured by sliding the detector along the slotted waveguide and recording the maximum and minimum voltages. The ratio of these two voltages gives the standing-wave ratio. In doing so, the operating point of the diode detector (on its V-I characteristic curve) is not the same when measuring the maximum and the minimum voltages. This causes measurement error associated with determining the SWR. In spite of all the above the agreement between theory and experiment is good, with the slotted waveguide approach yielding a reflection coefficient magnitude within 10% of that theoretically predicted over the whole frequency range investigated, while the agreement for the phase being even closer.

Figure 5-3: Standard loads; a metallic sheet (left) and a matched load (right).

[1] The measurements obtained for the plexiglass sheet using the VNA was conducted in one of the labs in USA because the VNA is not available in our lab. A sample of the plexiglass sheet was sent with all its specifications and the magnitude and phase of the reflection coefficient were measured.

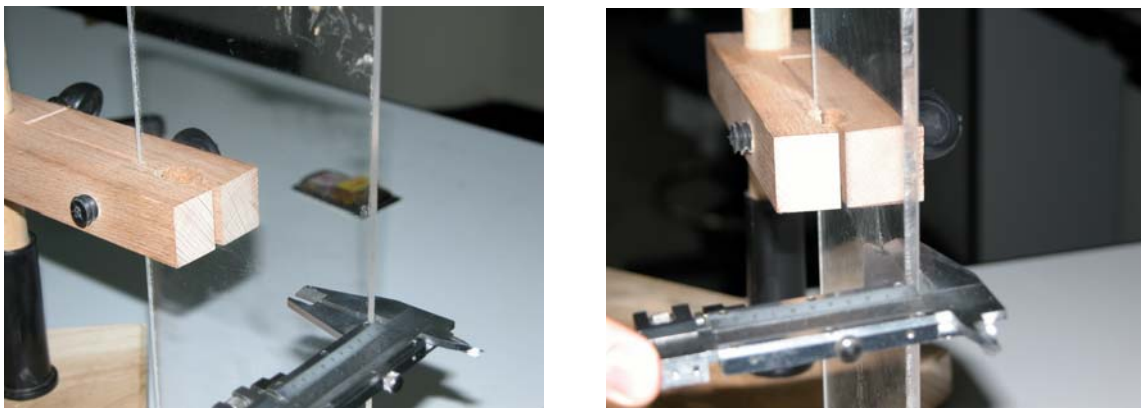

(a) (b)

Figure 5-4: (a) Front view and (b) side view of: Plexiglass sheet of 4.0 mm thickness with vernier calliper measuring its thickness.

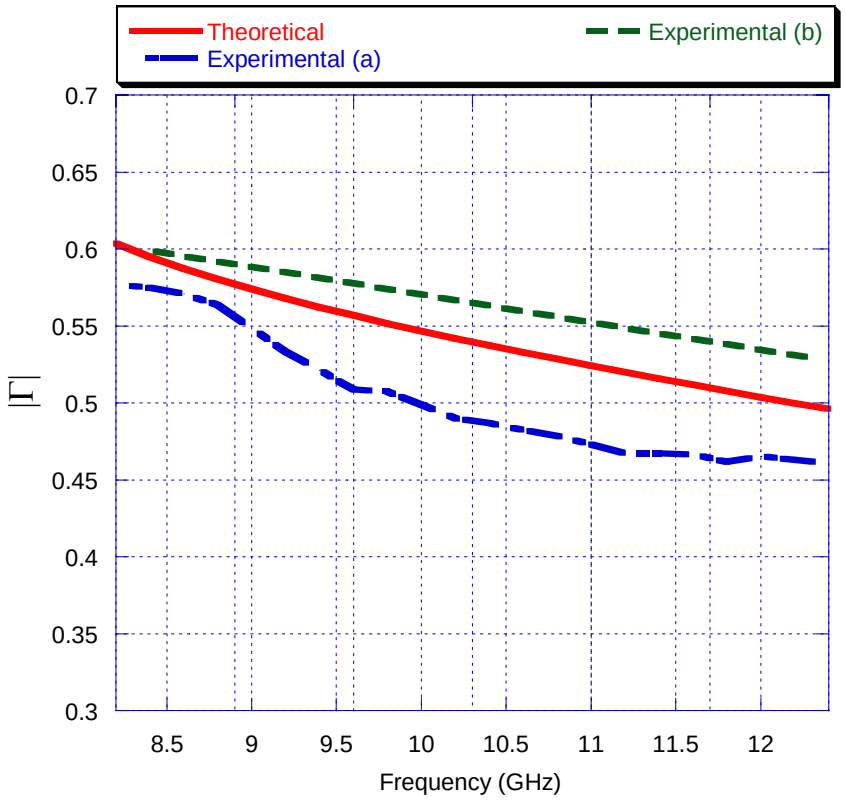


Figure 5-5: Magnitude of the reflection coefficient for 4.0 mm plexiglass sheet as function of frequency at X-band. Experimental results (a) are conducted with the VNA and (b) with the slotted waveguide technique.

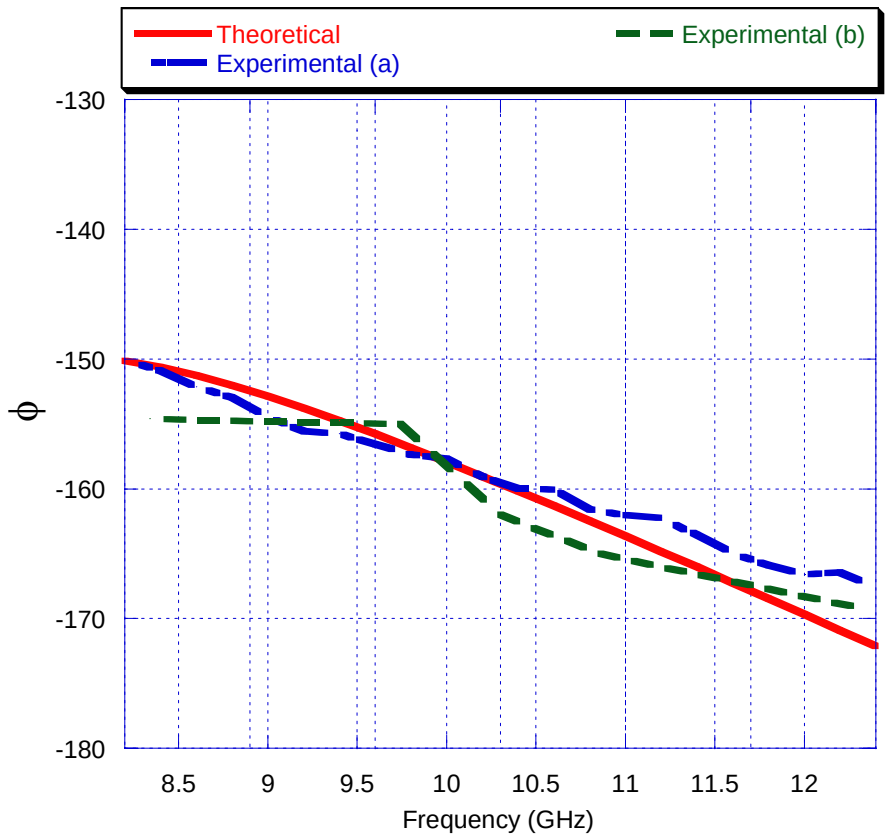


Figure 5-6: Phase of the reflection coefficient for 4.0 mm plexiglass sheet as function of frequency at X-band. Experimental results (a) are conducted with the VNA and (b) with the slotted waveguide technique.

## *5.3 Calibrated Experimental Results for Breast Phantom*

After confirming the reliability between the theory and measurements for standard loads and a simple test structure (plexiglass), the slotted waveguide setup will be utilized to obtain calibrated measurements of the magnitude and phase of the reflection coefficient during a 1-D line scan for breast cancer detection. Consequently, a 2-D experimental calibrated image of the magnitude of the reflection coefficient will be produced to show the aptitude of this system to detect tumour presence within the breast phantom.

As mentioned earlier and as shown in Figure 5-7, the microwave sweeper generates a microwave signal in the X-band, which is then fed into the slotted waveguide. The sliding probe senses the microwaves inside the waveguide and the

microwave signal is then applied to the diode detector. The standing-wave characteristics inside the slotted waveguide will be measured using the diode detector and a digital voltmeter. The flange of the slotted waveguide is in contact with the breast phantom. The tumour is located at the centre of the phantom in the xy-plane and directly after the skin simulant in the yz-plane (where z-direction is the direction of propagation). The breast phantom properties were given in section 4.1 of this thesis.

From chapter 4, it was found that 9.5 GHz is the optimum frequency in the X-band for tumour detection in the breast phantom. Also, the range from 8.2 GHz ending to 8.8 GHz tends to be sensitive enough for tumour presence detection. Thus the experimental 1-D line scans will be conducted at 8.5 GHz and 9.5 GHz. The standing-wave ratio, SWR, and the position of a standing-wave minimum, $l_{min}$, in the slotted waveguide are measured for each and every location while moving the breast phantom in the xy-plane. Then equations (5.1) and (5.2) are applied to find the complex reflection coefficient, $\Gamma$, at the rectangular waveguide sensor's aperture. Figures 5-8 and 5-9 show a line-scan of the magnitude and phase of the reflection coefficient as a function of the breast x-displacement, respectively. It is obvious from both figures that the magnitude as well as the phase changes when the tumour simulant is in front of the sensor's aperture. The noticeable variation in the reflection coefficient is due to the dielectric contrast between the normal breast tissue simulant and the tumour simulant. Furthermore, the magnitude difference at 9.5 GHz is much greater than the magnitude difference at 8.5 GHz. Thus 9.5 GHz is confirmed as the optimum frequency at X-band. This fully agrees with the conclusions obtained for the uncalibrated measurements using the scalar network analyzer. Whereas for the phase measurements, 9.5 GHz is slightly better than 8.5 GHz since the phase difference for both frequencies are close to each other.

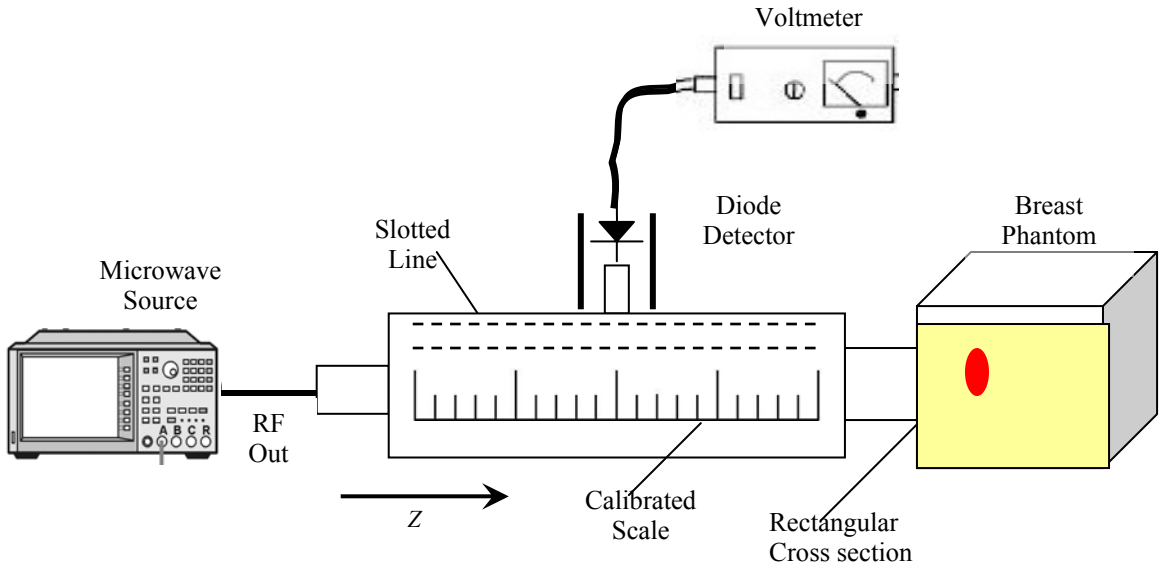


(a)

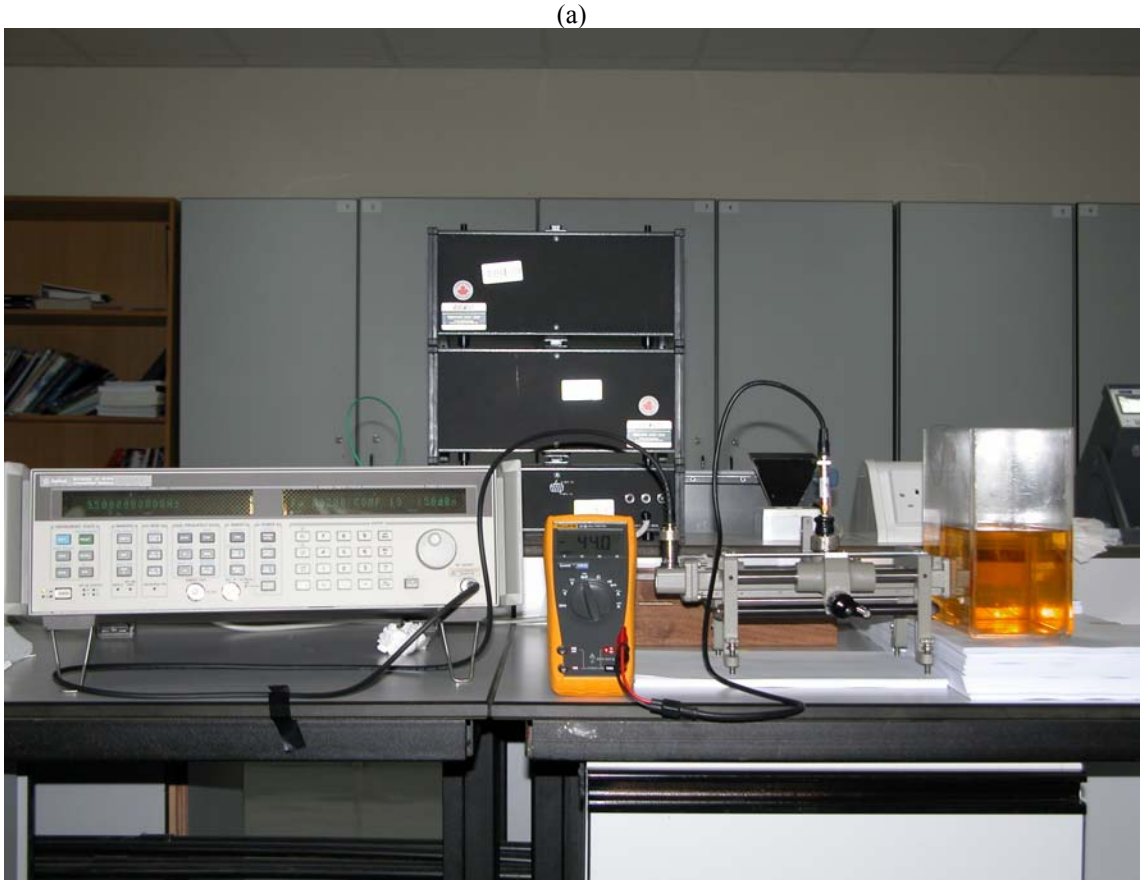

(b)

Figure 5-7: Near-field microwave calibrated measurement system with breast phantom under inspection: (a) schematic diagram (b) real system.

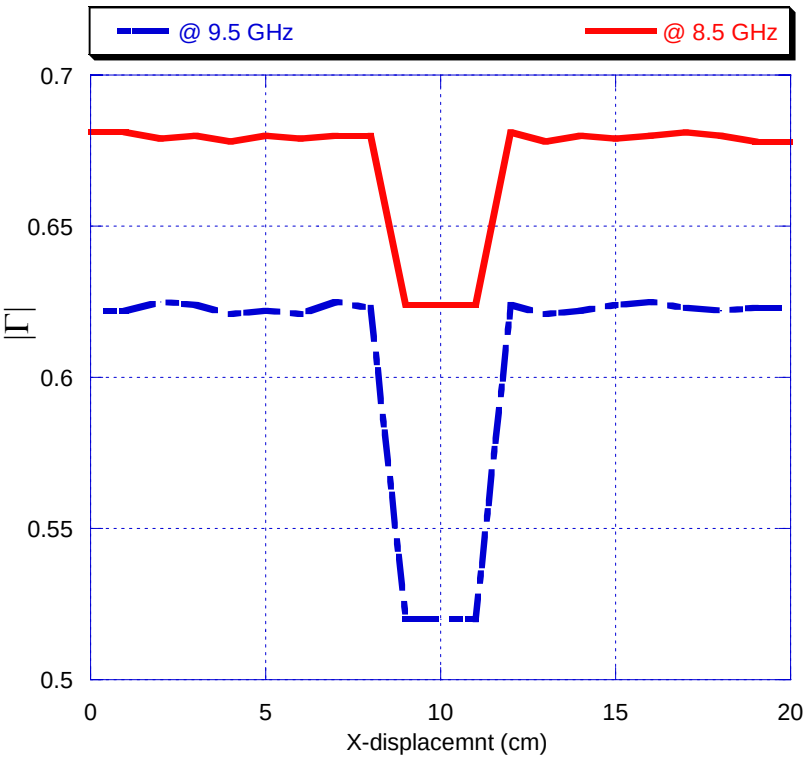


Figure 5-8: Calibrated magnitude line scan of the reflection coefficient as a function of the breast x-dimension for breast phantom with a tumour located at the centre in the xy-plane.

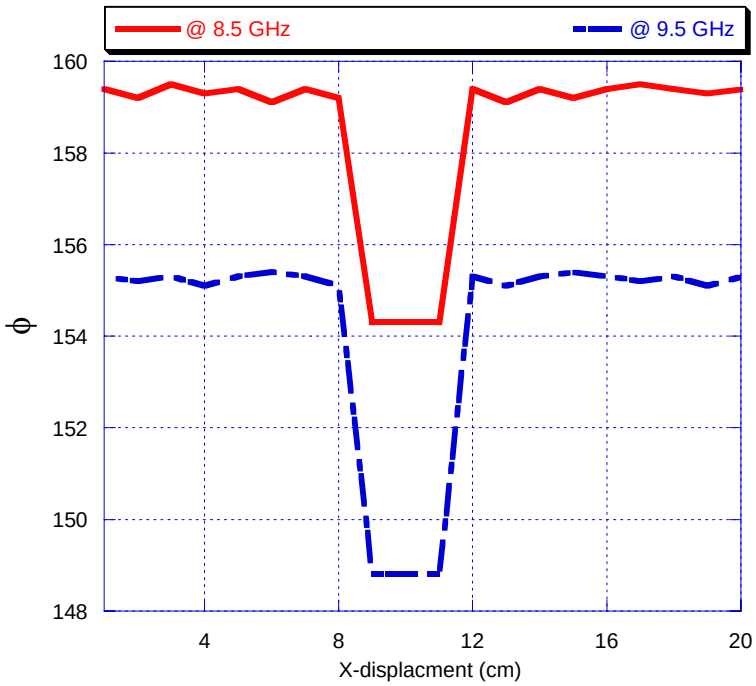


Figure 5-9: Calibrated phase line scan of the reflection coefficient as a function of the breast x-dimension for breast phantom with a tumour located at the centre in the xy-plane.

To validate the calibrated experimental results theoretically, the reflection coefficient was calculated and simulated using the 3-layer breast model of chapter 3 but for the same properties of the breast phantom adopted practically. Figures 5-10 and 5-11 show a comparison between the theoretical and measured magnitude and phase of the

reflection coefficient as a function of the breast x-dimension for breast phantom with a tumour located at the centre in the xy-plane operating at 9.5 GHz, respectively. It is clear from both figures that the variations in theoretical magnitude and phase are qualitatively the same as those observed experimentally. There are however, as might be expected, quantitative differences. In particular, the theoretical magnitude and phase differences are greater than the measured magnitude and phase differences.

The interpretation of the quantitative mismatch of these results is due to many factors. In section 4.1 it has been mentioned that the artificial tumour is represented by a diacetin solution poured into a 2 cm by 3 cm balloon. However, the balloon thickness and its dielectric property are not accounted for in the simulation. In addition, the diacetin solution conductivity ($\sigma$) is taken (from literature) to be 1.9 S/m at 6 GHz and the normal breast tissue simulant conductivity ($\sigma$) is 0.05 S/m at 6 GHz, whereas the operating frequency is 9.5 GHz, and this might lead to quantitative differences. Indeed, the imaginary part of the dielectric property ($\varepsilon_r''$) is a frequency dependent parameter and its relation with the conductivity and the frequency is given by $\varepsilon_r'' = \frac{\sigma}{2\pi f \varepsilon_o}$. Furthermore, from a practical perspective there may be some air voids inside the balloon since it might not be completely filled with the tumour simulant. Also, the previously described sources of errors associated with the analysis of Figures 5-5 and 5-6 will apply to Figures 5-8 to 5-11 as well.

The presence of one or more of the above mentioned conditions is sufficient to vary the output signal. Indeed, it has been shown previously that small variations in the parameters (in particular the dielectric property or thickness of any layer of inclusion) change the output signal accordingly [Qad.98a]. Thus, it is to be expected that there will not an exact quantitative agreement between the experimental breast phantom results and those obtained theoretically. However, the qualitative agreement obtained is very good and gives a strong indication of the validity of the mathematical model presented

in chapter 2. The measurement uncertainty analysis discussed next was conducted at 9.5 GHz since it is the optimum frequency.

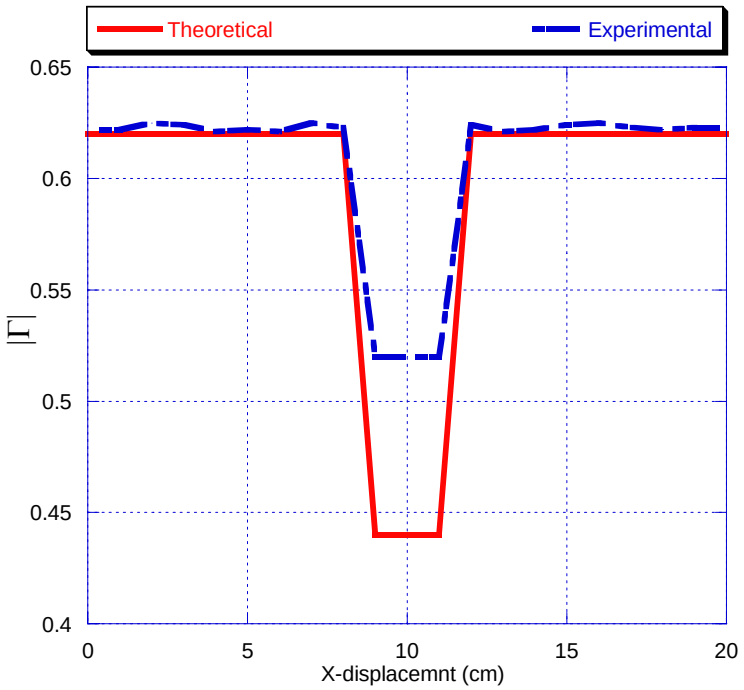


Figure 5-10: Comparison between the theoretical and measured magnitude of the reflection coefficient as a function of the breast x-dimension for breast phantom with a tumour located at the centre in the xy-plane operating at 9.5 GHz.

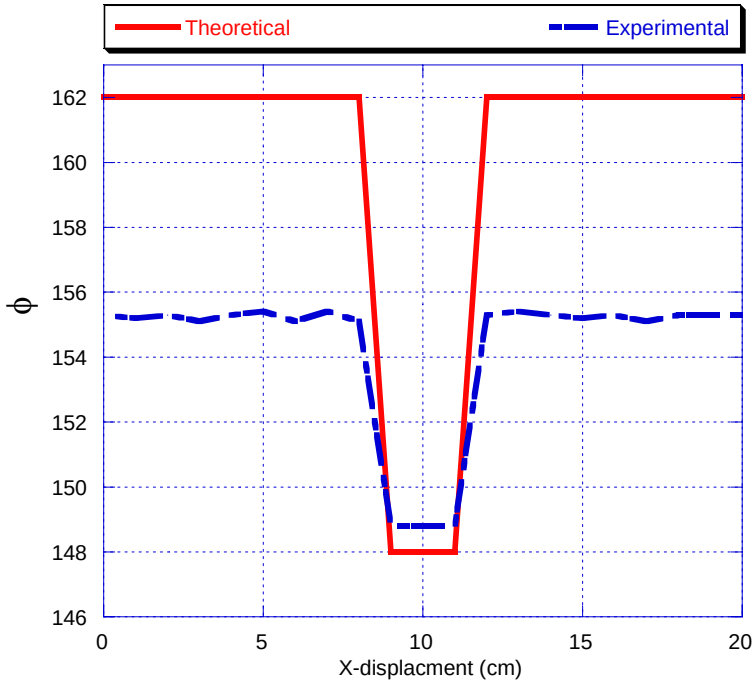


Figure 5-11: Comparison between the theoretical and measured phase of the reflection coefficient as a function of the breast x-dimension for breast phantom with a tumour located at the centre in the xy-plane operating at 9.5 GHz.

It is possible to estimate the measurement uncertainty associated with the setup and calibrated results described above by repeating the measurements several times for the same scenario and then calculating the standard deviation, $\sigma_{sd}$, of the measured value. Standard deviation is a measure of the variation of $M$ data points ($x_1 ... x_M$) about an average value and is typically called the uncertainty in a measured data. The measurement repetitions were conducted at 9.5 GHz and the number of measurements for each scanning point was ten. The standard deviation is displayed in Figure 5-12 as error bars associated with the measured values of the magnitude of the reflection coefficient. It is clear from the figure that the data obtained are trustworthy, with the measurement errors probably mainly due to either a position error of the indicated standing-wave minimum or to the voltmeter instability when measuring microvolts. The consistency of the measurements is also shown next in the 2-D experimental image in Figure 5-13.

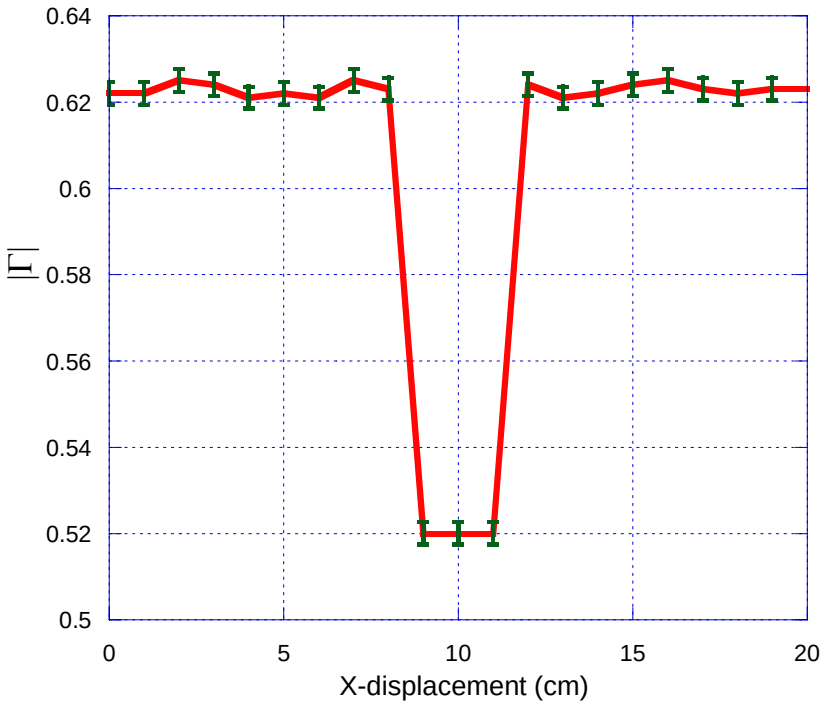


Figure 5-12: Measurement uncertainty display of the calibrated magnitude line scan of the reflection coefficient as a function of the breast x-displacement for breast phantom with a tumour located at the centre in the xy-plane operating at 9.5 GHz.

The calibrated measurement system discussed above offers a chance for obtaining a two-dimensional image of the breast phantom under inspection.

Consequently, the tumour may be viewed in two-dimensional image. Thus, a two-dimensional data matrix is obtained by moving the slotted waveguide in a raster scan in front of the breast phantom in steps of 0.5 cm in the imaging plane (x-y plane) and measuring the maximum and minimum voltage values that are proportional to the phase and/or magnitude of the reflection coefficient at the open-ended aperture of the waveguide. The scan is performed at a frequency of 9.5 GHz in contact fashion. The scan covered an area of 150 mm by 50 mm in x and y directions respectively.

This two-dimensional array of voltage SWR values was used to create a contrast 2-D magnitude reflection image of the breast phantom. Figures 5-13a and 5-13b display the signal intensity and the plan view of the calibrated magnitude of the reflection coefficient, $|\Gamma|$, with a tumour located at the centre in the xy-plane, correspondingly. The contrast is high and the tumour is evidently visible in the centre of the image. The magnitude difference is around 0.1. The size of the tumour on the image corresponds well with the physical size of the tumour. This indicates the high spatial resolution that may be attained with near-field microwave imaging [Sal.07].

One more significant observation on the image is the presence of two features along the sides of the tumour (marked by X as shown in Figure 5-13b). These features are due to the sidelobes of the radiator (sensor) and the edge effects of the tumour. Thus the sensor radiation attributes possess sidelobes that may interact with inner tumours and produce extra features within the image obtained.

Figure 5-14 shows a theoretical 2-D reflection magnitude image of the reflection coefficient at 9.5 GHz for breast phantom with a tumour located at the centre in the xy-plane to compare it with the calibrated 2-D reflection magnitude image shown in Figure 5-13. As for the 1-D result, there is very good qualitative agreement, and the value of the reflection coefficient magnitude is reduced over the region of the tumour. It is also noticed that certain features of the experimental image, in particular the sidelobes seen in the Figure 5-13 are also observed in the theoretical simulation (marked by X in

Figure 5-14). As for the 1-D result it can also be seen that the theoretical reflection coefficient magnitude varies between 0.62 and 0.44 as compared to the lower variation in the experimental case of 0.62 to 0.52. The contrast (and as a consequence perceived resolution) of the theoretical image is therefore greater.

The experimental image shown here is only used to detect the presence of tumour and to obtain good estimate of its spatial extent. Further analysis to determine more quantitative information about the properties of the tumour can be performed by conducting extensive experimental measurements and analyzing the measured data, but such additional experiments are outside of the scope of this thesis. Raster scan type of image formation is not the only approach to near-field microwave imaging. Similar images can be produced using 1-D or 2-D array of microwave probes [Bol.90] [Fra.98].

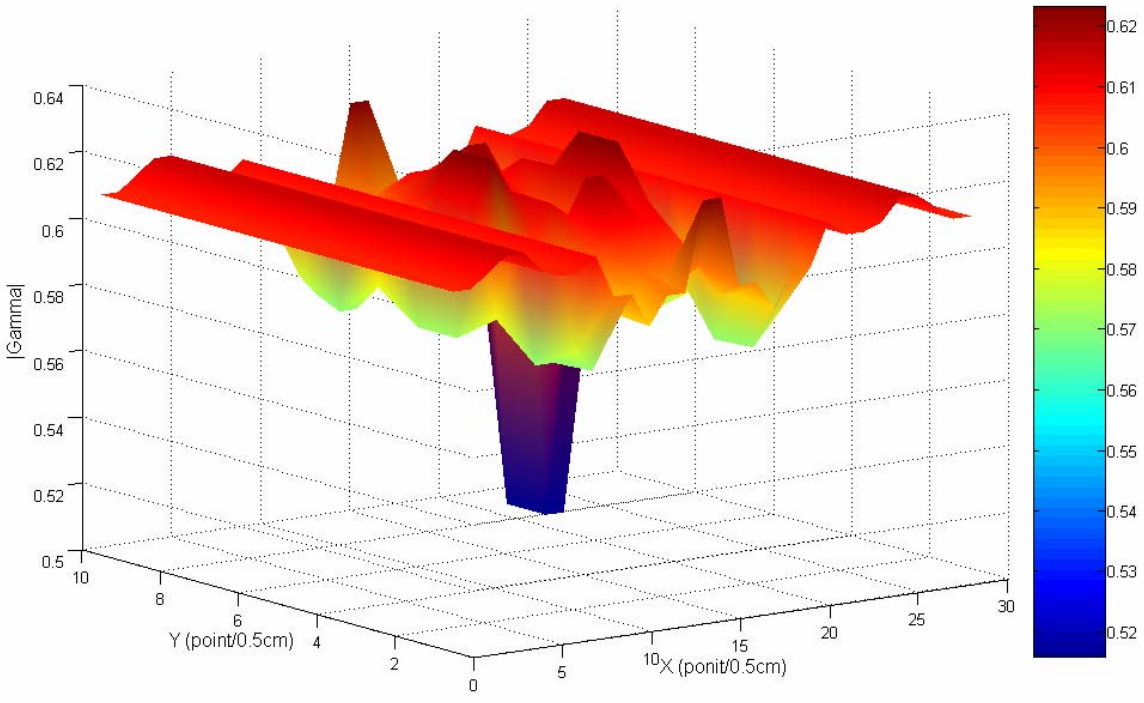


(a)

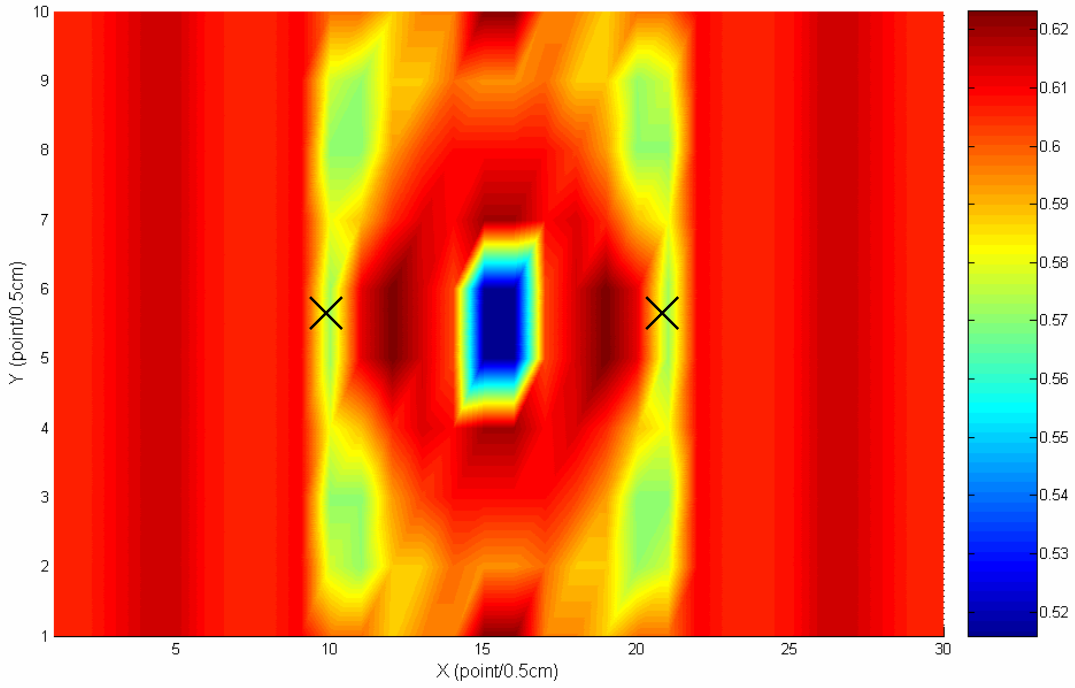


(b)

Figure 5-13: 2-D experimentally calibrated obtained image of the magnitude of the reflection coefficient at 9.5 GHz for breast phantom with a tumour located at the centre in the xy-plane: (a) signal intensity, (b) plan view.

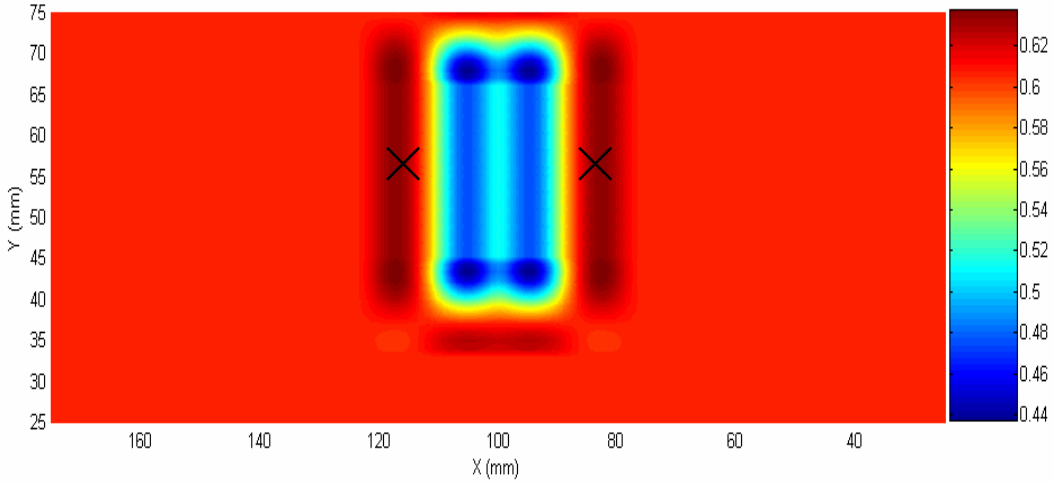


Figure 5-14: Theoretical 2-D reflection magnitude image of the reflection coefficient at 9.5 GHz for breast phantom with a tumour located at the centre in the xy-plane.

## *5.4 Summary and Remarks*

In conclusion, the experimental results presented in this chapter show clearly the suitability of near-field microwave techniques for breast tumour detection. In addition the reliability of the theoretical formulations presented in chapter 2, as well as the usefulness of the uncalibrated measurements obtained in chapter 4 is evident. An experimental system utilizing a slotted waveguide for calibrated measurements is presented and its operation is clarified. With the slotted waveguide, the SWR and the variation in the phase of the reflection coefficient can both be measured reliably. Indeed, the slotted waveguide used to be the primary way of measuring reflection coefficient, but it is been largely supplanted in modern times by the vector network analyzer in terms of accuracy, versatility, and convenience. It is true that measuring the reflection coefficient using the slotted line takes a lot of time compared to a vector network analyzer, but from a cost perspective the slotted waveguide is far superior.

A detailed analysis and comparison between calibrated measurements and simulation results for standard loads and simple dielectric structure (plexiglass) was presented. The agreement between the theoretical and measured results for the simple dielectric structure (plexiglass) was good, but could be improved even more by having better and accurate knowledge of the plexiglass dielectric properties over the full range of frequencies used. There was an agreement between the simulation analysis and the experimental results for the VNA and the slotted waveguide technique. With the slotted waveguide approach, the reflection coefficient magnitude was within 10% of that theoretically predicted over the whole frequency range investigated. At the beginning of the frequency band, the difference is almost zero and it increased with frequency. As for the phase measurements, the agreement was very close and there was a great match between the theoretical results and the practical measurements. However, there were

some discrepancies between the simulation and experimental results. Many factors have impact on this discrepancies such as the numerical technique adopted and mathematical approximations since the solution of the equations is not obtained in closed form. Also, the code developed for the theoretical model assumes an infinite waveguide flange, where as for the measurements, 41 mm x 41 mm flange was used. Moreover, the operating point of the diode detector (on its V-I characteristic curve) was not the same when measuring the maximum and the minimum voltages for the standing-wave ratio measurement. This resulted in measurement error associated with determining the SWR.

1-D line scans and a 2-D contrast image of the breast phantom with the tumour simulant embedded within the phantom were presented. These scans and images have been created using a measured voltage that is related to the magnitude and/or phase of the effective reflection coefficient at the microwave sensor's aperture. These scans and image convey detailed information about the structure and the integrity of the breast phantom under inspection. The size of the tumour within the scans and the images closely agrees with its physical size, which points out the high resolution accompanied with this technique.

There were quantitative discrepancies between the simulations and the practical results. The theoretical magnitude and phase differences were greater than the measured magnitude and phase differences. The magnitude difference for the theoretical results was around 0.18 whereas the difference for the measurements was around 0.1. Also, the phase difference for the theoretical results was around 14° degrees whereas the difference for the measurements was around 6° degrees. The explanation of this quantitative mismatch of these results was due to many factors such as the balloon thickness and its dielectric property were not accounted for in the simulation. In addition, the diacetin solution conductivity ($\sigma$) was taken to be 1.9 S/m at 6 GHz and the normal breast tissue simulant conductivity ($\sigma$) is 0.05 S/m at 6 GHz, whereas the

operating frequency was 9.5 GHz. The imaginary part of the dielectric property ($\varepsilon_r''$) is a frequency dependent parameter and its relation with the conductivity and the frequency is given by $\varepsilon_r'' = \frac{\sigma}{2\pi f \varepsilon_o}$. Furthermore, from a practical perspective there may be some air voids inside the balloon since it might not be completely filled with the tumour simulant. However, the qualitative agreement between the theoretical results and the calibrated experimental measurements confirms the validity of the mathematical model presented in chapter 2. Thus, a calibrated non-invasive near-field microwave detection system has been successfully designed and built to experimentally detect tumour simulant in the breast phantom. This was achieved by measuring the magnitude and/or phase of the reflection coefficient at the sensor's aperture.

# *CHAPTER 6*

## *Conclusions and Further Work*

In this thesis, theoretical formulations and experimental measurements were delivered to show the potential of near-field microwave non-invasive testing and evaluation (NIT&E) techniques utilizing an open-ended rectangular waveguide sensor for breast cancer detection. The high contrast in the dielectric properties between normal and malignant breast tissues is the attractive feature for tumour detection with microwave imaging and non-invasive testing techniques. The interaction of electromagnetic waves, at microwave frequencies, with multilayered dielectric media is fundamental for any microwave screening or testing application. However, a reliable and optimised detection process can not be achieved without detailed knowledge and analysis of the interaction between the microwaves and the breast structure in the near-field region. That is why it was of great importance to understand the interaction of the electromagnetic fields radiated from the microwave sensor, namely an open-ended rectangular waveguide sensor, with the breast under inspection.

Thus, chapter 2 was designated to develop a mathematical model of the interaction between electromagnetic waves, at microwave frequencies, with N-layer dielectric media. Determining and simulating the near-field radiation properties, namely the normalized electric field, the real power pattern and the imaginary power pattern was the main target when developing the mathematical model. Accordingly, calculating and obtaining the phase and the magnitude of the effective reflection coefficient at the rectangular waveguide aperture, as well as theoretical 1-D line scans and 2-D images was another major intention from the developed mathematical model. A Fourier Transform Matching method, not widely used in medical microwave imaging, formed

the basis of the mathematical model and proved most useful in finding the necessary solutions for electric field properties within the N-layer dielectric medium. Subsequently, equations (2.16) (2.57) and (2.69) formed the basis for a computational simulation analysis presented in chapter 3.

Moreover, the general N-layer dielectric structure terminated by infinite half-space (IHS) of air with an inclusion (tumour) in the near-field region developed in section 2.1.7 was adopted. Backing the breast by a metallic sheet will not be beneficial because the breast is a high lossy dielectric material. So, the signal will not reach the end of the breast. In addition, it will be easier and smoother for the patient when imaging the breast since locating any metallic plate at the opposite end of the imaging plane is not needed and squeezing the breast tissue is avoided. But still, the case of backing the N-layer dielectric structure with a conductor was derived for the purpose of future research, in case there is an opportunity of combining near-field microwave imaging with other screening tools or testing techniques. Adding a conductor sheet at the opposite side of the breast might enhance the detection sensitivity since total reflection will occur and it is as if the breast is screened twice (keeping in mind that the penetration depth has to be increased more than the present penetration depth to reach the other end of the breast).

The development of a general model for the electric field properties within N-layer dielectric structure (rather than limiting the model to just a few layers), as carried out in Chapter 2, can form the basis for a more realistic and detailed breast-model and form part of advanced research and investigation concerning breast cancer detection using near-field microwave NIT&E techniques. That will come about when accurate measurements of the dielectric properties of breast tissues and its constituents exist at microwave frequencies and when the dielectric properties of malignant and benign tissues (such as malignant cancer, cyst, mastalgia, calcification, etc.) are measured or known at microwave frequencies. Other properties must be taken into consideration

such as the physical properties, dimensions, etc. of the different parts of the breast while developing a near-field microwave imaging system. Fortunately and recently, M. Lazenik, *et al.* have started measuring the dielectric properties of breast tissues for 490 breast tissue samples from 93 patients over 0.5-20 GHz frequency range [Laz.07]. Thus, although the detailed N-layer model was not used extensively for simulations in this thesis, because of the above mentioned uncertainty that exists in the literature on the dielectric properties of normal breast tissue and the existence of little data regarding the dielectric properties of benign and malignant tumours at microwave frequencies, it should prove most useful in future. In this thesis the 3-layer approximation to the general-N layer case was used extensively and proved most useful in predicting the likely performance of our near-field microwave approach to breast cancer detection.

In chapter 3, an extensive theoretical computational simulation analysis was conducted to bring to light the promise of near-field microwave NIT&E technique for breast cancer detection. To fully understand the imaging mechanism of the open-ended rectangular waveguide probe, the near-field radiation patterns (normalized electric field, real power pattern and imaginary power pattern) were computed and analyzed. The analysis of these patterns allowed assessing the presence of tumour within the breast tissue. Theoretical images (magnitude and phase images) of the effective reflection coefficient of cancerous breast showed that detection of tumour presence was possible. Forming the images theoretically for different setups played a significant role in optimising the resolution and sensitivity of the acquired reflection images. Also, forming these images theoretically might assist in solving the inverse problem in future.

The optimisation parameters that were tackled through the simulations in chapter 3 included investigating the influences of frequency of operation, loading of the waveguide sensor and dielectric properties of the standoff distance medium. The effect of each optimisation parameter was shown on the radiation patterns and theoretical reflection images. The dielectric properties of the standoff distance were not optimised

efficiently. Instead, estimation of the local optimum dielectric standoff was adopted in the simulation analysis.

When the waveguide was empty (8.2GHz – 12.4GHz), the magnitude difference and the phase difference of the reflection coefficient were around 0.05 and 1.2° degrees respectively. There was no observable optimum frequency of operation when the waveguide was not loaded. Whereas when the waveguide was completely filled with a dielectric material of relative permittivity $\varepsilon_r$ = 12.25 (2.34GHz – 3.54GHz), the maximum magnitude difference was achieved at the end of the frequency band and it was around 0.57. Also, the maximum phase difference was obtained at the beginning of the frequency band and it was around 24° degrees. 3.0 GHz tended to be an optimum operating frequency. Thus, operating at 3.0 GHz, the magnitude difference was around 0.53 and the phase difference was 15° degrees for 5 mm tumour depth. Therefore, the magnitude as well as the phase detection sensitivity turned out to be higher when the waveguide was loaded.

When the microwave sensor was loaded (i.e. operating at 3.0 GHz) and a 1.0 mm standoff distance with relative permittivity $\varepsilon_r$ = 35.3 was attached to the sensor's aperture, the real power was coupled more into the breast. For example, for 10 mm tumour depth, the power shifted from -16 dB to -13 dB. Therefore, the real power density increased when a standoff distance medium with finite dimensions and known relative permittivity was introduced at the sensor's aperture. The maximum difference in the magnitude image when there was no standoff dielectric is 0.16. However, when the 1.0 mm standoff dielectric was present, the maximum difference in the magnitude image became 0.2 (for 10 mm tumour depth). Thus the detection sensitivity became 1.25 times better when the standoff dielectric was present. The dynamic range of the phase image when there was no standoff dielectric is 0.5° degrees. But when the 1.0 mm standoff dielectric was introduced, the dynamic range of the phase image became 2° degrees (for 10 mm tumour depth). Therefore, the magnitude as well as the phase

detection sensitivity increased more when the waveguide was loaded and a standoff distance with certain relative permittivity was introduced.

The multidimensional optimisation (i.e. optimising: (1) the frequency of operation; (2) the probe's filling; (3) and the standoff distance medium dielectric properties) enhanced the detection sensitivity, increased the penetration depth (lower frequency of operation), and improved the spatial resolution. This 3-D optimisation resulted in detecting the tumour presence within the breast. Hence, the simulations presented in chapter 3 verified the successful possibility of implementing the developed image formation model practically.

In chapter 4, a breast phantom that mimicked the dielectric properties contrast of the real breast model (presented in section 1.11 of this thesis) was developed. The constituents of this phantom were selected based on their dielectric properties, such that the dielectric properties of the breast phantom have a similar ratio in the dielectric constant contrast between normal and malignant tissues. This phantom was utilized for experimental investigation since using such phantoms is common practice in medical microwave imaging and negates the need for the IRB-approval necessary to perform measurements with real patients and on real breasts.

An experimental setup for uncalibrated measurements, of the reflection coefficient magnitude only, was developed and its operation was discussed. Several experimental results were shown and relative information, such as tumour existence, about the cancerous cell within the breast were obtained. The uncalibrated measurements showed great potential of the near-field microwave non-invasive testing techniques for breast cancer detection. The experimentally obtained line scans expressed detailed information about the breast phantom under inspection. This information included tumour existence, tumour physical dimensions, and tumour position in the xy-plane.

In chapter 5 more detailed experimental results were presented both to further investigate the integrity of the simulation results presented in chapter 3 and to further address some practical issues. An experimental system utilizing a slotted line with rectangular waveguide cross-section for calibrated measurements of both magnitude and phase of the reflection coefficient was developed and its operation was explained. The magnitude and the phase of the effective reflection coefficient were measured with the slotted waveguide by making measurements on standing wave set-up within the slotted line. This approach provides a more cost-effective measurement approach as compared to the use of expensive vector network analysers. A detailed and in-depth analysis and comparison between calibrated measurements and simulation results for standard loads and simple dielectric structure (plexiglass) were presented, and comparisons between the slotted-line approach and sample vector analyser results were made. In all cases the agreement was good.

The experimental results presented in chapter 5 demonstrated the validity of the theoretical formulations presented in chapter 3 as well as the uncalibrated measurements obtained in chapter 4 to a greater extent. 1-D line scans and 2-D contrast image of the breast phantom with the tumour embedded within the phantom were presented. These scans and image were created using a measured voltage that is related to the magnitude and/or phase of the effective reflection coefficient at the microwave sensor's aperture. These scans and images conveyed detailed information about the structure and the integrity of the breast phantom under inspection. The size of the tumour within the scans and the image closely agreed with its physical size which pointed out the high resolution accompanied with this technique. In addition, the theoretical-versus-experimental qualitative assessment for the breast phantom confirms the validity of the mathematical model presented in chapter 2 and shows the promise of near-field microwave NIT&E techniques utilizing an open-ended rectangular waveguide sensor for breast cancer detection. Thus, a calibrated near-field microwave

non-invasive detection prototype system was designed and built to experimentally detect tumour presence via measuring the magnitude and/or phase of the effective reflection coefficient at the sensor's aperture.

There is still a massive amount of research and development to be conducted in order to achieve good performance. Current and in-progress measurements of dielectric properties of normal breast tissue and classic abnormalities will grant a solid base for the improved design of microwave imaging systems. The use of a computer controller or a microcontroller with data acquisition board allows for real-time processing and display of the measurement results as a function of the phantom physical size or as a function of the frequency band of the microwave sensor.

A detailed study in the radar and wireless communication fields is definitely of great significance for future endeavours in the field of near-field microwave medical imaging. Recent trends in these fields have been toward miniaturizing and ruggedizing **(**adapt something for hard use**)** hardware, improving hardware performance, and integrating system functions. These trends suggest that in the future it will become more feasible and cost-effective to integrate microwave monitoring systems directly into manufacturing lines. In view of the trend towards miniaturization, an increase in the use of sensor arrays to permit rapid inspection of larger areas or to achieve higher spatial resolution is expected. In addition, microwave sensors will be increasingly operated at millimetre-wave frequencies and combined with other types of sensors (such as optical sensors, ultrasound sensors, etc.) in what so called "sensor fusion" or "multi-sensor data fusion" to provide greater sensitivity and discrimination.

Data processing techniques may serve as valuable tools in complex cases where the measurement parameters such as small tumours are highly correlated. Multivariable regression models and neural networks are some of the techniques which can be used both for theoretical expositions and on-line measurement setups to aid in multiparameter measurements. Near-field microwave NIT&E techniques will also

benefit from the current activities aimed at combining sensors with digital signal-processing and microcontroller hardware to produce smart sensors that are, for example, self-calibrating or adaptive to their environment.

Lastly, near-field microwave NIT&E techniques are still a current field of active research, and such work will lead to continuous improvements in measurement techniques and data interpretation. Experts in the fields of radiology, oncology, biostatistics, surgery, biomedical engineering, medical physics, other screening tools and signal processing must get involved in one team to develop a state of the art imaging system for breast cancer detection. Near-field microwave non-destructive non-ionizing non-invasive imaging systems utilizing open-ended rectangular waveguide sensors are coming of age and have proved to be a promising approach for breast cancer detection. In time they should hopefully become a successful clinical complement to other conventional screening techniques such as X-ray mammography, ultrasound and MRI.

# APPENDIX A

## *List of Publications*

A1. Wael Saleh and N. Qaddoumi, "Breast Cancer Detection Utilizing Loaded Open-Ended Rectangular Waveguide Sensors," *the 10th IEEE International Conference on Electronics, Circuits, and Systems, ICECS-2003*, University of Sharjah, Sharjah, UAE, 14-17 December 2003.

A2. Wael Saleh, David Wright, Philip Slade, and Nasser Qaddoumi, "Breast Cancer Detection Utilizing Near-Field Non-invasive Harmless Microwave Testing Technique," *5th UAE Diagnostic Imaging Conference*, April 18-21 2004, Armed Forces Officers Club, Abu Dhabi, UAE.

A3. Wael Saleh, David Wright, Philip Slade, and Nasser Qaddoumi, "Exploration of Breast Tumours Utilizing Non-invasive Near-Field Microwave Imaging," *Conference on Precision Electromagnetic Measurements 2004*, 27 June - 2 July, London, UK.

A4. Wael Saleh, "Breast Cancer Detection Utilizing a Non-Invasive Harmless Near-Field Microwave Testing Technique," Poster for *the Britain's Top Younger Engineers Competition*, 14th December 2004, House of Commons, London, UK.

A5. Wael Saleh, Philip Slade, Nasser Qaddoumi, and David Wright, "Microwave Breast Cancer Detection Using Open-Ended Rectangular Waveguide Probes," *10th International Symposium on Microwave and Optical Technology*, August 22-25, 2005, Fukuoka, Japan.

A6. Wael Saleh, Philip Slade, Nasser Qaddoumi, and David Wright, "Microwave Breast Cancer Detection Using Open-Ended Rectangular Waveguide Probes," *Special Issue of the International Journal of Microwave and Optical Technology*, 2006 (accepted for publication).

A7. Wael Saleh, Nasser Qaddoumi, and David Wright, "Breast Cancer Detection Utilizing Non-invasive Near-Field Microwave Imaging," accepted for *The 3rd International Conference on Electromagnetic Near-Field Characterization and Imaging* (ICONIC 2007), St. Louis, MO, USA, on June 27-29, 2007 (selected accepted papers will be published in *IEEE Transactions on Instrumentation and Measurement*).

# APPENDIX B

## *List of Awards and Certificates*

B1. **Young Scientist Bursary Award** in the Conference on Precision Electromagnetic Measurements (CPEM 2004), London, UK (only twenty scientists were chosen).

B2. **Youngest Researcher** at *5th UAE Diagnostic Imaging Conference*, April 18-21 2004, Armed Forces Officers Club, Abu Dhabi, UAE.

B3. **Participation in the Britain's Top Younger Engineers** held in House of Commons, December 2004. (About 95 of Britain's top younger research engineers from university and industrial research laboratories were selected from 140 entrants to make presentations as the House of Commons on their work. Dr. Aimee Morgans, of the Engineering Department at Cambridge University, won the top prize. Dr. Morgans is a Royal Academy of Engineering/EPSRC Postdoctoral Research Fellow).

B4. **Letter of invitation** from the conference chairman to attend the 10th International Symposium on Microwave and Optical Technology, August 22-25, 2005 Fukuoka, Japan (showing that I was the only participant from UAE).

NPL
National Physical Laboratory

National Physical Laboratory
Hampton Road
Teddington
Middlesex
United Kingdom
TW11 0LW

**Switchboard** 020 8977 3222
**NPL Helpline** 020 8943 6880
**Fax** 020 8943 6458

**www.npl.co.uk**

This is to certify that WAEL SALEH, PhD student of the University of Exeter, was awarded a Young Scientist Bursary to attend the Conference on Precision Electromagnetic Measurements (CPEM 2004) in London, on 27 June - 2 July 2004, after submitting papers: "Exploration of Breast Tumors Utilizing Noninvasive Near-field Microwave Imaging" and "Corrosion Detection And Thickness Evaluation Utilizing Active Near-Field Microwave Nondestructive Testing Techniques" for poster presentation in the RF Free Field Technical Session.

Stuart Pollitt

**Stuart Pollitt**
**Director – Enabling Metrology Division**
**National Physical Laboratory**

22 September 2006

**B2**

**5th United Arab Emirates**
**Diagnostic Imaging Conference**
**Abu Dhabi 18 – 21 April 2004**


This is to certify that Wael Saleh, Ph.D. candidate of the University of Exeter (UK), was the youngest researcher and presenter at the 5th UAE Diagnostic Imaging Conference, after submitting and presenting the paper entitled: "***Breast Cancer Detection Utilizing Near-Field Non-Invasive Harmless Microwave Testing Technique***" for an oral presentation in the free papers session. This certification is given on behalf of the scientific committee of the 5th UAE Diagnostic Imaging Conference.

Yours sincerely,

**Dr. Hatem A. Abou El Abbass, M.D.**
Senior Consultant Radiologist & Chairman of the Scientific Committee
E-mail: hatem_ghonim@yahoo.com / hes23oil@emirates.net.ae
Mobile Phone: 00971506285779 / 00971503577725
Fax No.: 0097165388957
P.O. Box 26924 Sharjah, UAE

| Conference members: | | | Contact Information | |
|---|---|---|---|---|
| President | : | H.E. Dr. A. Ghaffar A. Ghafoor | Tel. | : +971-26339931 |
| Conference Chairman | : | Hamed Kazim | Fax | : +971-26310084 |
| Secretary | : | Dr. Evelyn Bebars | E-mail | : federalradiology@hotmail.com |
| Scientific Chairman | : | Dr. Hatem Abou El Abbass | Website | : www.moh.gov.ae / moh_x_ray.htm |

Special Reception
Richard Page M.P.
Sponsoring Member

Presentations by and Competition for
Britain's Top Younger Engineers
House of Commons
Tuesday, 14 December 2004

Certificate of Participation

*Wael Saleh*

Richard Page M.P
Chairman: Parliamentary & Scientific Committee

Dr Eric Wharton
SET for BRITAIN

SET for BRITAIN

bp ExxonMobil BNFL Rolls-Royce Connected by vodafone RWE Thames Water

NATURAL ENVIRONMENT RESEARCH COUNCIL

The Royal Academy of Engineering

# 10th International Symposium on Microwave and Optical Technology

**August 22-25, 2005 Fukuoka, Japan**
**http://ismot2005.fit.ac.jp**

March 30, 2005

## Letter of Invitation to ISMOT2005

Wael Saleh
Microwave Imaging and Nondestructive Evaluation Laboratory
Electrical Engineering Department
School of Engineering
American University of Sharjah (AUS)
P.O. Box: 26666, Sharjah
United Arab Emirates (UAE)

Dear Wael Saleh:

I am delighted to inform you that the 10th International Symposium on Microwave and Optical Technology (**ISMOT2005**) is held in Fukuoka, Japan on August 22-25, 2005. This symposium is jointly organized by Kyushu University, Fukuoka Institute of Technology, Fukuoka, Japan, and University of Nevada, Reno, USA, and is held in cooperation with the International Union of Radio Science (URSI), the Electronic Society of the Institute of Electronics, Information and Communication Engineers (IEICE), the IEEE MTT/LEOS Japan Chapters and IEEE Fukuoka Section, IEEE Northern Nevada Section and MTT/LEOS Chapters, the Chinese Institute of Electronics (CIE), and the Institute of Electronics Engineers of Korea (IEEK). The ISMOT is intended to provide an international forum for exchanging new ideas, thoughts, and achievements on physics, applications, and technologies of microwaves, and optoelectronics, and related fields. Internationally leading experts on microwave and optical technology will join this exciting event.

It gives me great pleasure to invite you to present your paper entitled "**MICROWAVE BREAST CANCER DETECTION USING OPEN-ENDED RECTANGULAR WAVEGUIDE PROBES**" at ISMOT2005. You will be only one participant from your country. Your presentation as a representative of UAE will be much appreciated by the participants.

The latest information about the symposium is available on the ISMOT2005 website at: http://ismot2005.fit.ac.jp. If you have any questions or requests, please do not hesitate to contact us.

Looking forward to meeting you at ISMOT2005 in August.

With regards,

K. Yasumoto

Kiyotoshi Yasumoto
ISMOT2005 Chairman
Professor
Department of Computer Science and
Communication Engineering
Kyushu University
Fukuoka 812-8581, Japan

## REFERENCES


[Abu.03] Mohammed Abu-Khousa, Wael Saleh and Nasser Qaddoumi, "Defect Imaging and Characterization in Composite Structures Using Near-field Microwave Nondestructive Testing Techniques," *Journal of Composite Structures*, 62 (2003), pp. 255-259.

[Agi.85] "85027A/B/C Directional Bridge: Operating and Service Manual," Agilent Technologies, 1985.

[Agi.96a] "83751A/B and 83752A/B Synthesized Sweeper User's Guide," Agilent Technologies, 1996.

[Agi.96b] "83751A/B and 83752A/B Synthesized Sweeper Data Sheet," Agilent Technologies, 1996.

[Agi.96c] "Agilent 8757 Scalar Network Analyzer Data Sheet," Agilent Technologies, 1996.

[Agi.96d] "Agilent 423B, 8470B, 8472B, 8473B/C Low Barrier Schottky Diode Detectors Data Sheet," Agilent Technologies, 1996.

[Agi.00] "Agilent 85027 A/B/C Directional Bridge, Operating and Service Manual," Agilent Technologies, 2000.

[Alt.63] Altschuler, H.M., "Dielectric Constant," in M. Sucher and J. Fox, Eds. Handbook of Microwave Measurements, Vol. II, Brooklyn, NY, Polytechnic Press, Chapter 9, 1963.

[Arc.88] Arcone, S. A. and R. W. Larson, "Single-Horn Reflectometry For In Situ Dielectric Measurements at Microwave Frequencies," *IEEE Trans. on Geo. And Rmy. Sens.*, 26(1), pp. 89-92, Jan. 1988.

[Bah.82] Bahr, A.J., *Microwave Nondestructive Testing Methods,* Gordon and Breach Science Publishers, New York, NY, 1982

[Bah.02] Bahr, A., R. Zoughi and N. Qaddoumi, *Nondestructive Evaluation: Theory, Techniques, and Applications,* Chapter on Microwave Techniques, edited by P.J. Shull, Marcel and Dekker, Inc., 2002.

[Bak.92] Bakhtiari, S., S. Ganchev and R. Zoughi, "A Novel Technique for Microwave Thickness Measurement of Dielectric Slabs Using an Open-Ended Rectangular Waveguide," *Review of Progress in Quantitative NDE*, vol. 11A, pp. 529-535, Plenum Press, 1992.

[Bak.93] Bakhtiari, S., S. Ganchev and R. Zoughi, "Open-Ended Rectangular Waveguide for Nondestructive Thickness Measurement and Variation Detection of Lossy Dielectric Slabs Backed by a Conducting Plate," *IEEE Transactions on Instrumentation and Measurement*, vol. 42, no. 1, pp. 19-24, February, 1993.

[Bak.95] Bakhtiari, S., S. Ganchev and R. Zoughi, “A Generalized Formulation for Admittance of an Open-Ended Rectangular Waveguide Radiating into Stratified Dielectrics,” *Research in Nondestructive Evaluation*, vol. 7, no. 2/3, pp. 75-87, 1995.

[Bal.97] CA Balanis, *Antenna Theory, Analysis and Design*, New York: John Wiley and Sons, 1997.

[Bea.03] C. Beasley, S. C. Hagness, J. Booske, T. M. Breslin, F. Xu, M. J. Lindstrom, D. Popovic, M. Okoniewski, W. Temple, A. Magliocco, and T. Ogilvie, “Ex-Vivo Dielectric Characterization of Normal, Benign, and Malignant Breast Tissue At Microwave Frequencies: Preliminary Results from A Multi-Institutional Study,” *IEEE Int. Symp. Antennas Propag. USNC/URSI Radio Sci. Meeting*, Columbus, OH, June 2003.

[Bel.90] Belhadj-Tahar, N.-E., A. Fourrier-Lamar, and H. de Chanterac, “Broad Band Simultaneous Measurement Of Complex Permittivity And Permuability Using A Coaxial Discontinuity,” *IEEE Trans. on Microwave Theory Tech.*, vol. MTT- 38, pp. 1-7, Jan. 1990.

[Bra.65] R Bracewell, *The Fourier Transform and Its Applications*. New York: McGraw-Hill Book Co., Chapter 9,1965.

[Bre.82] R. J. Brenner, “X-ray mammography and diaphanography in screening for breast cancer,” *J Reprod Med*, vol. 27, no. 11, pp. 679-684, Nov. 1982.

[Bri.96] Brind J, Chinchilli M, et al, Induced abortion as an independent risk factor for breast cancer: *a comprehensive review and meta–analysis. J Epidemiol Community Health*, vol. 10, pp. 481–496, 1996.

[Bro.99] M. A. Brown and R. C. Semelka, *MRI: Basic Principles and Applications*, 2nd ed., Wiley-Liss, New York, 1999.

[Boi.99] Bois, K., A. Benally and R. Zoughi, "MultiMode Solution for the Reflection Properties of an Open-Ended Rectangular Waveguide Radiating into a Dielectric Half-Space: Forward and Inverse Problems," *IEEE Transactions on Instrumentation and Measurement*, vol. 48, no. 6, pp. 1131-1140, December 1999.

[Bol.90] Bolomey, J. Ch. and Pichot, Ch., "Microwave tomography: from theory to practical imaging systems," *Int. J. Imaging Syst. Technol.*, vol. 2, pp. 144-156, 1990.

[Bov.89] Boving, K. G. "NDE Handbook, Non-destructive examination methods for condition monitoring," Teknisk Forlag A/S (Danish Technical Press), 1989.

[Bus.99] S. C. Bushong, *Diagnostic Ultrasound*, McGraw-Hill, New York, 1999.

[Cam.92] A. M. Campbell and D. V. Land, "Dielectric Properties of Female Human Breast Tissue Measured In Vitro at 3.2 GHz," *Phys. Med. Biol.*, vol. 37, pp. 193-210, 1992.

[Car.00] K. L. Carr, P. Cevasco, P. Dunlea, and J. Shaeffer, “Radiometric Sensing: An Adjuvant to Mammography to Determine Breast Biopsy,” *IEEE MTT-S International Microwave Symposium Digest*, vol. 2, pp.929-932, June 2000.

[Cha.84] S. S. Chaudhary, R. K. Mishra, A. Swarup, and J. M. Thomas, “Dielectric Properties of Normal and Malignant Human Breast Tissues at Radiowave and Microwave Frequencies,” *Indian J. Biochem. Biophys.*, vol. 21, pp. 76-79, 1984.

[Che.98a] F. C. Chen and W. C. Chew, “Time-Domain Ultra-Wideband Microwave Imaging Radar System,” *Proc. IEEE Instr. Meas. Conf.*, pp. 648-650, 1998.

[Che.98b] W. C. Chew, “Imaging and Inverse Problems in Electromagnetics,” in *Advances in Computational Electrodynamics: The Finite-Difference-Time-Domain Method*, A. Taflove, Ed. Norwood, MA: Artech House, 1998, Ch. 12.

[Col.99] S. B. Colak, M. B. van der Mark, G. W.’t Hooft, J. H. Hoogenraad, E. S. van der Linden, and F. A. Kuijpers, “Clinical Optical Tomography and NIR Spectroscopy for Breast Cancer Detection,” *IEEE Journal of Selected Topics in Quantum Electronics*, vol. 5, no. 4, pp. 1143-1158, July/August 1999.

[Dec.74] Decreton, M. C., and F. E. Gardiol, “Simple Non-Destructive Method for Measurement of Complex Permittivity,” *IEEE Trans. on Instrumentation and Measurement*, vol. IM-23, pp. 434-438, Dec. 1974.

[Deh.03] Hamid Dehghani, Brian W Pogue, Steven P Poplack and Keith D Paulsen, “Multiwavelength Three Dimensional Near Infrared Tomography of the Breast: Initial Simulation, Phantom and Clinical results,” *Applied Optics*, vol. 42, no. 1, pp. 135-145, January 2003.

[Deh.04] Hamid Dehghani, Marvin M Doyley, Brian W Pogue, Shudong Jiang, Jason Geng and Keith D Paulsen, “Breast Deformation Modelling for Image Reconstruction in Near Infrared Optical Tomography,” *Phys. Med. Biol.*, vol. 49, no. 7, pp. 1131-1146, 2004.

[Deh.05] Hamid Dehghani, Ben Brooksby, Brian W Pogue and Keith D Paulsen, “Effect of Refractive Index on Near Infrared Tomography of the Breast,” *Applied Optics*, vol. 44, no. 10, pp. 1870-1878, April 2005.

[Edw.93] Edwards, J. and R. Zoughi, “Microwave Sensitivity Maximization of Disbond Characterization in Conductor Backed Dielectric Composites,” *Journal of Nondestructive Evaluation*, vol. 12, no. 3, pp. 193-198, September 1993.

[Enc.86] Encinar, J. A. and Rebollar, J. M., "Convergence of Numerical Solutions of Open-Ended Waveguide by Modal Analysis and Hybrid Modal-Spectral Techniques," *IEEE Trans. on Microwave Theory Tech.*, vol. MTT-34, no. 7, pp. 809-814, July 1986.

[Fea.00] E. C. Fear, and M. A. Stuchly, "Microwave Breast Cancer Detection." *IEEE MTT-S Digest*, pp. 1037-1040, 2000.

[Fea.02] E. Fear, S. C. Hagness, P. Meaney, M. Okoniewski, and M. Stuchly, "Enhancing Breast Tumor Detection with Near-Field Imaging," *IEEE Microwave Magazine*, vol. 3, no. 1, pp. 48-56, March 2002.

[Fin.05] M. L. Finkel, *Understanding the Mammography Controversy: Science, Politics, and Breast Cancer Screening*, 1st edition, Greenwood Publishing Group, Inc., 2005.

[Fos.89] K. R. Foster and H. P. Schwan, "Dielectric Properties of Tissues and Biological Materials: A Critical Review," *Crit. Rev. Biomed. Eng.*, vol. 17, pp. 25–104, 1989.

[Fra.98] A. Franchois, A. Joisel, C. Pichot, and J. C. Bolomey, "Quantitative Microwave Imaging with A 2.45 GHz Planar Microwave Camera," *IEEE Trans. Med. Imag.*, vol. 18, pp. 550-561, August 1998.

[Gab.96a] C. Gabriel, S. Gabriel, and E. Corthout, “The Dielectric Properties of Biological Tissues: I. Literature Survey,” *Phys. Med. Biol.*, vol. 41, pp. 2231-2249, 1996.

[Gab.96b] S. Gabriel, R. W. Lau, and C. Gabriel, “The Dielectric Properties of Biological Tissues: II. Measurements on the Frequency Range 10 Hz to 20 GHz,” *Phys. Med. Biol.*, vol. 41, pp. 2251-2269, 1996.

[Gab.96c] S. Gabriel, R. W. Lau, and C. Gabriel. “The Dielectric Properties of Biological Tissues: III. Parametric Models for the Dielectric Spectrum of Tissues,” *Phys. Med. Biol.*, vol. 41, pp. 2271-2293, 1996.

[Gan.01] O. P. Gandhi, Qing-Xiang Li and Gang Kang, “Temperature Rise for the Human Head for Cellular Telephones and for Peak SARs Prescribed in Safety Guidelines,” *IEEE Trans. on Microwave Theory and Techniques*, vol. 49, pp. 1607-1613, Sept. 2001.

[Gib.05] Gibson A P, J C Hebden, J Riley, N L Everdell, M Schweiger, S R Arridge, D T Delpy, “Linear and Non-linear Reconstruction for Optical Tomography of Phantoms with Non-scattering Regions,” *Applied Optics*, vol. 44, no. 19, pp. 3925-3936, July 2005.

[Gop.94] Gopalsami, S. Bakhtiari, S. Dieckman, P. Raptis and J. Lepper, “Millimeter-Wave Imaging for Nondestructive Evaluation of Materials,” *Materials Evaluation*, vol. 52, no. 3, March, 1994.

[Gra.97] Gray, S. and R. Zoughi, “Dielectric Sheet Thickness Variation and Disbond Detection in Multi-Layered Composites Using an Extremely Sensitive Microwave Approach,” *Materials Evaluation*, vol. 55, no. 1, pp. 42-48, 1997.

[Gro.80] C. Gros, M.D., M. Gautherie, “Breast Thermography and Cancer Risk Prediction,” *Cancer*, vol. 45, no. 1, pp. 51-56, 1980.

[Gur.06] Guray, M., Sahin, A. A., “Benign breast diseases: classification, diagnosis, and management,” *The Oncologist*, vol. 11, pp. 435-449, 2006.

[Hag.98] S. C. Hagness, A. Taflove, and J. E. Bridges, “Two-Dimensional FDTD Analysis of a Pulsed Microwave Confocal System for Breast Cancer Detection: Fixed-Focus and Antenna-Array Sensors,” *IEEE Trans. Biomedical Engineering,* vol. 45, pp. 1470-1479, Dec. 1998.

[Hag.99] S. C. Hagness, A. Taflove, and J. E. Bridges, “Three-Dimensional FDTD Analysis of a Pulsed Microwave Confocal System for Breast Cancer Detection: Design of an Antenna Array Element,” *IEEE Trans. Antennas Propagation,* vol. 41, pp. 783-791, May 1999.

[Has.97] R. H. Hashemi and W. G. Bradley, Jr., *MRI: The Basics*, Lippincott, Williams and Wilkins, Philadelphia, 1997.

[Heb.05] Hebden J. C., T. D. Yates, A. P. Gibson, N. Everdell, S. R. Arridge, D. W. Chicken, M. Douek, M. R. S. Keshtgar, "Monitoring Recovery Following Laser Surgery of the Breast Using Optical Tomography: A Case Study," *Applied Optics*, vol. 44, no. 10, pp. 1898-1904, April 2005.

[Her.83] B. Hermansson, D. Yevick and P. Danieisen, "Propagating Beam Analysis of Multimode Waveguide Tapers," *IEEE Journal of Quantum Electronics*, vol. QE-19, pp. 1246-1251, 1983.

[Hen.93] Henderson IC. Risk Factors for Breast Cancer Development. *Cancer Supplement*, vol. 71, 1993, pp. 2127–2140.

[Hew.85] "HP 8757A Scalar Network Analyzer Operating Manual," Hewlett-Packard Company, 1985.

[Hub.97a] Huber, C., H. Abiri, S. Ganchev and R. Zoughi, "Modeling of Surface Hairline Crack Detection in Metals Under Coatings Using Open-Ended Rectangular Waveguides," *IEEE Transactions on Microwave Theory and Techniques*, vol. 45, no. 11, pp. 2049-2057, November 1997.

[Hub.97b] Huber, C., S.I. Ganchev, R. Mirshahi, J. Easter and R. Zoughi, "Remote Detection of Surface Cracks/Slots Using Open-Ended Rectangular Waveguide Sensors: An Experimental Investigation," *Nondestructive Testing & Evaluation*, vol. 13, pp. 227-237, 1997.

[Hur.87] W. D. Hurt, J. M. Ziriax, and P. A. Mason, “Variability in EMF permittivity values: Implications for SAR calculations,” *IEEE Trans. Biomed. Eng.*, vol. BME-27, no. 10, pp. 396–401, Oct. 1987.

[Ina.99] U. S. Inan and A. S. Inan, *Engineering Electromagnetics*, Addison Wesley Longman, Inc., 1999.

[Jia.01] H. Jiang, , Y. Xu, N. Iftimia, J. Eggert, K. Klove, L. Baron and L. Fajardo, “Three-Dimensional Optical Tomogrpahic Imaging of Breast in a Human Subject,” , *IEEE Trans. in Medical Imaging*, vol. 20, no. 12, pp. 1334-1340, December 2001.

[Joi.94] W. T. Joines, Y. Z. Dhenxing, and R. L. Jirtle, “The Measured Electrical Properties of Normal and Malignant Human Tissues from 50 to 900 MHz,” *Med. Phys.*, vol. 21, pp. 547-550, 1994.

[Kir.94] Kirilenko, A. A., Senkevich, S. L., Tkachenko, V. I., Tysik, B. G., “Waveguide Diplexer and Multiplexer Design,” *IEEE Trans. MTT-S*, vol. 42, pp. 1393-1396, July 1994.

[Kor.82] Korotky, S. K., Minford, W. J., Buhl, L. L., Divino, M. D., Alferness, R. C., “Mode Size and Method for Estimating the Propagation Constant of Single-Mode Ti: LiNbO/sub 3/ Strip Waveguides,” *IEEE Trans. MTT-S*, vol. 82, pp. 1784-1789, October 1982.

[Kot.03] Kothari, M., "Benign breast disorders," *Chemist and Druggist*, pp. 19-22, March 2003.

[Kra.88] Kraus, J., *Antennas*, 2nd edition, McGraw-Hill, Inc. N.Y., 1988.

[Kra.92] Kraus, J. D., *Electromagnetics*, 4th edition, McGraw-Hill, Inc. N.Y., 1992.

[Kre.98] F. W. Kremkau and A. Allen, eds., *Diagnostic Ultrasound: Principles and Instruments*, Saunders, Philadelphia, 1998.

[Kru.99a] R. A. Kruger, K. K. Kopecky, A. M. Aisen, D. R. Reinecke, G. A. Kruger, and W. L. Kiser, Jr., "Thermoacoustic CT with Radio Waves: A Medical Imaging Paradigm," *Radiology*, vol. 211, pp. 275-278, 1999.

[Kru.99b] R. A. Kruger, W. L. Kiser, Jr., D. R. Reinecke, G. A. Kruger, and R. L. Eisenhart, "Thermoacoustic Computed Tomography of the Breast at 434 MHz," *IEEE MTT-S International Microwave Symposium Digest*, vol. 2, pp. 591-594, 1999.

[Lav.67] Lavelle, T.M., "Microwaves in Nondestructive Testing," *Materials Evaluation*, vol. 21, no. 11, pp. 254-257, Nov. 1967.

[Laz.07] M. Lazebnik, C. B. Watkins, J. H. Booske, S. C. Hagness, D. Popovic, L. McCartney, M. Okoniewski, M. J. Lindstrom, T. M. Breslin, J. Harter, S. Sewall, W. Temple, D.Mew4, A. Magliocco5, T. Ogilvie, "Large-Scale Studies of Ultrawideband Dielectric Properties of Normal and Malignant Breast Tissues at Microwave Frequencies," Accepted for *The 3rd International Conference on Electromagnetic Near-Field Characterization and Imaging* (ICONIC 2007), St. Louis, MO, USA, on June 27-29, 2007.

[Li.01] X. Li and S. C. Hagness, "A Confocal Microwave Imaging Algorithm for Breast Cancer Detection," *IEEE Microwave and Wireless Components Letters*, vol. 11, no. 3, pp. 130-132, March 2001.

[Li.03] X. Li, S. C. Hagness, B. D. Van Veen, and D. van der Weide, "Experimental Investigation of Microwave Imaging via Space-Time Beamforming for Breast Cancer Detection," *IEEE MTT-S International Microwave Symposium Digest*, vol. 1, pp. 379-382, Philadelphia, PA, June 2003.

[Li.04] X. Li, S. K. Davis, S. C. Hagness, D. van der Weide, and B. D. Van Veen, "Microwave imaging via space-time beamforming: Experimental investigation of tumor detection in multi-layer breast phantoms," *IEEE Transactions on Microwave Theory and Techniques*, vol. 52, no. 8, pp. 1856-1865, August 2004.

[Lov.95] Susan M. Love, MD and Karen Lindsey, *Dr. Susan Love's Breast Book*, 1995.

[Lun.72] Lundien, J. R., "Determining Presence Thickness And Electrical Properties of Stratified Media Using Swept Frequency Radar", Tech. Rept. M-72-4, U. S. Army Engineer Waterways Experimental Station, Nov. 1972.

[Mac.80] Macphie, R. H. and Zaghloul, A. I., "Radiation from a Rectangular Waveguide with Infinite Flange-Exact Solution by the Correlation Matrix Method," *IEEE Trans. Antennas Propagation*, vol. AP-28, no. 4, pp. 809-814, July 1980.

[Mar.70] D. Marcuse, "Radiation Losses of Tapered Dielectric Slab Waveguides," *Bell Systems Tech. J.*, vol. 49, pp. 273-290, 1970.

[Mea.99] P. M. Meaney, K. D. Paulsen, J. T. Chang, M. W. Fanning, and A. Hartov, "Nonactive Antenna Compensation for Fixed-Array Microwave Imaging: Part II- Imaging Results," *IEEE Trans. Med. Imag.*, vol. 18, pp. 508-518, June 1999.

[Mea.00] P. M. Meaney, M. W. Fanning, D. Li, S. P. Poplack, and K. D. Paulsen, "A Clinical Prototype for Active Microwave Imaging of the Breast," *IEEE Trans. Microw. Theory Tech.*, vol. 48, no. 11, pp. 1841–1853, Nov. 2000.

[Met.98] F. A. Mettler, M. J. Guberteau and B. Mettler, *Essentials of Nuclear Medicine Imaging*, Saunders, Philadelphia, 1998.

[Mir.71] Mirra AP, Cole P, et al. Breast cancer in an area of high parity: Sao Paulo, Brazil. *Cancer Research*. 1971; 31: 77–83.

[Miy.93] M. Miyakawa, "Tomographic Measurement of Temperature Change in Phantoms of the Human Body by Chirp Radar-Type Microwave Computed Tomography," *Med. Biol. Eng. Comput.*, vol. 31, pp. S31-S36, 1993.

[Moo.01] Moore, S.K., "Better breast cancer detection," *IEEE Spectrum*, vol. 38, issue 5, pp. 50-54, May 2001.

[Mou.00] S. Mouthy, B. Bocquet, R. Ringot, N. Rocourt, and P. Devos, "Microwave Radiometric Imaging for the Characterisation of Breast Tumours," *Eur. Phys. Journal: Appl. Phys.*, vol. 10, pp. 73-78. 2000.

[Mub.01] Mubarak, K., K.J. Bois and R. Zoughi, "A simple, Robust and On-Site Microwave Technique for Determining Water-to-Cement (w/c) Ratio of fresh Portland Cement-Based Materials" *IEEE Transactions on Instrumentation and Measurement*, vol. 50, no. 5, pp. 1255-1263, October 2001.

[Mur.94] J. N. Murrell, A. D. Jenkins, *Properties of Liquids and Solutions*, 2nd ed., John Wiley & Sons, Chichester, England, 1994.

[Nik.89] Nikita, K. S., and N. K. Uzunoglu, “Analysis of The Power Coupling From a Waveguide Hyperthermia Applicator Into a Three-Layered Tissue Model,” *IEEE Trans. on Microwave Theory and Tech.*, vol.MTT-37, no. 11, pp. 1794-1801, Nov. 1989.

[Nyi.86] I. Nyirjesy, “Clinical Evaluation, Mammography and Thermography in the Diagnosis of Breast Carcinoma,” *Thermology*, vol. 1, pp.170-173, 1986.

[Off.05] Office for National Statistics, Cancer Statistics registrations: Registrations of cancer diagnosed in 2002, England. Series MB1 no.33. 2005, National Statistics: London.

[Paq.00] D. Paquette, J. Snider, F. Bouchard, I. Olivotto, H. Bryant, K. Decker, and G. Doyle, “Performance of screening mammography in organized programs in Canada in 1996,” *Can. Med. Assoc. J.*, vol. 163, pp. 1133-1138, 2000.

[Par.96] Parker S, Tong T, et al. Cancer Statistics, 1996. *American Cancer Society*, vol. 46, pp.1–23, 1996.

[Par.59] W. H. Parsons, *Cancer of the Breast.* Springfield, IL: Thomas, 1959.

[Pau.99] K. D. Paulsen and P. M. Meaney, “Nonactive Antenna Compensation for Fixed-Array Microwave Imaging: Part I- Model Development,” *IEEE Trans. Med. Imag.*, vol. 18, pp. 496-507, June 1999.

[Poz.05] David Pozar, *Microwave Engineering*, 3rd edition, John Wiley and Sons, Inc., 2005.

[Qad.95a] Qaddoumi, N., S. Ganchev, G. W. Carriveau and R. Zoughi, "Microwave Imaging of Thick Composites with Defects," *Materials Evaluation*, vol. 53, no. 5, August 1995.

[Qad.95b] Qaddoumi, N., H. Abiri, S. Ganchev and R. Zoughi, "Near-Field Analysis of Rectangular Waveguide Probes Used for Imaging," *Proceedings of the Review of Progress in Quantitative NDE*, vol. 15A, pp. 727-732, Plenum Press, NY, 1995.

[Qad.96a] Qaddoumi, N., R. Zoughi and G.W. Carriveau, "Microwave Detection and Depth Determination of Disbonds in Low-Permittivity and Low-Loss Thick Sandwich Composites," *Research in Nondestructive Evaluation*, vol. 8, no. 1, 1996.

[Qad.96b] Qaddoumi, N. and R. Zoughi, "Microwave Detection of Corrosion Under Paint and Composite Laminate Coatings," *Proceedings of SPIE Symposium, Nondestructive Evaluation Techniques for Aging Infrastructure & Manufacturing Conferences*, Scottsdale, AZ, December 2-5, 1996.

[Qad.96c] Qaddoumi, N., Gamcjev. S. I. and R. Zoughi and G.W. Carriveau, "Microwave Diagnosis of Low-Density Fiberglass Composites with Resin Binder," *Research in Nondestructive Evaluation*, vol. 8, no. 3, 1996.

[Qad.97] Qaddoumi, N., A. Shroyer and R. Zoughi, "Microwave Detection of Rust Under Paint and Composite Laminates," *Research in Nondestructive Evaluation*, vol. 9, no. 4, pp. 201-212, 1997.

[Qad.98a] Qaddoumi, N., "Microwave Detection and Characterization of Subsurface Defect Properties in Composites Using Open Ended Rectangular Waveguide," Ph.D. Dissertation, Colorado State University, USA, 1998.

[Qad.98b] Qaddoumi, N., P. Stepanek, R. Mirshahi, E. Ranu, R. Zoughi, J.D. McColskey and R. Livingston, "Influence of Flange, Frequency and Liftoff on Microwave Detection of Stress Induced Fatigue Cracks Using Open-Ended Rectangular Waveguide," *Proceedings of the SPIE Symposium on Nondestructive Evaluation Techniques for Aging Infrastructure Manufacturing*, vol. 3396, pp. 208-215, San Antonio, TX, March 1998.

[Qad.00] Qaddoumi, N., L. Handjojo, T. Bigelow, J. Easter, A. Bray and R. Zoughi, "Microwave Corrosion Detection Using Open-Ended Rectangular Waveguide Sensors," *Materials Evaluation*, vol. 58, no. 2, pp. 178-184, February 2000.

[Rad.99] M. M. Radai, S. Abboud and M.Rosenfeld, "Evaluation of impedance technique for detecting breast carcinoma using a 2-D numerical model of the torso," *Annals of the New York Academy of Sciences*, vol. 873, pp. 360-369, 1999.

[Sad.95] M. N. O. Sadiku, *Elements of Electromagnetics*, 2nd edition, Oxford University Press, Inc., 1995.

[Sal.01] Wael Saleh and N. Qaddoumi "Corrosion Detection and Thickness Evaluation Using Microwave Nondestructive Testing Techniques," *2001 IEEE AP-S International Symposium and USNC/URSI National Radio Science Meeting*, Boston, Massachusetts, USA, July 8-13 2001.

[Sal.03a] Wael Saleh, Nasser Qaddoumi, and Mohammed Abu-Khousa, "Preliminary Investigation of Near-field Nondestructive Testing of Carbon-Loaded Composites Using Loaded Open-Ended Waveguides," *Journal of Composite Structures*, vol. 62, pp. 403-407, 2003.

[Sal.03b] Wael Saleh and N. Qaddoumi, "Breast Cancer Detection Utilizing Loaded Open-Ended Rectangular Waveguide Sensors," *the 10th IEEE International Conference on Electronics, Circuits, and Systems, ICECS-2003*, University of Sharjah, Sharjah, UAE, 14-17 December 2003.

[Sal.04a] Wael Saleh, David Wright, Philip Slade, and Nasser Qaddoumi, "Breast Cancer Detection Utilizing Near-Field Non-invasive Harmless Microwave Testing Technique," *5th UAE Diagnostic Imaging Conference*, April 18-21 2004, Armed Forces Officers Club, Abu Dhabi, UAE.

[Sal.04b] Wael Saleh, David Wright, Philip Slade, and Nasser Qaddoumi, "Exploration of Breast Tumours Utilizing Non-invasive Near-Field Microwave Imaging," *Conference on Precision Electromagnetic Measurements 2004*, pp. 202-203, 27 June - 2 July, London, UK.

[Sal.04c] Wael Saleh, "Breast Cancer Detection Utilizing a Non-Invasive Harmless Near-Field Microwave Testing Technique," Poster for *the Britain's Top Younger Engineers Competition***,** 14th December 2004, House of Commons, London, UK.

[Sal.05] Wael Saleh, Philip Slade, Nasser Qaddoumi, and David Wright, "Microwave Breast Cancer Detection Using Open-Ended Rectangular Waveguide Probes," *10th International Symposium on Microwave and Optical Technology*, August 22-25, 2005, Fukuoka, Japan.

[Sal.06] Wael Saleh, Philip Slade, Nasser Qaddoumi, and David Wright, "Microwave Breast Cancer Detection Using Open-Ended Rectangular Waveguide Probes," *Special Issue of the International Journal of Microwave and Optical Technology*, 2006 (accepted for publication).

[Sal.07] Wael Saleh, Nasser Qaddoumi, and David Wright, "Breast Cancer Detection Utilizing Non-invasive Near-Field Microwave Imaging," accepted for *The 3rd International Conference on Electromagnetic Near-Field Characterization and Imaging* (ICONIC 2007), St. Louis, MO, USA, on June 27-29, 2007 (selected accepted papers will be published in *IEEE Transactions on Instrumentation and Measurement*).

[She.97] Shen, Z. and Macphie, R. H., "A Simple Method for Calculating the Reflection Coefficient of Open-Ended Waveguides," *IEEE Trans. on Microwave Theory Tech.*, vol. MTT-45, no. 4, pp. 546-548, April 1997.

[Sou.98] A. E. Souvorov, A. E. Bulyshev, S. Y. Semenov, R. H. Svenson, A. G. Nazarov, Y. E. Sizov, and G. P. Tatsis, "Microwave Tomography: A Two-Dimensional Newton Iterative Scheme," *IEEE Trans. Microwave Theory Tech.*, vol. 46, pp. 1654-1658, November 1998.

[Sta.92] D. D. Stark and W. G. Bradley, Jr., *Magnetic Resonance Imaging*, 2nd ed., Mosby-Year Books, St. Louis, 1992.

[Ste.77] Steyskal, H., "Analysis of Circular Waveguide Arrays on Cylinders," *IEEE Trans. Antennas Propagation*, vol. 25, no. 5, pp. 610-616, Sep. 1977.

[Sub.06] Subhadra Srinivasan, Brian W. Pogue, Shudong Jiang, Hamid Dehghani, Christine Kogel, Sandra Soho, Jennifer J. Gibson, Tor D. Tosteson, Steven P. Poplack and Keith D. Paulsen, "In Vivo Hemoglobin and Water Concentration, Oxygen Saturation, and Scattering Estimates from Near-Infrared Breast Tomography Using Spectral Reconstruction," *Acad. Radiology*, vol. 13, no. 2, pp. 195-202, February 2006.

[Sur.88] Surowiec, S. S. Stuchly, J. R. Barr, and A. Swarup, "Dielectric Properties of Breast Carcinoma and the Surrounding Tissues," *IEEE Trans. Biomed. Eng.*, vol. 35, pp. 257-263, April 1988.

[Tav.99] Fattaneh A. Tavassoli, *Pathology of the Breast*, 2nd ed., McGraw-Hill, New York, 1999.

[Teo.85] Teodoridis, V., Sphicopoulos, T., Gardiol, F.E., "The Reflection from an Open-Ended Rectangular Waveguide Terminated by a Layered Dielectric Medium," *IEEE Trans. on Microwave Theory Tech.*, vol. MTT-33, no. 5, pp. 359-366, May 1985.

[Thr.01] J. H. Thrall and H. A. Ziessman, *Nuclear Medicine: The Requisites*, 2nd ed., Mosby St. Louis, 2001.

[Ven.86] Venugopalan, P., k. Jose, K. Nair, P Chaturvedi, and V. Ravindran, "Microwave Technique for Locating Inhomogenities in Cured Rocket Propellant Samples", *NDT International*, 19(6), pp. 395-397, Dec. 1986.

[Wan.98] L.-H. Wang, "Optical Tomography for Biomedical Applications," *IEEE Engineering in Medicine and Biology*, vol. 17, pp. 45-56, March/April 1998.

[Wan.99] L. V. Wang, X. Zho, H. Sun, and G. Ku, "Microwave-Induced Acoustic Imaging of Biological Tissues," *Rev. Sci. Instr.*, vol. 70, pp. 3744-3748, 1999.

[Wan.06] Xin Wang, Brian W. Pogue, Shudong Jiang, Hamid Dehghani, Xiaomei Song, Subhadra Srinivasan, Ben A. Brooksby, Keith D. Paulsen, Christine Kogel, Steven P. Poplack, and Wendy A. Wells, "Image reconstruction of effective Mie scattering parameters of breast tissue in vivo with near-infrared tomography," *Journal of Biomedical Optics*, vol. 11(4), 041106, July/August 2006.

[Wat.92] D.J. Watmough and K.M. Quan, “X-ray mammography and breast compression”, *Lancet*, 340, p.122, 1992.

[Web.03] Andrew Webb, *Introduction to Biomedical Imaging*, IEEE Press edition, John Wiley and Sons, Inc., 2003.

[Web.1] Website 1: http://www.imaginis.com/breasthealth

[Web.2] Website 2: http://info.cancerresearchuk.org/cancerstats/

[Web.3] Website 3: http://www.calgaryhealthregion.ca/

[Web.4] Website 4: www.hmhd.org/nuclear.htm

[Yat.05a] Tara D. Yates, “Time-resolved Optical Tomography for the Detection and Specification of Breast Disease,” Ph.D. thesis, University of College London, January 2005.

[Yat.05b] Yates T. D., J. C. Hebden, A. P. Gibson, N. Everdell, S. R. Arridge, and M. Douek, “Optical Tomography of the Breast Using A Multi-Channel Time-Resolved Imager”, *Phys. Med. Biol.*, vol. 50, pp. 2503-2517, May 2005.

[Yat.05c] Yates T. D., .J C. Hebden, A. P. Gibson, L. Enfield, N. L. Everdell, S. R. Arridge, and D. T. Delpy, “Time-resolved optical mammography using a liquid coupled interface,” *Journal of Biomedical Optics*, vol. 10, no. 5, September/October 2005.

[Yeh.94a] Yeh, C. and R. Zoughi, “Microwave Detection of Finite Surface Cracks in Metals Using Rectangular Waveguide Sensors,” *Research in Nondestructive Evaluation*, vol. 6, no. 1. pp. 35-55, 1994.

[Yeh.94b] Yeh, C. and R. Zoughi, “A Novel Microwave Method for Detection of Long Surface Cracks in Metals,” *IEEE Transactions on Instrumentation and Measurement*, vol. 43, no. 5, pp. 719-725, October, 1994.

[Yeh.94c] Yeh, C., E. Ranu and R. Zoughi, “A Novel Microwave Method for Surface Crack Detection Using Higher Order Waveguide Modes,” *Materials Evaluation*, vol. 52, no. 6, pp. 676-681, June, 1994

[Zou.90a] Zoughi, R. and S. Bakhtiari, “Microwave Nondestructive Detection and Evaluation of Disbonding and Delamination in Layered-dielectric Slabs,” *IEEE Trans. on Inst. and Meas.*, 39(6), pp. 1059-1063, Dec. 1990.

[Zou.90b] Zoughi, R. and S. Bakhtiari, “Microwave Nondestructive Detection and Evaluation of Voids in Layered-dielectric slabs”, *Research in Nondes. Eval.*, 2(4), pp. 195-205, 1990.

[Zou.90c] Zoughi, R. and M. Lujan, “Nondestructive Microwave Thickness Measurement of Dielectric Slabs”, *Materials Eval.*, 48(9), pp. 1100-1105, Sept. 1990.

[Zou.90d] Zoughi, R., “Microwave Nondestructive Testing: Theories and Applications,” *International Advances in Nondestructive Testing (IANDT)*, Vol. 15, pp. 255-288, Gordon and Breach Science Publishers, 1990.

[Zou.94] R. Zoughi and S. Ganchev, *Microwave Nondestructive Evaluation, State-of-the-Art Review*, Texas Research Institute (TRI/NTIAC) publications, 1994.